INFORMATION TO USERS

The negative microfilm of this dissertation was prepared and inspected by the school granting the degree. We are using this film without further inspection or change. If there are any questions about the content, please write directly to the school. The quality of this reproduction is heavily dependent upon the quality of the original material

The following explanation of techniques is provided to help clarify notations which may appear on this reproduction.

1. Manuscripts may not always be complete. When it is not possible to obtain missing pages, a note appears to indicate this.

2. When copyrighted materials are removed from the manuscript, a note appears to indicate this.

3. Oversize materials (maps, drawings, and charts) are photographed by sectioning the original, beginning at the upper left hand corner and continuing from left to right in equal sections with small overlaps.

UMI Dissertation
Information Service

A Bell & Howell Information Company
300 N. Zeeb Road, Ann Arbor, Michigan 48106

A dissertation entitled

STARTUP AND STABILITY

OF A SMALL SPHERICAL TOKAMAK

submitted to the Graduate School of the
University of Wisconsin-Madison
in partial fulfillment of the requirements for the
degree of Doctor of Philosophy

by

Gregory Douglas Garstka

Date of Final Oral Examination: September 15, 1997

Month & Year Degree to be awarded: **December** **May** **August**

1997

Approval Signatures of Dissertation Readers:

James D Callen

Raymond J Fonck

Stet C Prager

Signature, Dean of Graduate School

Virginia L Greenwald

STARTUP AND STABILITY

OF A

SMALL SPHERICAL TOKAMAK

by

Gregory Douglas Garstka

A dissertation submitted in partial fulfillment

of the requirements for the degree of

Doctor of Philosophy

(Nuclear Engineering and Engineering Physics)

at the

UNIVERSITY OF WISCONSIN - MADISON

1997

Acknowledgements

Here is my opportunity to step into the first person and acknowledge the help and camaraderie I have received from so many people in my six years at Wisconsin. My time here has been immeasurably enriched by the people I have known. I am grateful to you all.

I offer effusive thanks to my thesis advisor, Dr. Raymond Fonck. He has been a constant source of guidance, font of knowledge, and helping hand throughout my tenure here. He was the driving force behind MEDUSA; he pushed when we were foundering, rewarded us for our achievements, and celebrated our victories. I've gained a great deal, both professionally and personally, under his tutelage. I will miss working for him.

I am in the debt of a great many others here at the U.W. Tom Intrator was a great help, particularly with the triple probe and the new OH coils. Greg Winz rose above the call of duty for me quite often, and did excellent work. Paul Nonn's expertise (in just about *everything*, it sometimes seemed) was an enormous asset. Thanks are due to Jim DeKock for helping me stay connected, Tom Lovell for repeated lectures on, and pieces of, hardware, John Laufenberg for the SCR basics, Daniel Den Hartog for helping me through my first year, Bob Ashley for electronics and lots of other stuff, Chris Hegna for valuable discussions into tokamak physics, Sol Walsh for his great skill at machining, and Rose Birzer and Mark Swandby for helping me navigate the bureaucratic minefields. I would also like to thank Pat Caliva and Pam Wagner for their frequent, valuable assistance. I cannot say enough to recognize and applaud the efforts of the entire MEDUSA team as well. Many of them never saw the tokamak operate, but their *belief* in the project and team helped carry us forward, even through the hard times.

On the personal side, I have made many friends here whom I want to acknowledge. Tim and Gail Thorson have been my friends since I began graduate school; they have been kind, generous, understanding, and fun ("Did you see that jerk? Dropped his notes!") throughout our shared ordeal. Tim and Gail also had the patience and magnanimity to put me

up for my last weeks in school. Ben Lewicki has been a good friend, confidante, and fellow consumer of good beer and coffee. Ben gets extra thanks for introducing me to Lisa. Kevin Tritz is a great guy. George McKee, Tom Gianakon, and I shared many evenings of philosophy and culture over plates of buffalo wings and glasses of doppelbock. Ji-Soo Kim and Jim Gilland were always ready to discuss physics, society, or life in general. Scott Kruger and Yas Nishimura were all-around cool dudes. Pete Kies, Dwayne Kaufman, Mirko Vukovic, and Palmer Smitherman added levity and friendship to my first years here, while Aaron Sontag and Betsy Reinecke have been new but welcome additions to our circle of friends. I have been blessed with a series of great roommates: Steve Wukitch, Rob Coffey, Derek Mayer, and Ben, Kevin, and Scott Willems. I would also like to thank "the exes"—Jenny Gottwald, Kelly Kasum, Ted Ressel, Jenny Schroeder, Kate Wachholz, and Amy Wendelborn— for the good times we've enjoyed. I would be remiss without mentioning Chloe, Bailey, Macro, Micro, Mr. Fish, Muffy, Perry, Casey, and Samuel Foster Adams. Finally, a hearty "nice catch" to all those who were on the receiving end of my rocket and grenade launchers. "Whose side are you on?!"

But my greatest thanks go to my family. My grandparents, Douglas and Catherine Miller and Joseph and Elsie Garstka, helped make me the person I am today. My brother Brian has become a true friend. He knows me better than anyone else; I am extremely proud of him and all that he has accomplished. Words cannot express the depth of my feeling for my parents Joseph and Virginia. They have supported me through good times and bad; they have always been encouraging and loving. To them I owe much that I can never repay. Finally, I want to thank my fianceé Lisa Wendelborn. She has been consistently understanding and supportive throughout the composition of this thesis, and her family has gone to great lengths to make me feel welcome. Lisa has filled the last eighteen months of my life with joy, laughter, and love. I look forward to the life we will lead together.

Gregory Douglas Garstka

September 8, 1997

To my family —

past, present, and future

Table of Contents

Abstract

The spherical tokamak (ST) is an evolutionary extension of the conventional tokamak concept where the aspect ratio is less than 2. These devices may possess significant advantages over standard tokamaks—they are capable of achieving higher values of β, seem to be more resilient to disruptions, and are significantly smaller than conventional tokamaks. Two important questions for the next generation of spherical tokamaks concern startup and internal reconnection events (IREs). Understanding startup is crucial due to the limited amount of ohmic flux in an ST. The IREs are disruption-like events observed on STs that do not result in termination of the current channel.

Experiments have been conducted on the Madison EDUcational Small Aspect-ratio (MEDUSA) tokamak to answer some of the questions about startup and IREs in STs. MEDUSA is a small ohmic tokamak with an insulating vacuum vessel. Major parameters are R=12 cm, a=8 cm, I_p=10-40 kA, B_T=0.2-0.45 T, Δt_{pulse}=1-2 ms, $\langle n_e \rangle \approx 5\times10^{19}$ m^{-3}, and $T_{e0} \approx$100 eV. The experiments in this work were aided by an internal magnetic probe array that constrained the reconstruction of MHD equilibria.

It was found that startup efficiency, measured by the Ejima coefficient C_E, improved with increasing loop voltage and toroidal field. Double tearing modes were found to be an important mechanism for current penetration in MEDUSA; their presence early in the discharge can improve the magnetic flux consumption. The lowest achieved value of the Ejima coefficient was 0.61 (0.13 for "OH only") for a discharge with 0.375 T toroidal field and 9.4 V startup loop voltage.

The study of internal reconnection events revealed the presence of a heretofore undiscovered precursor, which in MEDUSA was manifested as coherent oscillations in the

internal poloidal field at 65-75 kHz for 100 μs prior to the IRE. These events were found to result in decreased ℓ_i and β, inward movement of the magnetic axis, dramatically increased q_0, and slightly decreased q_{98}. The magnetic helicity was found to change between -15% and +28% over an IRE.

1. Introduction

1.1 Energy and Society

The civilization of the industrialized world depends on the ready availability of large amounts of energy. There is scarcely an area of modern life that energy does not affect. This energy consumption is obviously apparent in some of its forms, such as personal transportation and space heating. However, many of the effects of energy consumption are secondary in nature. Food production is greatly increased by mechanized harvesting. Communication relies on electrically-powered systems. Many medical diagnostics and treatments require electrical power in order to function. Energy is so much a part of life that it is essentially taken for granted.

The United States alone used 90.62 Q (2.66×10^{13} kW-hr) in 1995, split roughly equally between residential / commercial, industrial, and transportation uses [1]. (A Quad, abbreviated Q, is a quadrillion BTUs of energy, which is approximately 2.9×10^{11} kW-hr.) This is roughly equal to 10^5 kW-hr per person. The U.S. energy consumption has increased dramatically over the past two centuries, and it can be argued that the increasing use of energy correlates strongly with the rise of the American standard of living. In 1850, for example, total U.S. energy consumption was 2.4 Q (or 3.1×10^4 kW-hr per person), while in 1920 the total was 21.4 Q (or 5.9×10^4 kW-hr per person) [2,3]. Even these figures are understated, though, because improvements in technology have increased the efficiency of energy use. For example, gas and electric heating are much more efficient than a fireplace.

The developing nations of the world will require similar quantities of energy if they are to improve their material well-being. This is indeed what forecasters believe will happen.

The world consumption of energy in 1995 was approximately 360 Q. By 2015, the U.S. Department of Energy predicts an increase in world consumption of over 50%, to 562 Q. This growth will be especially concentrated in Asia, where a number of developing nations (India and China are examples) are expanding their energy base [4].

But herein lies a problem—the world's most commonly-used energy resources, fossil fuels, are in limited supply. Fossil fuels comprise 84% of the energy consumption in the U.S. [1], the balance being composed of nuclear power and renewables, primarily hydroelectricity. Crude oil is the fossil fuel with the smallest estimated world supply. In 1995, world consumption of crude oil was roughly 25 billion barrels (bbl) per year. In the year 2015, this consumption is expected to grow to 38 billion bbl/year [4]. The U.S. Geological Survey estimates that the total amount of recoverable crude oil in the world is between 2.1 trillion and 2.8 trillion bbl [5]. These statistics imply that the supply of crude oil will run out in 70 to 90 years from now.

The picture is somewhat brighter for coal, at least in the U.S. Here the total estimated reserve is 4 trillion short tons (3.6 trillion tonnes) [6], which is enough to last for several thousand years at current levels of consumption. These levels will likely increase dramatically in the next century, however, when supplies of crude oil run out. Most of the nations of the earth do not have reserves as plentiful as the U.S., and it is outside the U.S. where energy demand is most likely to grow.

Another difficulty with fossil fuels is environmental effects. Fossil fuels must be mined, transported, burned, and disposed. The current consumption of coal in the U.S.[6], for example, results in approximately 1 billion short tons of waste (solid, as ash, and gaseous, as CO_x, SO_x, etc.) that must be disposed of each year. The burning of crude oil products (e.g. diesel fuel and gasoline) as motor vehicle fuel is a major source of air pollution in urban areas. The ocean transport of oil can result in oil spills, with all of the

associated environmental damage.

Because of these and other limitations of fossil fuels, it is desirable to find new energy sources for the future. This search has concentrated primarily on sources of electricity, since electricity is one of the most versatile forms of energy. It has delivered a few marketable technologies, most notably nuclear fission power. Nuclear power provides about 10% of U.S. electrical energy, and significantly greater percentages in some other countries such as France and Japan. Other technologies, such as geothermal and wind power, have been employed in locations where they are feasible. Still others, such as photovoltaic panels, are not currently employable but might be after further development.

1.2 Nuclear Fusion and Tokamaks

Perhaps the most promising of these new technologies, and the basic impetus for this thesis, is nuclear fusion power. Fusion is the process that powers the stars, and hence is the starting point for most of the energy on the earth. It is conceivable that a power reactor which used this process could be constructed. Such a reactor would have many advantages, as will be discussed.

It has been known for decades that the binary nuclear reactions of several different light atoms are exothermic. Among the most common of these reactions are [7]:

$$\begin{aligned} D + D &\rightarrow T + H + 4.04\,MeV \\ D + D &\rightarrow {}^{3}He + n + 3.27\,MeV \\ D + T &\rightarrow He + n + 17.58\,MeV \\ D + {}^{3}He &\rightarrow He + H + 17.34\,MeV \end{aligned} \qquad (1\text{-}1)$$

where D is deuterium (^2H) and T is tritium (^3H). (The reaction energies are divided among the products according to conservation of momentum.) Deuterium is available naturally as a

small fraction (0.015 atom percent) of hydrogen, and can be extracted from any water source. Tritium can be bred by n-Li reactions. These substances are widely spread throughout the world in large quantities.

The advantages of using fusion to provide electricity are manifold. The fuel for fusion reactors is widespread and abundant. It would require little or no mining, and its acquisition and transport would cause essentially no safety or environmental problems. There is little waste produced by fusion reactions; the "spent fuel" is mostly hydrogen and helium. The most hazardous waste would be irradiated reactor components, which would have short half-lives and pose no threat to public safety. If the D-^{3}He fuel cycle is eventually employed, it will significantly reduce the irradiation of reactor components. In currently-envisioned concepts, fusion reactors would be inherently fail-safe; no runaway reaction would be possible.

But the reactions in equation 1-1 are not easy to precipitate. The electrostatic repulsion of atomic nuclei keeps them relatively far apart, unless they have enough kinetic energy to overcome this potential barrier and fuse. This means that fusion reactions require high temperatures in order to occur in substantial numbers. The D-T reaction, for example, has a negligible cross-section below 7 keV of center-of-mass energy; the cross-section for this reaction peaks at 5 barns (1 barn = 10^{-24} cm^2) at an energy near 100 keV.The cross-sections for the D-D and D-^{3}He reaction peak at even higher energies. These high temperatures require the fusion fuels to exist in the plasma state. Many difficult steps must be taken to produce and confine a fusion-grade plasma.

So far two different families of concepts have evolved to do this. The first, inertial confinement fusion (ICF), also known as inertial fusion energy (IFE), makes fusion occur in a series of what are essentially tiny hydrogen bombs. These bombs, more properly known as targets, are imploded by some outside driver such as lasers or ion beams. ICF is

outside the scope of this thesis and will not be addressed further. The other major concept is magnetic confinement fusion. This concept relies on the fact that charged particles can be confined in a magnetic field according to the Lorentz force equation. There are many different types of devices that take advantage of this principle. Among them are tandem mirrors, stellarators, reversed-field pinches, and tokamaks.

The tokamak has emerged as the leading candidate of these devices (although the race is far from over). A tokamak consists of a toroidal vacuum chamber which houses the plasma, several sets of external magnets to confine the plasma in this geometry, and large amounts of auxiliary hardware to create, fuel, heat, and diagnose the plasma. The largest magnetic field component in a tokamak is directed in the toroidal direction. The plasma itself carries a toroidal current which generates a magnetic field in the poloidal direction. This current is usually driven by transformer action via an "ohmic solenoid" in the central bore of the torus. Chapter 2 contains a thorough discussion of tokamaks and tokamak physics.

Tokamaks have proven to be quite good at confining fusion-grade plasmas, but they still need significant improvements before the tokamak concept leads to a fusion reactor. One attempt to improve the tokamak is known as the spherical tokamak (ST), also known as the low-aspect-ratio tokamak. The ST is identical to conventional tokamaks except for one feature: the radius of the center hole of the torus is relatively small compared to the major radius of the plasma. The aspect ratio (A) is often used to characterize spherical tokamaks. The aspect ratio is the ratio of the plasma major radius (distance from the center of the torus to the center of the plasma cross-section) to the minor radius (distance from the plasma center to the plasma edge). For conventional tokamaks, A is typically around 3 to 5. Spherical tokamaks are defined as tokamaks having $A<2$, although the aspect ratio in STs is generally significantly lower than that (1.2-1.5). The primary advantage of the spherical tokamak is that it can confine plasmas of significantly higher beta (β) than conventional

tokamaks. Beta is the ratio of plasma pressure (nkT) to magnetic field pressure ($B^2/2\mu_0$), and is a figure of merit for a magnetic fusion confinement scheme. It can be demonstrated that the fusion power density is proportional to β^2 [8], so any confinement scheme that results in increased beta, such as the spherical tokamak, should be examined closely.

1.3 Motivation

This thesis is the result of studies of the performance of one particular spherical tokamak, the Madison EDUcational Small Aspect-ratio tokamak (MEDUSA). MEDUSA is described in detail in Chapter 4. The purpose of the research was twofold. The first purpose was to understand the consumption of ohmic flux by the plasma during startup and to identify the mechanisms responsible for current penetration during the startup phase of the tokamak discharge. The second was to gain an understanding of the process(es) responsible for internal reconnection events (IREs) in spherical tokamaks.

Startup is an important phase in any tokamak discharge. This is especially true for spherical tokamaks due to the geometry-imposed shortage of magnetic flux (volt-seconds) from the ohmic solenoid. This shortage makes crucial the understanding of the plasma's consumption of this flux if the tokamak is to reach its best performance in terms of ohmic current drive and heating. To this end, a study was undertaken on MEDUSA to understand the flux consumption, particularly the partition of input ohmic flux into dissipative and inductive components in the plasma. This flux consumption is closely related to the plasma current profile evolution, and hence the mechanisms responsible for current penetration are important here. This issue is particularly important with the imminent operation of the Pegasus toroidal experiment [9], which is to operate initially as an extremely low aspect-ratio tokamak (ELART) with a severely restricted amount of volt-seconds available for

startup.

Internal reconnection events seem to be quasi-disruptions that occur in STs. These events do not necessarily lead to premature termination of the discharge, as disruptions normally do. For a few years, evidence from the Small Tight Aspect Ratio Tokamak (START) (see numerous references in Chapter 2) suggested that spherical tokamaks might be immune to the hard disruptions which plague conventional tokamak operations. Although START has now been observed to disrupt, it does so infrequently; IREs are observed much more often. IREs are observed on other operating ST experiments; MEDUSA was the first experiment to confirm this phenomenon. Concurrent with the study of flux consumption, an effort was made to study IREs on MEDUSA. In particular, the evolution of the plasma equilibrium state across IREs was desired, as well as the evolution of the internal magnetic fields. Any precursors to these events were sought.

The studies of both startup and internal reconnection events rely on good equilibrium reconstructions of the plasma throughout the discharge. The magnetic diagnostics on MEDUSA were used as input to TokaMac 2.0, a fitting code that uses the well-known Grad-Shafranov equilibrium equation. Especially important was the use of an internal magnetic probe array, which returned the value of the major-radial magnetic field (**B•R**) at five points in the plasma throughout the discharge. This probe allowed routine determination of the plasma current profile, which was found to change dramatically during startup, and violently during an IRE.

1.4 Objectives and Organization

The objectives of this thesis research were:

1. Design, construct and operate a small spherical tokamak with interesting physical parameters.

2. Characterize the plasma equilibrium state (via a Grad-Shafranov code) throughout the discharge by direct measurements of plasma parameters, including current, flux, magnetic field, and temperature and density measurements.

3. Use these equilibria to analyze the magnetic flux consumption of different startup scenarios to objectively determine which startup technique results in the best use of limited ohmic volt-seconds, and identify the mechanisms responsible for the differences between shots.

4. Characterize plasma behavior before and during internal reconnection events, and attempt to find evidence of any precursors to these events.

This thesis is organized as follows. Chapter 2 contains a discussion of the physics of tokamaks, with an emphasis on spherical tokamaks. There is also a description of operating ST experiments and a discussion of the reactor-relevance of spherical tokamaks. Chapter 3 deals with plasma current distribution phenomena in tokamaks, treating specifically current diffusion, single and double tearing modes, disruptions, sawteeth, and IREs. MEDUSA is the subject of Chapter 4, where the various subsystems and experimental operation of the

tokamak are described. Chapter 5 discusses the equilibrium and flux consumption results from MEDUSA. Chapter 6 is concerned with the mechanics of current penetration during startup, and the results from studies of internal reconnection events. Chapter 7 then summarizes the thesis.

1.5 References

1. *Annual Energy Review 1995*, U.S. Department of Energy, Energy Information Administration, November 1996.

2. MELOSI, M.V., *Coping with Abundance: Energy and Environment in Industrial America*, Alfred A. Knopf, New York, p. 6, 1985.

3. U.S. Census Bureau Population Data for 1850, 1920, 1990.

4 *International Energy Outlook 1997*, U.S. Department of Energy, Energy Information Administration, May 1997.

5 MASTERS, C., et al., *A World Petroleum Assessment and Analysis*, in Proc. 14th World Petroleum Congress, John Wiley and Sons, New York, 1994, quoted in reference 4.

6. *Coal Data: A Reference*, U.S. Department of Energy, Energy Information Administration, February 1995.

7. MIYAMOTO, K., *Plasma Physics for Nuclear Fusion*, MIT Press, Cambridge, MA, p. 4, 1987.

8. STACEY, W.M., *Fusion: An Introduction to the Physics and Technology of Magnetic Confinement Fusion*, John Wiley and Sons, New York, 1984.

9. FONCK, R.J., et al., Bull. Am. Phys. Soc. **41** (1996) 1400.

2. Spherical Tokamaks

2.1 Introduction

Spherical tokamaks, also known as low-aspect-ratio or small-aspect-ratio tokamaks, have become a very active area of fusion research in the past few years. The spherical tokamak (ST) has exhibited a number of advantages over the "conventional" tokamak that: allow ready access to interesting high-β plasmas; could help lead to near-term commercialization of fusion technology; and may make it a more promising fusion reactor concept. Among these advantages are very high values of achievable beta, resilience to hard disruptions, and small reactor volume. These advantages must be contrasted with the difficulties of building and operating an ST, which stem primarily from the small area of the central bore.

The ST [1-3] is an evolutionary modification of the standard tokamak. In fact, it is conceptually identical to a conventional tokamak, with the aspect ratio (and the associated limits on coils, vacuum vessel, etc. naturally included) being the only difference between the two. The strong effects of toroidicity in a ST, however, lead to many significant differences from "conventional" tokamaks.

This chapter discusses the physics of spherical tokamaks. Section 2.2 provides a physics overview of standard and spherical tokamaks, including equilibrium, stability, and confinement. Section 2.3 contains a summary of past and current ST research, including presently operating and under-construction experiments. Section 2.4 is a discussion of engineering issues relevant to STs.

2.2 Physics of Conventional and Spherical Tokamaks

This section contains an overview of the physics of conventional and spherical tokamaks. It is intended primarily to be an introduction to the subject of spherical tokamaks, and to provide a physics background for this thesis. More information on the topics discussed in this section can be found in the references.

Tokamak Configuration

The tokamak is certainly the most thoroughly studied magnetic-confinement-fusion configuration. In its simplest form, a tokamak consists of a toroidal plasma resident in a confining and stabilizing magnetic field. The toroidal geometry used to describe tokamaks is illustrated in Figure 2-1. A simplified schematic of a tokamak is shown in Figure 2-2. The magnetic field is generated by three sources. The primary magnetic field component in a conventional tokamak is known as the "toroidal field;" this field is generated by coils that encircle the plasma at regular intervals. As the name indicates, this field is directed in the toroidal (ϕ) direction, and has a magnitude that is proportional to $1/R$, where R is the major radius of the tokamak. The second field is known as the "poloidal field" and is generated primarily by toroidal current flowing in the plasma. This field has no toroidal component; for a perfectly circular plasma this field is directed purely in the poloidal (θ) direction, i.e. it is in the R,Z plane at fixed ϕ. For a noncircular plasma this field has components in both the R and Z directions. The magnitudes of these components are a result of the complex details of the plasma equilibrium. A part of the poloidal field is known the "equilibrium field" or the "vertical field." This field is also poloidal in nature, but is provided by coils external to the plasma. These coils are toroidally axisymmetric and carry toroidal current. This field is required to maintain the equilibrium state of the plasma. It does so by providing the main

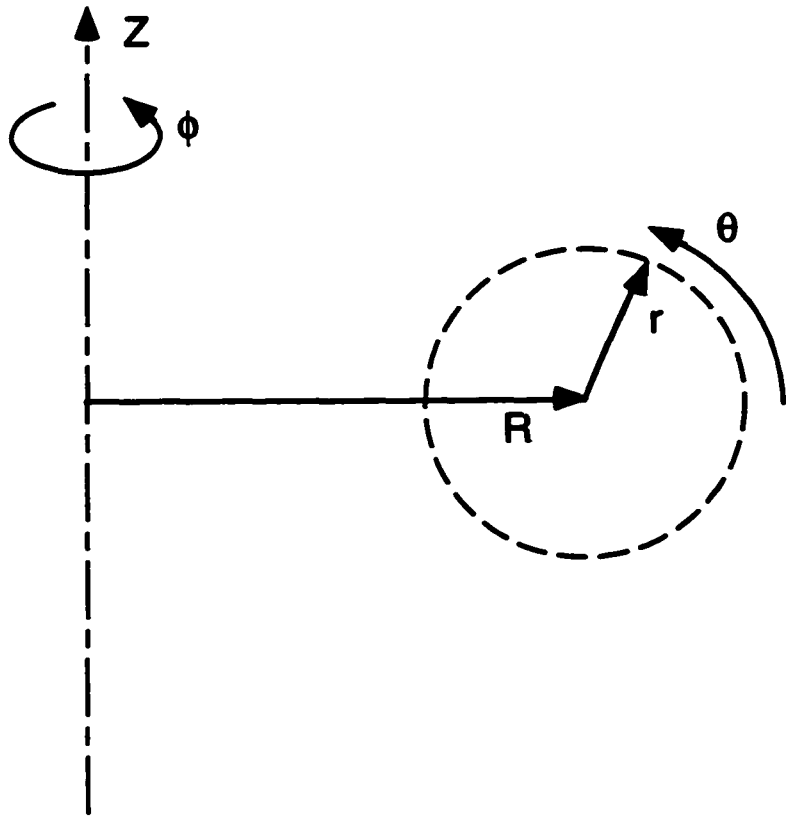

Figure 2-1. Toroidal geometry.

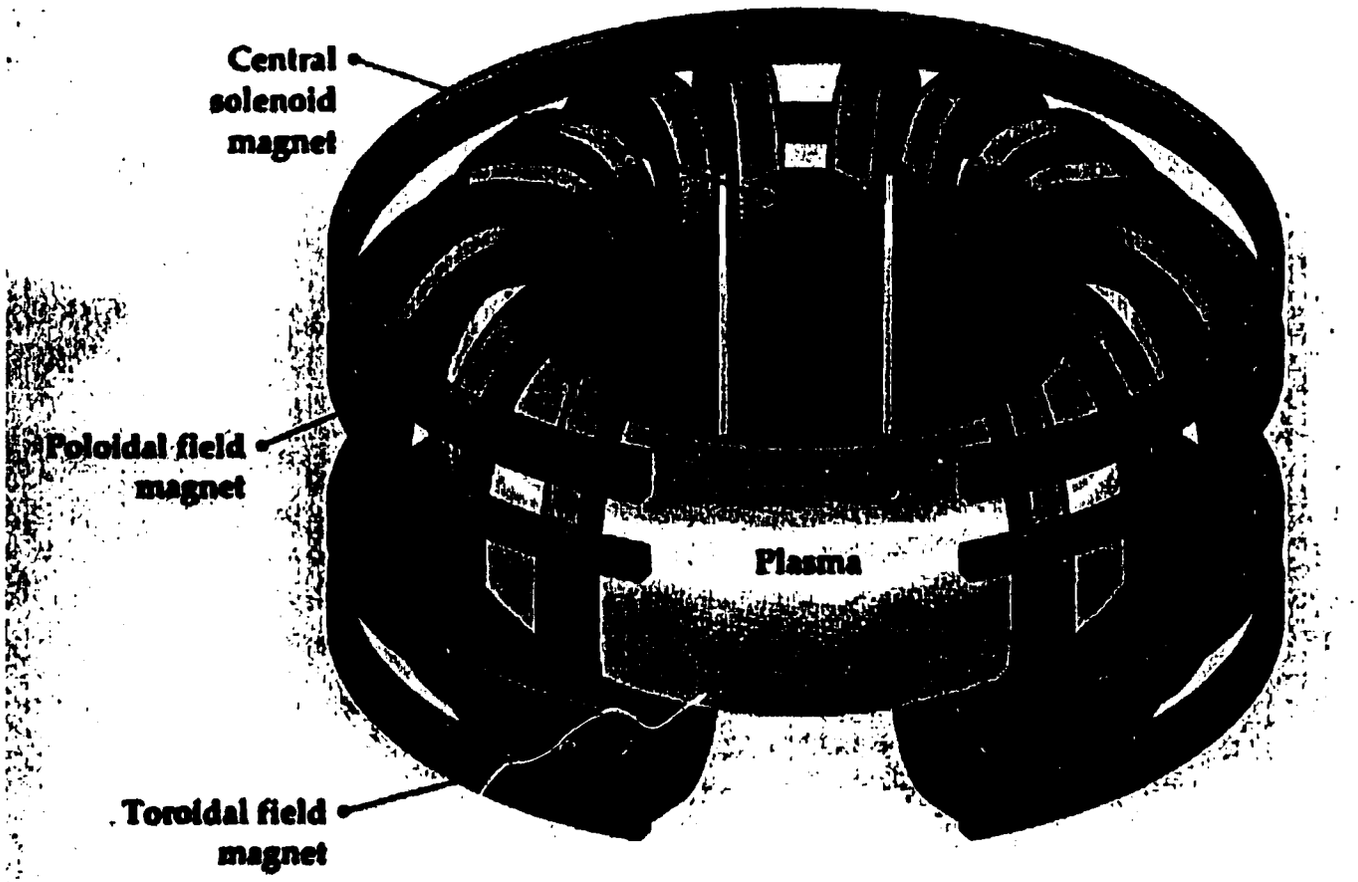

Figure 2-2. Simplified schematic of a tokamak (source: PPPL).

restoring force against radial expansion of the plasma current loop. It is also used to provide shaping for non-circular plasmas.

The plasma current is usually driven by magnetic induction; this is provided by another set of magnetic coils. This set, often called the "Ohmic Heating" or "OH" coil set, usually consists of a solenoid through the bore of the torus and a few other "trim" coils to keep this magnetic field away from the plasma. In order to drive a steady-state current in the plasma, a constant inductive voltage (loop voltage) must be applied. This requires that the current in the OH coils must be continually increased in accordance with Faraday's Law:

$$V_{loop} = \oint_C \mathbf{E}\cdot d\mathbf{l} = -\int_S \frac{\partial \mathbf{B}}{\partial t}\cdot d\mathbf{A} \qquad (2\text{-}1)$$

where C is a contour around the solenoid and S is the area encompassed by that contour. There are obviously physical limits on the amount of current that can be driven in the OH system; these limits generally force tokamaks to be pulsed devices. Much research is underway to drive plasma current by alternate means. Examples include coaxial helicity injection [4,5] and RF current drive by techniques such as lower hybrid waves [6-8], Alfven waves [9], and high-harmonic fast waves [10].

A spherical tokamak is merely a tokamak operating at an extreme of one of its parameters, the aspect ratio. One would expect, therefore, to be able to describe a ST in the same ways as one would a conventional tokamak. In many cases this is true—spherical tokamaks obey the Grad-Shafranov magnetic equilibrium equation, experience MHD instabilities, have trapped particles, and operate much the same way as other tokamaks.

In many of the particulars, though, STs behave quite differently than conventional tokamak wisdom would predict. Most of these differences are attributable to the large toroidal field gradient across an ST plasma [11]. The vacuum toroidal field of a tokamak is proportional to $1/R$; the ratio of the inboard magnetic field to the outboard field is then a

function of aspect ratio and can be written as

$$g(A) = \frac{B_\phi(R+a)}{B_\phi(R-a)} = \frac{A+1}{A-1} \qquad (2\text{-}2)$$

where g is the ratio of the fields and A is the aspect-ratio. Thus a tokamak with an aspect ratio of 5 will have g =1.5, A=2 gives g=3, A=1.5 gives g=5, and A=1.1 gives g=21. This large gradient of the toroidal field gives rise to a host of effects not generally noticeable in standard tokamaks: high edge magnetic shear, a large trapped particle fraction, values of q_a significantly different from q_*, and many others. The low aspect ratio geometry also has implications from the engineering standpoint too; most of these stem from the small size of the central bore of an ST. These issues will be discussed at the end of this section.

Tokamak Equilibrium

The equations of ideal magnetohydrodynamics (MHD) can be used to describe the equilibrium state of a plasma [12,13]. The ideal MHD description treats the plasma as a conducting fluid. For plasma equilibrium, three equations are of particular importance. The first is the condition on the divergence of the magnetic field:

$$\nabla \cdot \mathbf{B} = 0 \qquad (2\text{-}3)$$

where **B** is the magnetic induction, commonly known in plasma physics simply as the magnetic field. The second equation of importance is Ampere's Law:

$$\nabla \times \mathbf{B} = \mu_0 \mathbf{J} + \frac{1}{c^2}\frac{\partial \mathbf{E}}{\partial t} \qquad (2\text{-}4)$$

where **J** is the current density in the plasma. The third equation is the relation governing conservation of plasma momentum:

$$\rho\left[\frac{\partial \mathbf{v}}{\partial t} + (\mathbf{v}\cdot\nabla)\mathbf{v}\right] = \mathbf{J}\times\mathbf{B} - \nabla p \tag{2-5}$$

where p is the plasma pressure nkT, $\mathbf{v}$ is the flow velocity, and ρ is the total mass density mn. Eliminating the time-varying terms from equations 2-4 and 2-5 and removing the small convective term from equation 2-5 gives the following set of equations useful for describing plasma equilibrium:

$$\begin{aligned} \nabla\cdot\mathbf{B} &= 0, \\ \nabla\times\mathbf{B} &= \mu_0\mathbf{J}, \\ \mathbf{J}\times\mathbf{B} &= \nabla p. \end{aligned} \tag{2-6}$$

These equations are then solved in cylindrical-toroidal geometry (R,ϕ,Z), where $\partial/\partial\phi=0$ is used to guarantee toroidal axisymmetry. To simplify the solution, a stream function $\psi(R,Z)$ is introduced [12]:

$$\begin{aligned} \mathbf{B} &= \mathbf{B}_\phi\hat{\mathbf{e}}_\phi + \mathbf{B}_p \\ \mathbf{B}_p &= \frac{1}{2\pi R}\nabla\psi\times\hat{\mathbf{e}}_\phi \end{aligned} \tag{2-7}$$

where $\hat{\mathbf{e}}_\phi$ is the unit vector in the toroidal direction. This stream function can be shown to be equivalent to the plasma poloidal flux:

$$\psi = \int \mathbf{B}_p\cdot d\mathbf{A}. \tag{2-8}$$

The equilibrium solution then becomes a matter of solving for $\psi(R,Z)$. After some manipulations, the following relation may be derived:

$$\Delta^* \psi = -\mu_0 R^2 \frac{dp}{d\psi} - F\frac{dF}{d\psi} \tag{2-9}$$

where

$$F(\psi) = RB_\phi$$

and

$$\Delta^* = R\frac{\partial}{\partial R}\left(\frac{1}{R}\frac{\partial}{\partial R}\right) + \frac{\partial^2}{\partial Z^2}.$$

The functions $p(\psi)$ and $F(\psi)$ are free functions and must be specified. Equation 2-9 is generally known as the Grad-Shafranov equation; it is the standard relation for determining the plasma equilibrium state, specified by $\psi(R,Z)$. The solution to this equation is the value of the flux in the space of interest. The flux is naturally arranged into iso-flux contours which are known as flux surfaces. In discussions of plasma equilibria, the flux surfaces are often displayed in a 2D contour plot. Figure 2-3 is an example of a flux surface plot for the MEDUSA tokamak. Many important plasma quantities (n, T, q) are constant on a given flux surface and hence are functions of the flux ψ.

Solving the Grad-Shafranov equation, however, is not a trivial task. It is a second order non-linear partial differential equation. There are only a few simple closed-form analytic solutions to equation 2-9. The equation is solved numerically in almost all cases of interest. There are many different techniques for solving this equation. The primary method used to reconstruct the equilibria of real plasmas is the technique used in the EFIT code [14,15] (which is also the method employed by the TokaMac 2.0 code used for this thesis.) This method solves the Grad-Shafranov equation subject to the constraints of experimental data (e.g. flux loops, magnetic field measurements, etc.). The technique involves

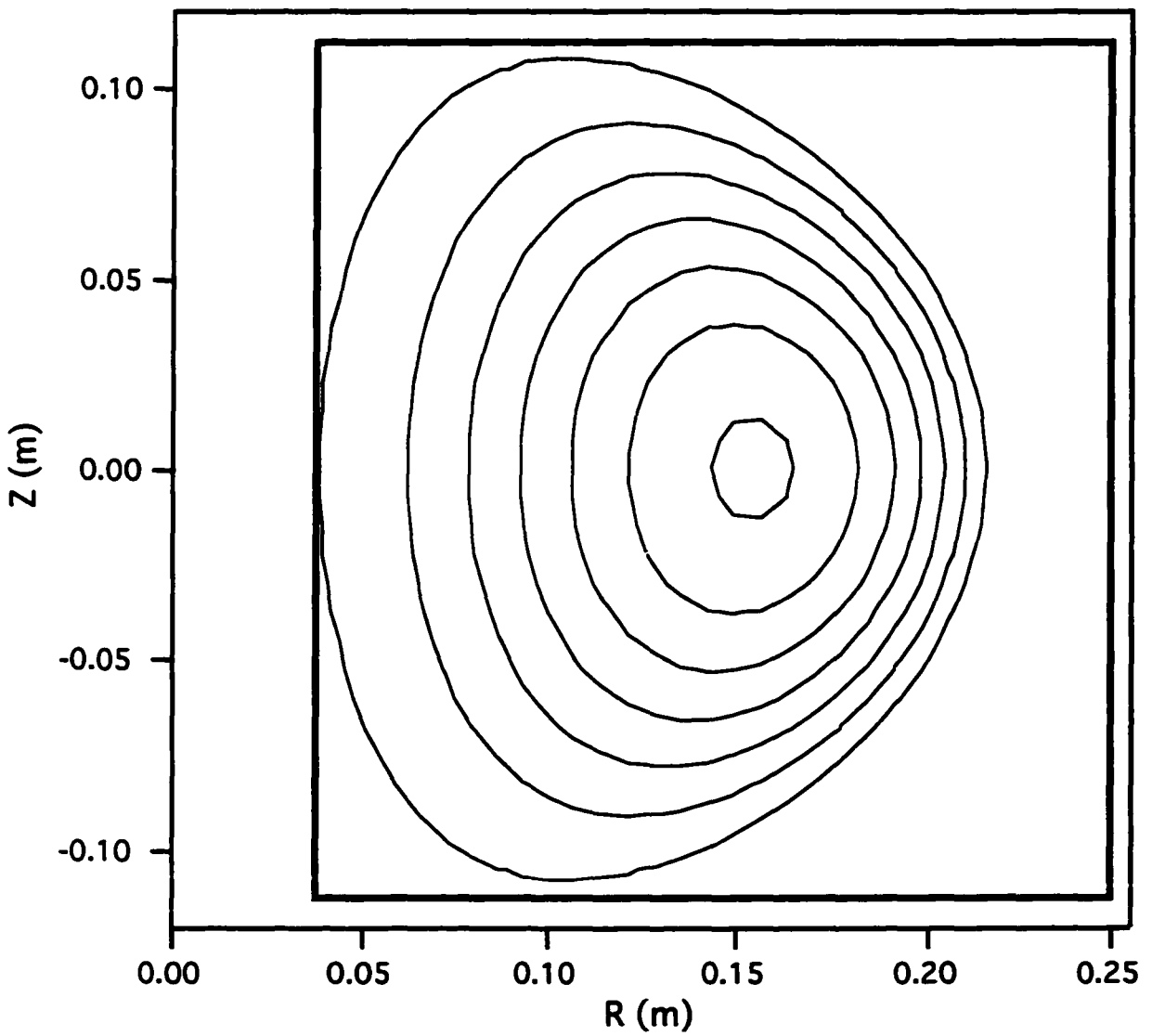

Figure 2-3. Flux surface plot for MEDUSA.

transforming the original problem into a set linearized optimization problems which are then solved with a Picard iteration approach. References 14 and 15 provide more detail on this solution technique.

Once the plasma flux surfaces are determined, many other quantities of interest can be calculated. Some quantities of interest here are the safety factor q, the elongation κ, the ratio of plasma pressure to magnetic field pressure β, the magnetic shear S, the magnetic well W, and the normalized internal inductance ℓ_i.

The safety factor is a function of flux; in fact, flux surfaces are often "named" by their values of q . The value of q is the number of toroidal transits per poloidal transit made by a magnetic field line. It is given by [12]:

$$q(\psi) = \frac{d\Phi/dV}{d\psi/dV} = \frac{F(\psi)}{2\pi}\oint\frac{dl_p}{R^2B_p} \qquad (2\text{-}10)$$

where V is the volume of a flux surface, Φ is the toroidal flux, and the integration is around one poloidal transit. A few particular values of the safety factor are of special interest. The value of q at the magnetic axis (the point where $\nabla\psi = 0$) is known as q_0 . The safety factor at the plasma edge is called q_a or q_ψ. In tokamaks with complex magnetic geometries, the safety factor is often calculated at the 95th or 98th percent flux surface (i.e., the flux surface that contains 95% or 98% of the plasma flux) and is rather obviously named q_{95} or q_{98} . The parameter q_*, known as the "kink safety factor," is the value of q that would be calculated without the effects of toroidicity. It is given as

$$q_* = \frac{2\pi a^2 \kappa B_0}{\mu_0 R_0 I_p} \qquad (2\text{-}11)$$

where a is the midplane half-width of the plasma, B_0 is the toroidal field on axis, and κ is

the elongation, which is discussed below. The kink safety factor is the value of q used when determining plasma stability to edge kink modes, discussed in the next section. The axial safety factor generally has a value near unity for fully formed plasmas; edge values of q are much more variable depending on the particular tokamak, but usually vary between 2 to 20.

Each flux surface also has an elongation κ. In practice, however, usually only the elongation of the last closed flux surface is reported. This value is given by [12,13]:

$$\kappa = \frac{1}{2\pi}\int_0^{2\pi} d\theta \left[\frac{r(\psi_b,\theta)}{a}\right]^2 \qquad (2\text{-}12)$$

where a is the plasma half-width on the midplane and ψ_b is the last closed flux surface. Practically, the elongation is the ratio of the total height of the plasma divided by the width at the midplane (b/a). Values of the elongation typically vary between 0.7 (oblate) to around 3 (highly elongated).

An important figure of merit for tokamaks is known as the plasma beta, or β. The value of beta is an indication of the "efficiency" of the confinement by the magnetic field [12]. There are many different values of beta each with a different purpose. In general, beta can be defined as

$$\beta = \frac{\langle 2nkT\mu_0 \rangle}{B^2} \qquad (2\text{-}13)$$

where $< >$ represents a volume average. Beta-toroidal is defined with respect to the toroidal field, while beta-poloidal (β_p) is defined with respect to the poloidal field. For some definitions of beta the magnetic field is taken as an average, while in others it is not. For this thesis, the definition given in equation 2-13 will be considered appropriate for the total beta.

Often in practice, however, the value of beta is calculated using the vacuum magnetic field, since the real value of the magnetic field may not be known. In some cases, such as strongly paramagnetic spherical tokamaks, this practice can seriously overstate (by 40% or more) the "true" value of beta as given in Equation 2-13. A variation of beta that is important for stability analysis is the normalized beta (or "beta-normal," β_N), which is given as:

$$\beta_N = \frac{aB\beta}{I_p} \tag{2-14}$$

where a is in meters, B is in Tesla, β is the total beta in percent, and I_p is in MA. The normalized beta is used in conjunction with the Troyon stability limit [12,16], which places an empirical limit of 3.5 to 4 on β_N due to ideal MHD modes.

The magnetic shear, S, is an indication of the change of the pitch angle of the magnetic field lines between adjacent flux surfaces. The shear is defined as [12,13]:

$$S(V) = \frac{2V}{q}\frac{dq}{dV} \tag{2-15}$$

where V is the volume of a flux surface. Since V is a function of flux, S can also be expressed as a function of ψ.

The magnetic well is a flux-surface function that is useful in discussions of pressure-gradient driven instabilities. It is closely related to the average curvature of a magnetic field line. A large, positive well is favorable for stability. It is defined as [13]:

$$W = \frac{2V}{\langle B^2 \rangle}\frac{d}{dV}\left\langle \mu_0 P + \frac{B^2}{2} \right\rangle \tag{2-16}$$

where the average is taken over a field line.

The final quantity to be discussed here is ℓ_i, the normalized internal inductance of

the plasma. It is defined as [17]:

$$\ell_i = \frac{1}{\overline{B_p}^2 V} \int_V B_p^2 dV' \qquad (2\text{-}17)$$

where V is the plasma volume, V' is the volume of a flux surface, and the average poloidal field is taken at the plasma edge. The internal inductance is a global value for the equilibrium, and is primarily a function of the shape of the current density profile $J(R,Z)$. In general terms, ℓ_i is a measure of the "peakedness" of the current density profile. For a circular large-aspect-ratio tokamak, a flat current density profile has $\ell_i = 0.5$; a strongly peaked profile might have $\ell_i = 2$, and a very hollow profile might have $\ell_i = 0.2$.

ST Equilibrium

ST plasmas are accurately described by the Grad-Shafranov equation. Most of the differences between ST equilibria and those of conventional tokamaks are matters of degree. Nevertheless, some of these degrees have implications for stability, confinement, and other matters, and are therefore important to understand.

One of the more important features of ST equilibria is the large magnetic shear typically present. Plots of $q(\psi)$, $V(\psi)$, and $S(\psi)$ for a MEDUSA plasma and a comparable conventional tokamak (infinite aspect-ratio) are given in Figure 2-4. Two features in this figure are of particular note. The first is the large gradient of the safety factor in the outer portion of the MEDUSA plasma. This is discussed below. The second is the magnitude of the MEDUSA shear as compared to the conventional tokamak — it is significantly larger throughout the entire plasma. This increased shear plays an important role in many stability issues, to be discussed in the next section. The shear in the center of a high-beta ST will not

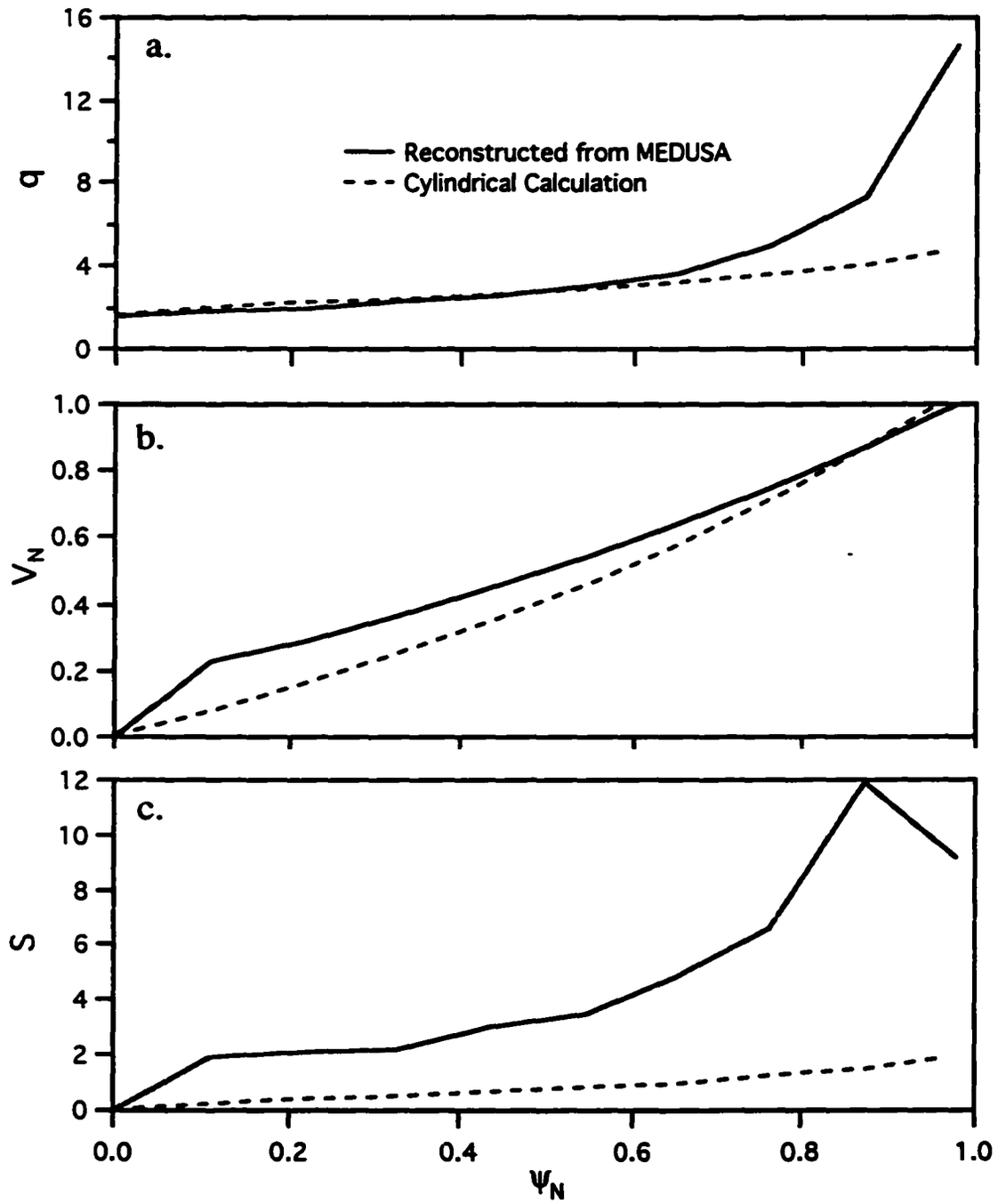

Figure 2-4. Plots of flux-surface quantities for a reconstructed MEDUSA equilibrium and an analytical calculation of a large-aspect-ratio tokamak. Both have $\ell_i = 1$ and $q_0 = 1.63$. The normalized flux ψ_N is the flux divided by the total plasma flux. a.) The safety factor q. b.) The normalized volume (V/V_{tot}). c.) The magnetic shear S.

be large, however, especially if the internal inductance is low. However, the edge shear will still be much larger than that seen in conventional tokamaks.

As alluded to in the previous paragraph, STs feature relatively large values of the edge safety factor, relative to conventional tokamaks operating at the same toroidal field. An approximate value for q_ψ, calculated from a database of free-boundary equilibria, is given by Peng and Strickler [1]:

$$q_\psi = \frac{2.5\times 10^6 aB_\phi}{AI_p}\left(1+\kappa^2\right)f(\varepsilon) = q_*\left(\frac{1+\kappa^2}{2\kappa}\right)f(\varepsilon) \qquad (2\text{-}18)$$

where A is the aspect ratio, ε is the inverse aspect ratio, and

$$f(\varepsilon) = \frac{1.22-0.68\varepsilon}{\left(1-\varepsilon^2\right)^2}.$$

The function $f(\varepsilon)$ is a strong function of aspect ratio; it is plotted as $f(A)$ in Figure 2-5.

A very large edge safety factor (q=30, for example) is of little use in tokamaks. In most cases, STs are run with a combination of lower toroidal field and higher plasma current than would be possible in a conventional tokamak. The high plasma current relative to the toroidal field "rod" current is referred to as "good toroidal field utilization," and is one of the primary advantages of the ST.

The relatively large edge q in spherical tokamaks is a direct consequence of the steep toroidal field gradient. The safety factor quantifies the "twistedess" of field lines within a flux surface; q is the number of toroidal transits a field line makes for each poloidal transit. Since the toroidal field on the inboard of a ST plasma is large compared to other fields in the system, the field line makes a large number of toroidal transits on the inboard (where there is "good curvature," which is stabilizing to ballooning modes) as compared to the outboard

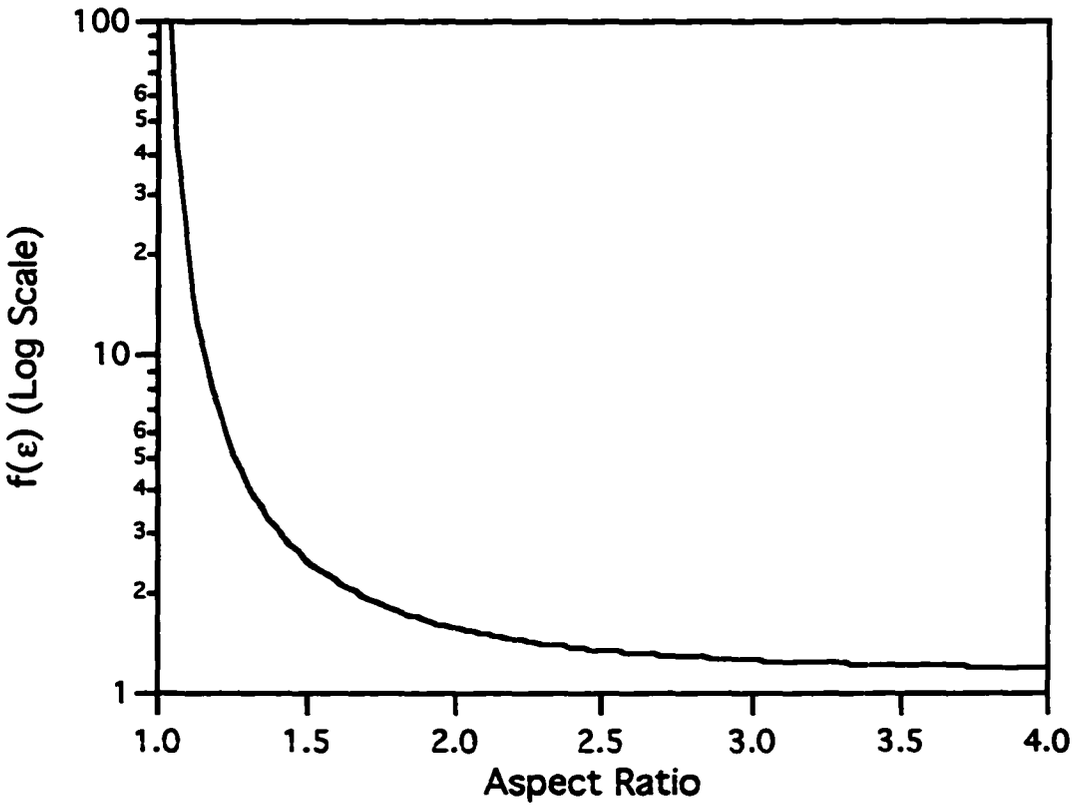

Figure 2-5. The function $f(\varepsilon)$ used in approximating values of q_{ψ} in STs.

where the curvature is "bad.") This can be seen graphically in Figure 2-6, a plot of a field line in a $q = 6$ surface in a Pegasus plasma with A=1.14.

An interesting effect of low aspect-ratio is an increase of the required vertical field over that needed for a conventional tokamak equilibrium. The vertical field (crossing the plasma current) is required to counteract the major radial expansion force of the plasma. This force is due in large degree to the poloidal field crossing the plasma current; the force is outward since the poloidal field is larger on the plasma inboard than the outboard. The required vertical field for a conventional large-aspect-ratio tokamak is given approximately as [18]:

$$B_v \approx \frac{\mu_0 I_p}{4\pi R_0}\left[\ln(8A) + \beta_p + \frac{\ell_i}{2} - \frac{3}{2}\right]. \qquad (2\text{-}19)$$

This equation is inaccurate for low-A tokamaks; it is usually at least a factor of 2 too low. This effect can be attributed to the high toroidicity of the ST; opposite sides of the torus are linked magnetically and increase the poloidal field on the high-field-side above what would be seen in a standard tokamak. A good operational rule of thumb is that spherical tokamaks require approximately the same amount of VF-system current (ampere-turns) as plasma current.

A property of spherical tokamaks is plasma paramagnetism [1,19]. Typically, low-beta tokamaks are slightly paramagnetic, meaning that the plasma toroidal field is greater than the vacuum field. As β_p increases to above 1 (approximately), the plasma becomes diamagnetic. The natural paramagnetism is a result of the poloidal component of the plasma current, which is carried by electrons tied to the field lines. As the rotational transform of the field lines increases (i.e. the safety factor decreases), this effect is magnified. The end result

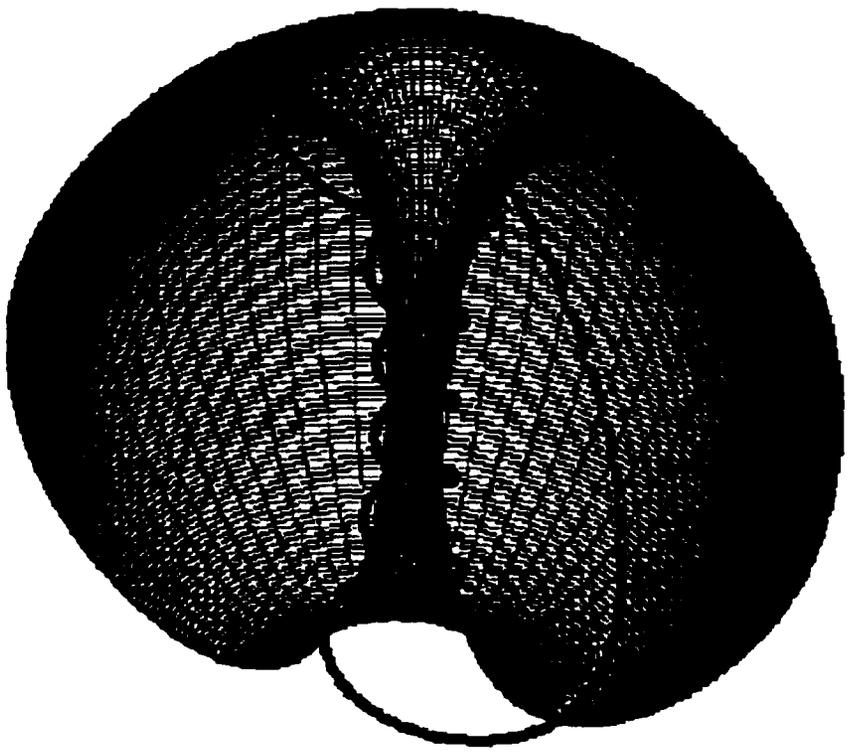

Figure 2-6. Field line plot of the Pegasus ST showing large number of inboard toroidal transits. (Courtesy S. Kruger)

is that STs tend to be more paramagnetic than conventional tokamaks, although this effect is mitigated somewhat by the high betas expected in STs.

A novel feature of ST equilibria is that they are naturally elongated in a straight vertical field [1,20,21]. This is advantageous in that elongation tends to increase the Troyon beta limit, which is discussed in the next section. Conventional tokamaks require shaping coils to achieve this elongation, which make them unstable to n=0 vertical displacement instabilities. Unshaped ST plasmas held in a straight or dipole equilibrium field are stable to these displacements [22].

Another interesting feature of STs is the so-called "natural divertor" (ND) [23,24]. This is a feature of the field lines immediately outside the last closed flux surface. These field lines topologically connect the outboard of the plasma with the center column and the top and bottom inside regions of the vacuum vessel. This connection length can be quite short for low-field STs with tight-fitting vacuum vessels. The natural divertor was originally touted as an advantage of ST plasmas, since it effectively removed much of the scrape-off plasma in the START tokamak [24], where the connection lengths are quite long. It has more recently become clear, however, that the ND can hurt the performance of larger ST plasmas by reducing the plasma edge temperature; this occurs because the divertor strongly couples the plasma edge to the vessel wall [25].

MHD Stability

Magnetohydrodynamic (MHD) stability in tokamaks is a rich and complex subject. A thorough review of this material is far beyond the scope of this thesis. This section, then, will contain a quick overview of the most common kinds of ideal and resistive MHD instabilities seen in tokamaks.

MHD instabilities (in contrast to instabilities arising from plasma kinetic effects) can

be subdivided into two general subcategories: ideal and resistive. (Sometimes neoclassical MHD instabilities are included as a third class; here they will be a "subclass" of resistive instabilities.) Ideal MHD instabilities tend to be better understood since the removal of the plasma resistivity makes the MHD equations much simpler to analyze. However, resistive instabilities are important in many tokamak phenomena such as current transport (see Chapter 3), magnetic islands, and disruptions. Ideal MHD stability will be discussed first; resistivity will be added afterwards.

The first issue to be addressed is the nature of an instability. Many quantities of interest in a tokamak plasma can be linearized about the equilibrium solution into a large steady-state part and a smaller time-dependent part [12]:

$$\xi(\mathbf{r},t) = \xi_0(\mathbf{r}) + \xi_1(\mathbf{r},t). \tag{2-20}$$

The perturbation ξ_1 can be further decomposed into a spatial part and a time-dependent part at a given frequency (or spectrum of frequencies):

$$\xi_1(\mathbf{r},t) = \xi_1(\mathbf{r})e^{-i\omega t}. \tag{2-21}$$

The real part of ω leads to a stable oscillatory solution. The imaginary part of ω gives either exponential growth or decay. If $\mathrm{Im}(\omega) > 0$, the perturbation grows and the system is unstable. Instability can also be ascertained through an energy principle [26]: if the potential energy associated with a perturbation decreases, then the system is unstable.

A second issue to address is the effect of instabilities on the plasma. Some instabilities, for example, the external kink, can lead to disruptions that terminate the plasma. Not all instabilities lead to disruptions, but most degrade the plasma in some way. Magnetic islands, which are usually created by neoclassical tearing modes, tend to hurt plasma confinement by providing a conduit for transport along the separatrices [27]. Double tearing

modes (discussed in detail in Chapter 3) can redistribute the plasma current density where a double-valued q-profile exists. Sawteeth in the plasma core inside the q=1 surface redistribute the plasma pressure [26]. In general, MHD instabilities are harmful to the plasma, particularly the confinement, though they are not always disastrous.

There are three types of ideal MHD instabilities that are of concern for tokamaks: interchange, ballooning, and kink instabilities. The first two derive free energy from the plasma pressure gradient, while the third is driven by the tension of the magnetic field lines. It can be shown that ideal MHD instabilities must preserve the topology of the flux surfaces. Since the resistivity is zero, the plasma is treated as a superconductor. The magnetic field lines move with the plasma fluid and cannot reconnect.

The ideal kink instability is driven by the energy in the plasma current. It represents a resonant distortion on a rational flux surface (i.e., $q = m/n$) where the field lines twist or kink helically on themselves much like a tightly-wound rubber band. For most tokamaks this instability is negligible except for low values of m and n (e.g. 1/1, 3/2, 2/1, 3/1). The external kink, which distorts the entire plasma column, can be quite virulent. It is usually avoided by operating the tokamak such that $q_\psi > 3$. The internal kink occurs on flux surfaces internal to the plasma and generally leads to small distortions of the field lines. The 1/1 internal kink can be suppressed by operating with $q_0 > 1$, although this condition is often violated.

The interchange instability is directly analogous to the Rayleigh-Taylor instability of fluid mechanics [28], where a heavy fluid is supported in an unstable equilibrium by a light fluid. In a tokamak, the heavy fluid and light fluid are replaced by the plasma and the magnetic field, respectively. This mode is generally stable in tokamaks due to the effects of the average "good" field line curvature (i.e., $\nabla B \cdot \nabla p < 0$). The ballooning instability is another pressure-driven mode. It can lead to localized bending and expansion of the field

lines [18,26], much like a weak spot on a balloon or inner tube distorts under pressure.

These pressure-driven instabilities are generally controlled by limiting the plasma beta. It has been found [12,16,29] that tokamaks are stable to essentially all ideal MHD instabilities (including internal and external kinks) if the total beta is limited by

$$\beta \leq 0.035 \frac{I_p}{aB_0} = 0.175 \frac{\kappa}{Aq_*} \qquad (2\text{-}22)$$

where A is the aspect-ratio and I_p is in MA. Equation 2-22 is known as the Troyon beta limit. The second equality is derived from the large-aspect-ratio expansion for q; the primary form of the Troyon limit is the first inequality.

If resistivity is introduced back into the MHD equations, a new set of MHD instabilities results. These resistive instabilities can change the topology of the flux surfaces by reconnecting field lines. Although there are many kinds of resistive instabilities, the only type of interest here is the tearing mode, which is driven by gradients in the current density across rational magnetic surfaces [26,30]. Tearing modes are discussed in more detail below and in Chapter 3.

The primary effect of tearing modes is the production of magnetic islands about rational flux surfaces. (When the effects of parallel viscous stress, i.e. viscosity along field lines, are included, the resultant modes are known as "neoclassical tearing modes" [26].) These islands have several implications for tokamak operation. As mentioned earlier, they tend to short-circuit plasma transport and reduce the confinement, at least locally [27]. Sawteeth are believed to be caused by the 1/1 mode. Tearing modes are likely responsible for various kinds of disruptions [31], locked modes, and the rapid current penetration observed during startup [31-33 and others], all of which are discussed in greater detail in the next chapter.

Stability of ST Plasmas

Perhaps the single greatest advantage of the spherical tokamak over more conventional tokamaks is the improved stability to many MHD modes. The Troyon beta scaling, equation 2-22, implies that decreasing the aspect ratio should increase the ideal beta limit. The second equality in equation 2-22 indicates that elongated, low-aspect-ratio tokamaks should experience elevated beta limits. The Troyon beta limit relation was not derived specifically for low aspect ratio. However, theoretical studies [22,34-36] indicate that the limit should hold for spherical tokamaks. There are also indications that the beta limit actually increases over the Troyon limit for low A [37]. These predictions have now received an experimental verification. The START tokamak [2,24] recently achieved an average toroidal beta of 30% [38], which is almost a factor of three above the previous record. The corresponding value of β_N was approximately 3.9; the beta at the magnetic axis was greater than 60%. These records were achieved transiently using neutral beam heating and fast ramp-down of the toroidal field. Despite their transient nature, though, these plasmas showed no sign of fast-growing ideal instabilities that might have been expected. (It should be noted that these quoted values of beta use the vacuum toroidal field as the reference; this is done primarily for the ease of calculation, in that the plasma paramagnetism is often not readily deduced. The actual values of beta are likely to be somewhat lower due to the plasma paramagnetism.) Finally, it is believed that STs provide a natural path to the region of second stability, where the Troyon beta limit does not apply. This has received no experimental test yet, however.

The lower limit on q_ψ for conventional tokamaks with conducting walls is typically 2 or 3; this limit is set to avoid large ideal kinks. This limit becomes more restrictive at lower aspect ratio, generally requiring $q_\psi > 4$ [16,34]. Since STs naturally tend to produce high

edge safety factors, this condition is generally not much of a limitation. An adjacent stability issue of possible concern for very low-aspect-ratio tokamaks (ULARTs and ELARTs) concerns the n=1 tilt and shift modes often observed on spheromaks. It has been demonstrated that these modes are well stabilized by toroidal fields significantly smaller than that required for stability to edge kinks [19,39,40] and should therefore not be a problem for STs, except possibly at extremely low A (approaching unity).

The stability of tearing modes and neoclassical tearing modes in spherical tokamaks is not very well determined at this point. There are several effects that could come into play in higher-beta spherical tokamaks.

The starting point for the analysis of stability to tearing modes in a ST plasma is the magnetic island evolution equation [41]:

$$\frac{dW}{dt} = 1.2\frac{\eta}{\mu_0}\left[\Delta'(W) - \frac{\Delta_{pol}}{W^3} + \left(\Delta_{neo} - \Delta_{GGJ}\right)\frac{W}{W^2 + W_d^2}\right] \qquad (2\text{-}23)$$

where W is the island width, Δ' is the classical tearing mode drive term, Δ_{pol} is a polarization-current-driven term, and W_d is a threshold island width for the neoclassical driving term and all terms are evaluated at the resistive layer about the rational flux surface. The other terms in equation 2-23 are Δ_{neo}, a bootstrap-current-driven term given roughly by

$$\Delta_{neo} \approx -k\sqrt{\varepsilon}\frac{L_p}{L_q}$$

where k is a constant on the order of 1, and L is the derivative scale length (i.e. $L_x = x'/x$), and Δ_{GGJ}, a finite-beta stabilization term given roughly by

$$\Delta_{GGJ} \approx 6.0\beta_t\frac{L_q^2(q^2-1)}{rL_p}.$$

The last term is known as the Glasser-Greene-Johnson term after its originators [42,43]. The GGJ term is relatively large for low aspect-ratio, high-q plasmas. However, it still may not be large enough to dominate neoclassical effects in STs, which are very profile sensitive [41].

There are further effects of toroidicity on tearing modes in spherical tokamaks. One of these is the coupling of unstable modes due to the effects of toroidicity [44]. For finite values of beta and finite aspect ratios, unstable modes with poloidal number m and toroidal number n can couple to other modes with the same value of n and adjacent values of m (e.g. 3/1 coupling to 2/1 and 4/1.) This coupling complicates the discussion of tearing modes in spherical tokamaks, since single unstable modes may be impossible to identify. There are also indications that the saturated islands widths in spherical tokamaks will be significantly smaller (in terms of W/a) than in conventional tokamaks, even with the presence of coupling-induced "satellite modes" [45].

The discussion of tearing modes in STs is enhanced by an interesting note from some operating experiments—the plasmas are seen to be "resilient" to current terminating disruptions. START and MEDUSA in particular have seen a surprising absence of disruptions in most cases. (These plasmas do see disruptions, however, which is why the term "resilience" is employed over the stronger phrase "disruption immunity" originally used [46,47].) This disruption resilience leads to plasmas which are typically disruption-free, except when mistreated (strongly compressed into the inner wall, limiting against an internal coil). The shortage of disruptions is intriguing given the possibility of small saturated island widths in STs and the presumption that disruptions can be caused by overlapping islands with "incommensurate helicities" [26]. These experiments do see a phenomenon that has been dubbed an internal reconnection event, or IRE. An IRE is similar to a soft disruption in that it results in a current spike and a negative loop-voltage spike. However, IREs do not

necessarily lead to termination of the plasma current. IREs are believed to be a result of resistive MHD activity. Internal reconnection events will be discussed in more detail in Chapters 3 and 6.

Tokamak Confinement Scaling

The ultimate purpose of a tokamak, by most measures, is to confine a thermonuclear plasma that would be the heart of a fusion power station. In the early days of fusion research, it became apparent that the plasma was not confined nearly as well as expected by classical (coulomb-collision-induced) diffusion arguments. Much research has been directed toward understanding the processes that actually cause this anomalous transport.

To help achieve a basic understanding of tokamak confinement, zero-dimensional scaling relations have been derived from experimental data. There are many such relations, each derived for different sorts of plasma conditions (collisionality, L- or H-mode, auxiliary heated, etc.) and machine classes. All of these relations relate various plasma and device parameters, such as I_p and R, to the plasma energy confinement time, given as:

$$\tau_E = \frac{W}{P_{in}} \tag{2-24}$$

where τ_E is the energy confinement time, W is the plasma stored energy, and P_{in} is the input power to the plasma. These relations presuppose a macroscopic steady-state in the plasma.

Following are a few of the many scaling relations that are used. In the following, τ_E is the energy confinement time in seconds, R and a are the major and minor radii in meters, n is the plasma density divided by 10^{19} m^{-3}, I_p is the plasma current in MA, M is the average mass number of the plasma ions (AMU), κ is the elongation, B is the toroidal field

at the magnetic axis in Tesla, P is the input power in MW, Z is the average number of electrons per plasma ion, q_{cyl} is the cylindrical value of the safety factor, and ε is the inverse aspect-ratio.

Neo-Alcator scaling is a conventional relation for ohmically heated tokamaks [48]:

$$\tau_{E,N-A} = 1.92 \times 10^{-21} \bar{n}_e R^2 a. \tag{2-25}$$

One of the most-used scaling laws in recent years has been one derived for L-mode confinement in the International Thermonuclear Experimental Reactor (ITER); it is known as ITER-89P [49]:

$$\tau_{E,ITER-89P} = 0.051 M^{0.5} I_p^{0.85} R^{1.2} a^{0.3} \kappa^{0.5} n^{0.1} B^{0.2} P^{-0.5}. \tag{2-26}$$

A scaling relation which attempts to take plasma turbulence into account (through a "critical electron-temperature-gradient" model) is that of Rebut, Lallia, and Watkins [50]:

$$\tau_{E,RLW} = 36.8 M^{0.5} I_p^{0.5} \bar{n}_e^{0.75} B^{0.5} Z^{0.25} \ell^{2.75} P^{-1} + 17.0 M^{0.5} I_p \ell^{1.5} Z^{0.5} \tag{2-27}$$

$$\text{where } \ell = \left(R a^2 \kappa\right)^{1/3}.$$

As a final example, the Lackner-Gottardi scaling relation is based on transport in the "plateau" region of collisionality [51]:

$$\tau_{E,L-G} = 0.03 \sqrt{\frac{M}{2}} I_p^{0.8} R^{1.8} a^{0.4} \left(\frac{\bar{n}_e}{P}\right)^{0.6} \frac{q_*^{0.4}}{f(\varepsilon)} \frac{\kappa}{\left(1+\kappa\right)^{0.8}}. \tag{2-28}$$

ST Confinement

Most of the empirical data on confinement in spherical tokamaks comes from the START experiment. This is obviously a limited data set. These results show, though, that ST confinement should be quite good compared to conventional tokamaks. Early results from START [52] indicated that the Rebut-Lallia and Lackner-Gottardi scalings represented the confinement data well, while the neo-Alcator scaling underpredicted the START results. Some more recent results [53] have confirmed that the Rebut-Lallia-Watkins and Lackner-Gottardi scalings accurately predict START electron temperature data. The START group has also invented a modified neo-Alcator scaling that takes aspect-ratio explicitly into account, and that seems to explain the ohmically heated START discharges fairly well:

$$\tau_{E,NA-S} = 6.0 \times 10^{-22} \overline{n}_e R^2 a q_* \left[\frac{\kappa A}{A-1} \right] \qquad (2\text{-}29)$$

where the conventions on units are the same as before. This expression is essentially the same as the regular neo-Alcator scaling (equation 2-25) with the addition of factors for elongation, safety factor, and aspect ratio. These terms will generally be small for conventional tokamaks, but they indicate increased confinement for elongated, low-A tokamaks.

One of the possible reasons for this decrease in transport in STs is the predicted reduction in width of saturated magnetic islands [45], which could reduce streaming transport losses along the island separatrices. There are also theoretical predictions of improved stability properties against high-n microinstabilities in ST plasmas. These microinstabilities include high-mode-number ballooning modes [54,55] and drift waves (trapped electron η_i modes) [55]. Since these types of microinstabilities are believed to be responsible for anomalous transport, their reduction in STs would seem to indicate an

improvement in confinement.

Other Physics Issues

In addition to the equilibrium, stability, and confinement issues already discussed, there are a few other physics properties that distinguish spherical tokamaks from the conventional variety. These include resistivity enhancement at low-A, increased bootstrap current, and single particle orbits. These topics will be briefly addressed in this section.

It is generally inappropriate to analyze the resistivity of a hot tokamak plasma with the simple Spitzer model. There are many phenomena that force the tokamak away from simple, collisional Spitzer resistivity. These processes are driven by neoclassical effects, which for the most part are caused by particles trapped by the gradient of the toroidal field. For a collisionless, cylindrical tokamak plasma, Ohm's law may be approximated on each flux surface by [26]:

$$J_{\parallel} = \frac{\sigma_{\parallel}}{1+\sqrt{\varepsilon}} E_{\parallel} - \frac{\sqrt{\varepsilon}}{1+\sqrt{\varepsilon}} \frac{1}{B_{\theta}} \frac{d}{dr}\left[p_e + \frac{p_i}{Z_{eff}} \right] \tag{2-30}$$

where $E_{\parallel}$ is the inductive electric field, $\sigma_{\parallel}$ is the classical conductivity, and all relevant quantities are evaluated on each flux surface. The first term on the right-hand side represents a trapped-particle correction to the classical conductivity. The second term represents a self-current, or bootstrap current, term.

The trapped particle fraction on a tokamak flux surface is

$$f_t = \sqrt{1 - \frac{B_{min}}{B_{max}}} \approx \sqrt{\frac{2\varepsilon}{1+\varepsilon}} \tag{2-31}$$

where the second equality is true for low-beta plasmas, and the entire expression is only

meaningful for collisionless plasmas. Here ε applies to each flux surface rather than the entire plasma. The second expression on the right-hand side is on the order of $\varepsilon^{1/2}$. For the outer flux surfaces in a ST, where ε is large, the trapped particle fraction can approach unity.Since trapped particles cannot carry plasma current, the resistivity increases with increasing trapped particle fraction. This phenomenon is known as "resistivity enhancement," where the enhancement is relative to Spitzer resistivity. The evaluation of the resistivity enhancement for an entire plasma is of course more complex than this; it requires knowledge of the current density, loop voltage, collisionality, and aspect ratio for each flux surface. Sample calculations of this enhancement for a parabolic temperature profile [56] indicate an enhancement of 1.5 for A=6, 2.5 for A=3, 4.5 for A=1.5, and 7 for A=1.1. This increased resistivity makes ohmic current drive more difficult at low A, but makes ohmic heating more effective.

If the outer regions of a ST plasma are collisional, i.e., in the Pfirsch-Schlüter regime of collisionality, then an additional effect may contribute to the toroidal current. The diffusive flux of particles in the Pfirsch-Schlüter regime leads to a pressure-gradient-driven current parallel to the magnetic field [26,57]. This current averages to zero over each flux surface. However, it can contribute locally to the current density profile which and thereby affect the stability of kink and tearing modes. In spherical tokamaks there may be some net positive contribution to the total toroidal current from this ∇p driven term.

The second term on the right-side of equation 2-31 represents the bootstrap current. This bootstrap current provides a large fraction of the plasma current in most reactor designs (including "fully bootstrapped" plasmas with 98-99% of the total current being self-driven.) This bootstrap current is brought about by toroidal momentum exchange between trapped particles (which carry a small diamagnetic current due to the finite width of the banana

orbits) and the passing particles [58]. The ratio of bootstrap current to driven current is proportional to $\varepsilon^{1/2}\beta_p$ [26], which is somewhat favorable to spherical tokamaks because of the weak inverse aspect-ratio scaling and the high beta. The bootstrap current fraction also scales with q^2 if β_T is held constant; this suggests that operation at low q is not the best option for a reactor, especially a high-beta ST [35]. There is also some indication [35] that the bootstrap current may scale more favorably than $\varepsilon^{1/2}\beta_p$ at low aspect-ratio. In fact, recent results have indicated that, as the aspect-ratio approaches unity, the bootstrap current does not vanish if the plasma is collisional; this is due to the large parallel viscosities along field lines at low A [59].

There are several intriguing possible single-particle effects in spherical tokamaks. At the outboard of an ST plasma, the mod-B surfaces are nearly parallel to the flux surfaces (a condition known an "omnigeneity"). In this region, particle drift orbits will nearly coincide with flux surfaces. It is predicted that the resultant narrow banana orbits will lead to reduced neoclassical transport [1]. In addition to this effect, a high-beta ST will have strongly modified mod-B surfaces such that the minimum-B location is not on the outboard midplane [60]; the effect of this field shaping will be trapped particle orbits located entirely above or below the midplane. It has been suggested that these orbits may have an effect on trapped-particle instabilities and hence plasma transport. However, the effects of these orbits are far from clear; it has been suggested that ST trapped-particle orbits are both stabilizing [61] and destabilizing [60]. A final issue worth noting is the size of the neutral beam particle orbits. Since in general the total field in a ST is small compared to a conventional tokamak, yet comparable beam energies are required for heating, large ion gyroradii will be produced. For example, a 50 keV deuterium ion in a 0.2 Tesla field has a gyroradius of 18.8 cm, which can be a substantial fraction of the plasma radius. This issue must be taken into account

when designing heating and diagnostic systems for ST plasmas.

2.3 Spherical Tokamak Experiments

There are currently five operating spherical tokamak experiments in the world, and at least six others currently under construction. This section reviews these experiments and their results. Although MEDUSA is included in the group of operating experiments, it will not be discussed explicitly in this section. Also, there are a few spheromak/tokamak hybrid experiments (notably TS-3 [19,39] and SPHEX) that will not be discussed here. Table 2-1 contains a summary of the major parameters of these devices. The values given in this table are taken from various references which are not necessarily all consistent. Some parameters may represent maximum achievable values, while others are meant to be "typical" values. The listings should only be taken as a guide. Figure 2-7 shows the relative sizes of many of these ST experiments.

Operating Experiments

The premier spherical tokamak operating today is the Small Tight-Aspect-Ratio Tokamak (START) located at the Culham Laboratory in Abingdon, U.K. [2,3,24,46, 47,52,56,62]. START is in many respects a very conventional tokamak; it relies on ohmic induction for startup and current drive, and has recently begun using a neutral beam [63] to heat the plasma. START was the first experiment (1991) to produce significant tokamak plasmas in a low-aspect-ratio geometry. The primary mission for START has been to demonstrate the supposed advantages of spherical tokamaks. It has demonstrated good toroidal field utilization, natural elongation, the "natural divertor," and high energy

Device	R (cm)	a (cm)	I_p (kA)	B_T (T)	Δt_{pulse} (ms)
Operating Experiments					
CDX-U [39,65]	34	22	100	0.13	20
HIT [5]	30	20	250	0.46	10
MEDUSA	12	8	40	0.5	2
START [56]	32	26	300	0.5	50
TST [70,71]	40	35	20	0.2	5
Under Construction					
ETE [72]	30	20	400	0.8	20
GLOBUS-M [73]	35	22	300	0.5	200
HIT-II [74]	30	20	250	0.46	20
MAST [75]	90	70	2 MA	0.65	5 s
NSTX [76]	85	68	1 MA	0.3	5 s
PEGASUS [78]	40	36	300	0.15	50

Table 2-1. Major parameters of several spherical tokamak experiments.

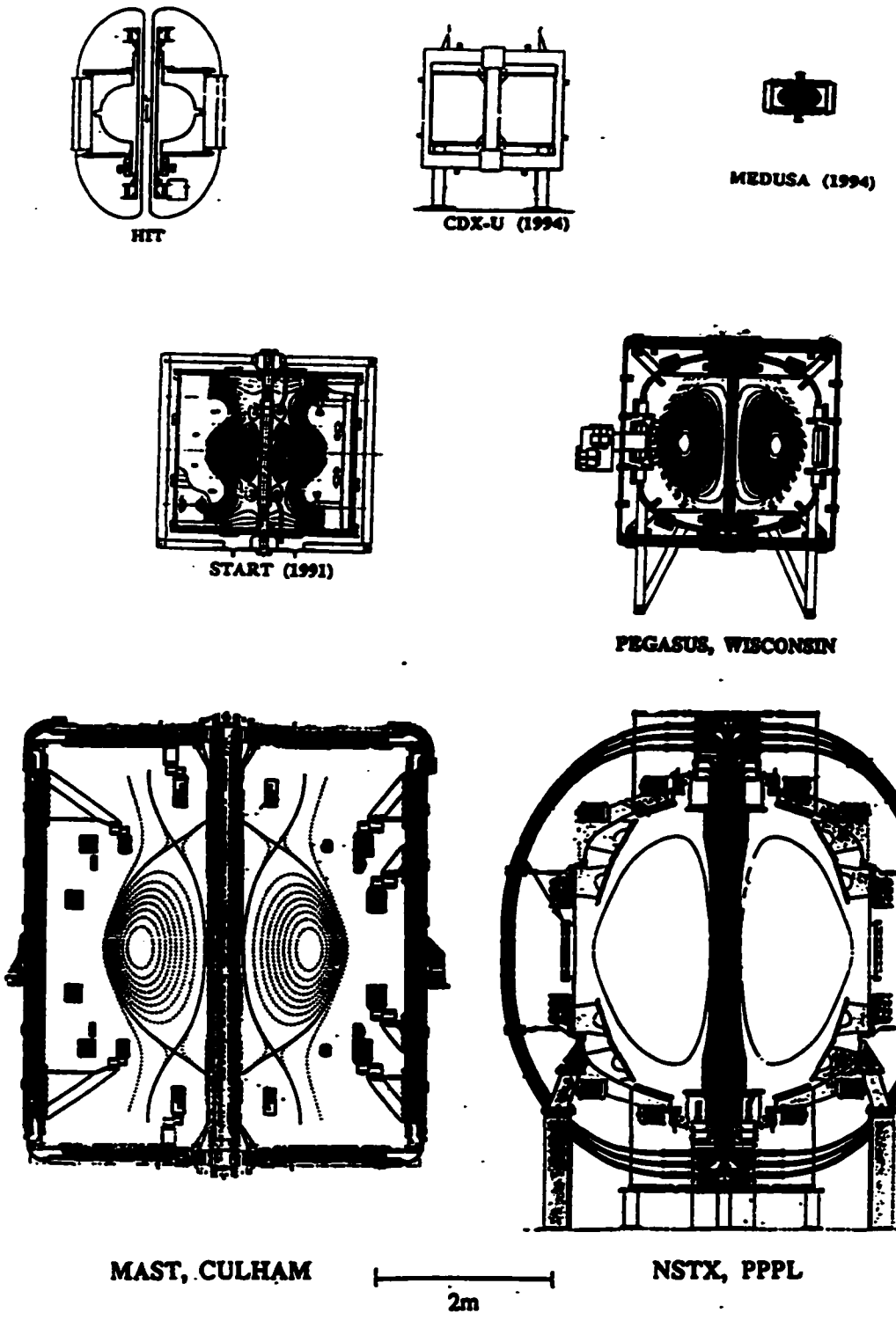

Figure 2-7. Relative sizes of several ST experiments.

confinement. One of the more interesting results from START is the near-disruption free operation it has experienced, which could be a great boon to STs if this behavior extrapolates to larger devices. The observation of IREs on START was duplicated first by MEDUSA and then by CDX-U. Finally, START has dramatically demonstrated the high-beta potential of spherical tokamaks. Recent experiments have transiently achieved values of β_T as high as 30% [38], shattering START's previous record of approximately 13%, which exceeded the 12.6% previously achieved in DIII-D [64]. START will be shut down in 1997 at about the time when MAST is to begin operating.

The Current Drive eXperiment-Upgrade (CDX-U) [39,65] is a low-aspect-ratio tokamak located at the Princeton Plasma Physics Laboratory near Princeton New Jersey. The mission of CDX-U was originally to investigate non-inductive current drive techniques such as DC helicity injection [66]. CDX-U has recently begun to investigate more general aspects of ST physics. Examples include analysis of resistive MHD modes [67], halo currents caused by "artificial" disruptions and IREs, edge q limits, and fast wave heating. There are also plans to implement high-harmonic fast wave (HHFW) current drive experiments in the near future.

The Helicity Injected Tokamak (HIT) [5,68,69] is located at the University of Washington in Seattle, Washington. As its name suggests, HIT is dedicated to studying coaxial helicity injection (CHI) [4], which is essentially a method of steady-state current drive in tokamaks. Helicity is equal to the volume integral of $\mathbf{A}\cdot\mathbf{B}$ over the plasma, and is roughly proportional to the plasma current. It dissipates on the resistive diffusion time scale. Helicity is "injected" into the tokamak inductively, via ohmic heating; it can also be injected by applying a bias voltage to an external flux surface that links the plasma. This method, with coaxial, axisymmetric electrodes, is the method used to operate HIT. Most of the

research on this experiment has been dedicated to characterizing the plasma parameters, including density, temperature, and current profiles, and examining MHD behavior. HIT is currently being upgraded to HIT-II.

The Tokyo Spherical Tokamak (TST) [70,71] is an extremely low-aspect-ratio (ELART; A<1.2) tokamak located at the University of Tokyo in Japan. It is a relatively modest experiment designed to investigate some of the physics phenomena in ELARTs. The topics for study include startup with very limited flux, stability to ideal MHD limits, and magnetic fluctuations.

Experiments Under Construction

Both the Experimento Toroidal Esférico (ETE) [72] and GLOBUS-M [73] are START-sized spherical tokamaks currently under construction, although both are delayed indefinitely due to budget limitations. ETE (the name translates to "Spherical Torus Experiment") is an experiment planned to be built at the Instituto Nacional de Pesquisas Espaciais (National Institute of Space Research) in São José dos Campos, Brazil. The proposed mission of ETE (1986) was to study spherical tokamak physics in general, and to examine steady-state current drive techniques. GLOBUS-M is to be built at the Ioffe Institute in Saint Petersburg, Russia. The research on GLOBUS-M will focus on scaling studies, divertor studies, configuration optimization, ion cyclotron and lower hybrid heating, and fast wave and lower hybrid current drive.

The HIT-II upgrade to the Helicity Injected Tokamak [74] involves replacing the thick-walled copper flux conserver of HIT with a thin-walled vacuum vessel. The poloidal field will be provided by sets of active-feedback coils. HIT-II will feature a 50 mV-s ohmic solenoid for direct comparisons of the effects of CHI and OH. It will have an increased pulse length of up to 20 ms. HIT-II also will have an improved diagnostic set and better

vacuum conditioning than HIT. It begins operation in 1997.

The Mega-Amp Spherical Tokamak (MAST) [75] is the successor experiment to START at Culham. MAST is significantly larger that START, although its physical design is quite similar. It will be primarily an ohmic, neutral-beam-heated tokamak. The primary purposes of MAST are to create ST plasmas comparable to other large tokamaks to allow a fair cross-concept comparison, obtain data for the design of a volumetric neutron source, and to extend the tokamak database to include larger STs. The physics topics to be studied include confinement and transport, MHD stability, current drive techniques, and divertor physics. MAST is expected to begin operation in mid-1998.

The National Spherical Tokamak eXperiment (NSTX) [76] is a large ST at the Princeton Plasma Physics Laboratory. It is similar in size to MAST. Its primary mission is to prove the important principles of a collisionless spherical tokamak: non-inductive startup, good confinement, ideal and resistive stability, attainment of high beta, and power and particle handling [77]. One of the features distinguishing NSTX from MAST is a heavy reliance on coaxial helicity injection for current drive. This will also allow a much more significant test of CHI than has been previously available. NSTX should begin operation in 1999.

The Pegasus Toroidal Experiment [78] is an extremely-low-aspect-ratio tokamak approximately the same size as TST. It is under construction at the University of Wisconsin in Madison. The central feature of Pegasus is a unique high-stress solenoid core which provides a large (120 mV-s) amount of ohmic induction in the ELART geometry. Pegasus will use this ohmic heating and fast wave heating to achieve very high toroidal beta (40% or higher.) The goals of the Pegasus program are to extend ST operation to the extreme limit of high toroidal field utilization and to explore the limitations of this region of parameter space. Pegasus is expected to begin operation in early 1998.

2.4 Spherical Tokamak Engineering Issues

The primary goal of fusion research is to develop a working fusion power reactor. With this in mind, there are many motivations to study spherical tokamaks: high beta, low toroidal field, disruption resilience, and (possibly) high confinement are chief among them. These issues mark the ST as a promising technology for a fusion-based power plant [3,16,79-81] or volumetric neutron source [3,79,82]. Yet there are practical matters that must also be considered if the ST is to be developed into a feasible commercial endeavor. These issues will be discussed in this section. The engineering problems of tokamaks in general, such as non-inductive current drive, tritium breeding, and superconducting magnets, will not be discussed in this section. It should be remembered, however, that the solution to these problems is crucial to the development of tokamak fusion reactors.

Advantages

Perhaps the greatest advantage of the ST as a reactor is the small physical size of the nuclear island, which is the energy-producing part of the plant. Current fusion reactor concepts compare rather unfavorably with the present generation of light water reactors, which should be expected to improve further. The ARIES-IV fusion power plant concept has a mass-power density (MPD) of 11 kWe per tonne of nuclear island mass, and an electric energy gain (Q_E) of 5.2; a typical PWR, by contrast, has a MPD of 800-1,000 kWe/tonne and Q_E = 20-30 [83]. Since the cost of a power plant tends to scale with the mass of the nuclear island, it is immediately obvious that, even if an "advanced physics" tokamak reactor such as ARIES-IV were built, it would likely be uncompetitive in the market. The good news for spherical tokamaks is that, if they can produce levels of electrical output similar to ARIES-IV, they will result in significantly smaller reactors and higher MPDs, in the range of 200-600 kWe/tonne [16].

Another advantage of low-aspect-ratio tokamak reactors is the increased Troyon beta limit. Spherical tokamaks will allow hotter, denser plasmas than the current first-stability limit for conventional tokamaks, and may provide a simple means to access the region of second stability. This high beta may in turn provide a path to advanced fuels cycles such as the neutron-lean (D,^{3}He) cycle. This cycle allows another significant advantage: because the products are charged particles (a proton and an alpha particle), direct energy conversion techniques could conceivably be used to generate electricity. These techniques give net efficiencies much greater than those allowed by the standard Rankine cycle. This efficiency increase would lead to a significant decrease in the cost of electricity produced by these reactors.

Another possible advantage of ST reactors is improved stability to hard disruptions. If the dearth of disruptions observed on START and MEDUSA is reproduced on larger ST experiments, it would represent a major advantage for the ST reactor concept. Disruptions are a major constraint on the operation of large tokamaks. Much effort is made to avoid them. When they do occur, they can often stop experimental runs for hours or days. A disruption creates large, non-axisymmetric electromechanical forces in and around the vacuum chamber; these are particularly bad when they are caused by halo currents flowing in the vessel itself. Meanwhile, the disrupted plasma can sputter large quantities of the limiting surfaces into the vacuum vessel. A tokamak power reactor would have to be designed to withstand such forces and impurities, which would add greatly to its cost. It would also have to be operated conservatively to avoid causing many disruptions. Moreover, any disruptions in a tokamak reactor would lead to an interruption of electricity generation. A disruption-stable ST could significantly reduce the costs associated with these problems and result in a much more attractive reactor. If the disruption "immunity" of STs is not demonstrated in the next generation of larger experiments, these devices may still posses

an advantage over conventional tokamaks with regard to disruption behavior. Recent results [84] from CDX-U indicate that disruption-induced halo currents in forced ST disruptions may be significantly smaller than those in conventional tokamaks, greatly reducing the asymmetric forces on the vacuum vessel associated with these currents.

There are several other possible advantages to ST reactors. The predicted large bootstrap fraction could result in reduced current drive requirements. Smaller banana orbits and magnetic islands could reduce transport. Stabilized microturbulence could do the same. Good toroidal field utilization would reduce the toroidal field requirements, although there are complications with the toroidal field magnets in a ST reactor which are discussed in the next section. All of these phenomena represent potential gains over conventional tokamaks.

Problems

Balancing the potential advantages of ST reactors discussed above are a number of problems. These problems are all essentially caused by the relatively small radius of the bore of the torus ($b = R\text{-}a$). The small size of this region limits the amount of equipment that may be placed there, and has effects on startup, current drive, diagnostics, and the toroidal field system.

The toroidal field system of a ST reactor will likely have to contain a normally conducting, resistive inner leg. A superconducting TF center column is generally considered to be out of the question [16,80,81,83] due to the large heat load from fusion neutrons. The TF rod poses several difficulties from an engineering standpoint. First, a resistive rod requires some fraction of the recirculating power for coil current drive. Estimates of the total fraction of recirculating power are typically around 20%, while the fraction required for the TF rod are around 8% [79,80]. Second, the rod will require cooling. The TF leg for a ST power plant will likely dissipate tens to hundreds of megawatts of resistive heat, in addition

to neutron heating of about the same magnitude [16,79]. Cooling will be required to maintain the conductivity of the rod, minimize creep, and prevent melting. Third, since the rod cannot be shielded from fusion neutrons, radiation damage is a major concern [85]. Among the effects will be radiation hardening, embrittlement, radiation-assisted creep, and a reduction in the ultimate strain. Additionally, neutron absorption reactions will produce hydrogen and helium gas in the matrix. Radiation damage will likely limit the lifetime of the rod to one year [16]. Finally, the power supplies for such a coil would be nontrivial, requiring a DC current supply at high currents (MA) and low voltages, or lower currents and higher voltages.

The limited space available in the inner bore of a ST reactor also places a severe restriction on the use of an ohmic solenoid to start up the plasma, and almost completely rules out the use of a solenoid to drive current. Most designs for ST reactors eliminate the ohmic solenoid altogether [16,80,81,83]. There are of course various means for non-inductively driving current in a tokamak, including coaxial helicity injection, Alfvén waves, high harmonic fast waves, and neutral beams. It may still be advantageous to rely on external magnetic flux to start up a tokamak reactor when it is necessary. Ohmic induction is a well-understood and highly efficient method for starting tokamak discharges. Possibilities for a ST reactor include the induction-compression method employed on START initially, and a very small startup solenoid in the central bore.

The small central bore of a ST reactor would also limit the use of various kinds of auxiliary equipment on the inner wall. A breeding blanket, for example, could not be used on the center post without compromising the aspect ratio. Similarly, articles such as antennas, beam dumps, and lasers will not be available on the inner wall. Very small diagnostics, such as magnetics, could conceivably still be used on the center post, although their utility would be limited in a steady-state tokamak.

2.5 References

1. PENG, Y-K.M., STRICKLER, D.J., Nucl. Fusion **26** (1986) 769.
2. SYKES, A., Plasma Phys. Control. Fusion **36** (1994) B93.
3. ROBINSON, D.C., et al., Fusion Technol. **30** (1996) 1360.
4. JARBOE, T.R., Fusion Technol. **15** (1989) 7.
5. NELSON, B.A., JARBOE, T.R., ORVIS, D.J., et al., Phys. Rev. Lett. **72** (1994) 3666.
6. KUBO, S., NAKAMURA, M., et al., Phys. Rev. Lett. **50** (1983) 1994.
7. JOBES, F., STEVENS, J., Phys. Rev. Lett. **52** (1984) 1005.
8. TOI, K., OHKUBO, K., et al., Nucl. Fusion **28** (1988) 147.
9. WUKITCH, S., VUKOVIC, M., et al., Phys. Rev. Lett. **74** (1995) 2240.
10. MAJESKI, R., NSTX Research Forum, Princeton N.J., February 5, 1997.
11. WOOTTON, A.J., et al., USTX: The University Spherical Torus Experiment, Proposal to the U.S. Department of Energy, 1996.
12. FREIDBERG, J.P., *Ideal Magnetohydrodynamics*, Plenum Press, New York, 1987.
13. FONCK, R.J., Lecture Notes, NEEP 527, University of Wisconsin-Madison, 1992.
14. LAO, L.L., St. JOHN, H., STAMBAUGH, R.D., et al., Nucl. Fusion **25** (1985) 1611.
15. LAO, L.L., et al., Nucl. Fusion **30** (1990) 1035.
16. HENDER, T.C., et al., Plasma Physics and Controlled Nuclear Fusion Research 1992 (Proc. 14th Int. Conf., Würzburg, 1992), Vol. 3, IAEA, Vienna (1993) 399.
17. LLOYD, B., JACKSON, G.L., TAYLOR, T.S., et al., Nucl Fusion **31** (1991) 2031.
18. STACEY, W.M., *Fusion: An Introduction to the Physics and Technology of Magnetic Confinement Fusion*, John Wiley & Sons, New York, 1984.
19. YAMADA, M., MORITA, A., et al., Trans. of Fusion Tech. **27** (1995) 161.
20. KALMYKOV, S.G., Sov. J. Plasma Phys. **18** (1992) 685.

21. ROBERTO, M., Nucl. Fusion **32** (1992) 1666.

22. HOLMES, J.A., et al., Phys. Fluids B **1** (1989) 358.

23. PENG, Y-K. M., et al., Plasma Physics and Controlled Nuclear Fusion Research 1994 (Proc. 15th Int. Conf., Seville, 1994), Vol. 2, IAEA, Vienna (1995) 643.

24. SYKES, A., et al., Plasma Physics and Controlled Nuclear Fusion Research 1994 (Proc. 15th Int. Conf., Seville, 1994), Vol. 1, IAEA, Vienna (1995) 724.

25. MIODUSZEWSKI, P., at the NSTX Research Forum, Princeton NJ, February 5, 1997.

26. CALLEN, J.D., "Models of Plasma Confinement and Heating in Tokamaks", U. of Wisconsin Center for plasma Theory and Computation Report UWPR 89-2, 1989.

27. CHANG, Z., FREDRICKSON, E.D., CALLEN, J.D., MCGUIRE, K.M., et al., Nucl. Fusion **34** (1994) 1309.

28. SCHMIDT, G., *Physics of High Temperature Plasmas*, Academic Press, New York, 1979.

29. TROYON, F., et al., Plasma Phys. **26** (1984) 209.

30. HEGNA, C.C., and CALLEN, J.D., Phys. Plasmas **1** (1994) 2308.

31. STIX, T.H., Phys. Rev. Lett. **36** (1976) 521.

32. CARRERAS, B., HICKS, H.R., and WADDELL, B.V., Nucl. Fusion **19** (1979) 583.

33. MAHAJAN, S.M., and HAZELTINE, R.D., Nucl. Fusion **22** (1982) 1191.

34. BESPOLUDENNOV, S.G., Sov. J. Plasma Phys. **12** (1986) 441.

35. MILLER, R.L., et al., at the Workshop for Establishing the Physics Basis Needed to Access the Potential of Compact Toroidal Reactors, Oak Ridge, TN, July 19, 1994.

36. CHARLTON, L.A., LEBOEUF, J-N., CARRERAS, B.A., Bull Am. Phys. Soc. **39** (1994) 1700.

37. JARDIN, S.C., et al., at the Workshop for Establishing the Physics Basis Needed to Access the Potential of Compact Toroidal Reactors, Oak Ridge, TN, July 19, 1994.

38. SYKES, A., Private communication to R. Fonck, April 7, 1997.

39. HWANG, Y.D., YAMADA, M., et al., Plasma Physics and Controlled Nuclear Fusion Research 1994 (Proc. 15th Int. Conf., Seville, 1994), Vol. 1, IAEA, Vienna (1995) 737.

40. BRUHNS, H., BRENDEL, R., et al., Nucl Fusion **27** (1987) 2178.

41. KRUGER, S.E., HEGNA, C.C., CALLEN, J.D., "Geometrical Influences on Neoclassical Magnetohydrodynamic Tearing Modes," Report UW-CPTC 97-10, July 1997.

42. GLASSER, A.H., GREENE, J.M., JOHNSON, J.L., Phys. Fluids **18** (1975) 875.

43. GLASSER, A.H., GREENE, J.M., JOHNSON, J.L., Phys. Fluids **19** (1976) 567.

44. CONNOR, J.W., et al., Phys. Fluids **31** (1988) 577.

45. CARRERAS, B.A., et al., Plasma Physics and Controlled Nuclear Fusion Research 1986 (Proc. 11th Int. Conf., Kyoto, 1986), Vol. 2, IAEA, Vienna (1987) 53.

46. SYKES, A., et al., Nucl. Fusion **32** (1992) 694.

47. SYKES, A., et al., Plasma Phys. Control. Fusion **35** (1993) 1051.

48. PARKER, R.R., et al., Nucl. Fusion **25** (1985) 1127.

49. YASHMANOV, P.N., et al., Nucl. Fusion **30** (1990) 1999.

50. REBUT, P.H., LALLIA, P.P., WATKINS, M.L., Plasma Physics and Controlled Nuclear Fusion Research 1988 (Proc. 12th Int. Conf., Nice, 1988), Vol. 2, IAEA, Vienna (1989) 191.

51. LACKNER, K., GOTTARDI, N.A.O., Nucl. Fusion **30** (1990) 767.

52. GRYAZNEVICH, M., et al., Bull Am. Phys. Soc. **38** (1993) 2008.

53. ROACH, C.M., Plasma Phys. Control. Fusion **38** (1996) 2187.

54. RAMOS, J.J., et al., at the Workshop for Establishing the Physics Basis Needed to Access the Potential of Compact Toroidal Reactors, Oak Ridge, TN, July 19, 1994.

55. REWOLDT, G., TANG, W.M., et al., Phys. Plasmas **3** (1996) 1667.

56. WALSH, M., Plasma Physics Seminar, University of Wisconsin-Madison, November 14, 1994.

57. WESSON, J., *Tokamaks*, Clarendon Press, Oxford, 1987.

58. CORDEY, J.G., CHALLIS, C.D., STUBBERFIELD, P.M., Plasma Phys. Control. Fusion **30** (1988) 1625.

59. SHAING, K.C., et al., Phys. Plasmas **2** (1995) 349.

60. ROACH, C.M., CONNOR, J.W., JANJUA, S., Plasma Phys. Control Fusion **37** (1995) 679.

61. REWOLDT, G., TANG, W.M., at the Workshop for Establishing the Physics Basis Needed to Access the Potential of Compact Toroidal Reactors, Oak Ridge, TN, July 19, 1994.

62. COLCHIN, R.J., Phys. Fluids B **5** (1993) 2481.

63. GRYAZNEVICH, M., WALSH, M.J., et al., Bull AM. Phys. Soc. **41** (1996) 1400.

64. TAYLOR, T.S., STRAIT, E.J., et al., Phys. Plasmas **2** (1995) 2390.

65. HWANG, Y.S., et al., Bull Am. Phys. Soc. **41** (1996) 1401.

66. ONO, M, et al., Plasma Physics and Controlled Nuclear Fusion Research 1992 (Proc. 14th Int. Conf., Würzburg, 1992), Vol. 1, IAEA, Vienna (1993) 693.

67. BRESLAU, J., et al., Bull. Am. Phys. Soc. **41** (1996) 1402.

68. NELSON, B.A., et al., Nucl. Fusion **34** (1994) 1111.

69. NELSON, B.A., et al., Phys. Plasmas **2** (1995) 2337.

70. HANADA, K. et al., Trans Fusion Technol. **27** (1995) 440.

71. TOYAMA, H., et al., Bull Am. Phys. Soc. **40** (1995) 1657.

72. LUDWIG, G.O., at the Workshop for Establishing the Physics Basis Needed to Access the Potential of Compact Toroidal Reactors, Oak Ridge, TN, July 19, 1994.

73. SAKHAROV, N., at the Workshop for Establishing the Physics Basis Needed to Access the Potential of Compact Toroidal Reactors, Oak Ridge, TN, July 19, 1994.

74. NELSON, B.A., et al., Bull Am. Phys. Soc. **41** (1996) 1577.

75. MORRIS, A.W., at the Workshop for Establishing the Physics Basis Needed to Access the Potential of Compact Toroidal Reactors, Oak Ridge, TN, July 19, 1994.

76. ONO, M., et al., Bull. Am. Phys. Soc. **41** (1996) 1403.

77. PENG, Y-K. M., et al., Bull. Am. Phys. Soc. **41** (1996) 1403.

78. FONCK, R.J., et al., Bull. Am. Phys. Soc. **41** (1996) 1400.

79. BUTTERY, R., et al., Plasma Physics and Controlled Nuclear Fusion Research 1994 (Proc. 15th Int. Conf., Seville, 1994), Vol. 2, IAEA, Vienna (1995) 633.

80. MILLER, R.L., KRAKOWSKI, R.A., et al., Los Alamos National Laboratory Report LA-10740-MS, June 1986.

81. PENG, Y-K. M., STRICKLER, D.J., et al., Fusion Technol. **8** (1985) 338.

82. PENG, Y-K. M., GALAMBOS, J.D., SHIPE, P.C., Fusion Technol. **21** (1992) 1729.

83. KRAKOWSKI, R.A., at the Workshop for Establishing the Physics Basis Needed to Access the Potential of Compact Toroidal Reactors, Oak Ridge, TN, July 19, 1994.

84. CHOE, W., NSTX Research Forum, Princeton N.J., February 6, 1997.

85. WRIGHT, J.C., *Metallurgy in Nuclear Power Technology*, Prentice-Hall, Englewood Hills, NJ, 1962.

3. Current Penetration in Tokamaks

3.1 Introduction

One of the fundamental issues of tokamak operations concerns the processes that distribute current density inside the plasma. This problem is especially important for the start-up phase, when current is rapidly being introduced into the plasma. Understanding the mechanisms that determine the startup distribution of the plasma current allows better operating techniques, which can result in better plasma performance in terms of ultimate plasma current, stability, energy confinement, and operational efficiency. Plasma current is also redistributed during disruptions and internal reconnection events (IREs). Of course, the same phenomena that distribute current in tokamaks can also move particles and energy around. Examples include the interaction between Joule heating and plasma resistivity, and the wholesale redistribution of plasma energy that occurs during a disruption.

The same mechanisms drive the current penetration in these different stages of tokamak operation; two of these mechanisms are usually important. The first is classical current diffusion, which is the same process that transports current into resistive conductors. The second is tearing modes, which appear in two different flavors. During startup, when a non-monotonic q profile may exist, double tearing modes can play a large role in current transport. At other times, when the q profile is monotonically increasing, single tearing modes can lead to disruptions, sawteeth, and internal reconnection events.

This chapter contains a discussion of the physics relevant to current penetration and redistribution in tokamaks. Section 3.2 discusses current diffusion in tokamaks. Section 3.3 deals with tearing modes. It contains an introduction to tearing modes, and discusses the roles of magnetic islands in disruptions (and IREs) and current penetration during startup. Section 3.4 outlines the formal flux consumption method for characterizing the efficiency of

the ohmic startup of tokamaks.

3.2 Current Diffusion

The first mechanism that allows current to penetrate into a tokamak plasma is current diffusion. This is the same means that allows the penetration of currents and magnetic fields in solid-state conductors. In a metal, where the resistance is assumed to be isotropic and independent of temperature and current density, the diffusion equation for the magnetic field can be written as [1]

$$\frac{\partial \mathbf{B}}{\partial t} = \frac{\eta}{\mu_0}\nabla^2\mathbf{B} \tag{3-1}$$

where η is the resistivity in ohm-meters. This equation can be simply derived from Faraday's Law and Ohm's Law. The current density **J** can be found from

$$\nabla \times \mathbf{B} = \mu_0 \mathbf{J}. \tag{3-2}$$

Often the exact solution of equation 3-1 is not necessary. In these cases, an estimate of scale lengths is generally sufficient. If some scale length L for diffusion is known, for example the thickness of a wire, and the magnetic field is assumed to vary exponentially in space, the characteristic time for diffusion τ can be expressed as

$$\tau = \frac{\mu_0 L^2}{\eta}. \tag{3-3}$$

This result is similar to the one obtained for the skin depthδ ($\approx L$) of a conductor with a sinusoidally-varying electric field [2]:

$$\delta = \sqrt{\frac{2\eta}{\mu_0 \omega}} \tag{3-4}$$

where $\omega (\approx 1/\tau)$ is the angular frequency.

These equations are of limited validity in tokamak plasmas. This is due primarily to the temperature dependence of the plasma resistivity. For classical current diffusion (i.e., no field-line curvature effects) the resistivity is well-represented by the Spitzer relation [1]:

$$\eta \propto \frac{\pi e^2 m_e Z_{eff} \ln\Lambda}{\left(4\pi\varepsilon_0\right)^2 T_e^{3/2}} = 5.2\times 10^{-5} \frac{Z_{eff}\ln\Lambda}{T_e^{3/2}(eV)} \qquad (3\text{-}5)$$

where Z_{eff} is the number of plasma electrons per ion, and

$$\Lambda = 12\pi n_e \lambda_D^3$$

where λ_D is the Debye length. Usually $\ln\Lambda$ is between 10 and 20 for laboratory plasmas, and is often set equal to a value independent of density (for example, 15). Thus the plasma resistivity is mainly a function of the electron temperature. Since the temperature profile in a tokamak can vary quite dramatically during startup or over a disruptive MHD event, this effect is significant. This functional dependence on temperature can be expressed instead as a dependence on space and time. If the diffusion equation (3-1) is re-derived for a tokamak plasma to include spatial and temporal variations of the resistivity, the result is

$$\mu_0 \frac{\partial \mathbf{B}}{\partial t} = \eta(\mathbf{r},t)\nabla^2\mathbf{B} - \left[\nabla\eta(\mathbf{r},t)\right]\times\left[\nabla\times\mathbf{B}\right] \qquad (3\text{-}6)$$

where the functional dependence of the resistivity has been specified.

If a self-consistent solution to this equation is desired, then the equations for the evolution of electron temperature must be included. This coupling is brought about by the local heating of the plasma by the current, and the thermal diffusion of the electron heat. Many different models can of course be implemented. A relatively simple one for cylindrical geometry uses four equations: heat conduction for electrons, for ions, the magnetic diffusion

equation, and Spitzer resistivity. The density profile is held constant. This is as given in [3]:

$$\frac{3}{2}n\frac{\partial T_e}{\partial t} = \frac{1}{r}\frac{\partial}{\partial r}\left(r\kappa_e\frac{\partial T_e}{\partial r}\right) - \frac{3m_e}{m_i}\frac{n}{\tau_e}(T_e - T_i) + \frac{\eta}{\mu_0}\left(\frac{1}{r}\frac{\partial (rB_\theta)}{\partial r}\right)^2$$

$$\frac{3}{2}n\frac{\partial T_i}{\partial t} = \frac{1}{r}\frac{\partial}{\partial r}\left(r\kappa_i\frac{\partial T_i}{\partial r}\right) + \frac{3m_e}{m_i}\frac{n}{\tau_e}(T_e - T_i) \qquad (3\text{-}7)$$

$$\mu_0\frac{\partial B_\theta}{\partial t} = \frac{\partial}{\partial r}\left(\frac{\eta}{r}\frac{\partial (rB_\theta)}{\partial r}\right)$$

where κ_e and κ_i are the electron and ion thermal conductivities, τ_e is the electron collision time, and Spitzer resistivity is implicitly assumed. Sometimes current diffusion in tokamaks is modelled with extensive codes such as the Tokamak Simulation Code (TSC) [4]. The situation can be further complicated by the introduction of effects such as radiation and sputtering, and by the addition of other heating or current drive mechanisms. Yet another complication arises from neoclassical effects brought about by toroidicity.

In practice, the rate of current diffusion can be calculated by measuring time-dependent temperature and density profiles, and taking neoclassical effects into account. The associated diffusion of the magnetic field can be found directly from equilibrium reconstructions, soft X-ray emission surfaces, magnetic probes, or other methods.

3.3 Tearing Modes

The presence of magnetic islands generated by tearing modes can have a strong influence on the current density distribution in a tokamak. This section examines the basic theory behind the growth of tearing modes, and the role of magnetic islands in current penetration during startup and disruptive MHD events.

Tearing Mode Theory

The primary features of tearing modes can be identified by examining a simple model. This model begins with Maxwell's equations and a set of resistive MHD equations. In this model, pressure gradients, temperature gradients, and large-scale flows are neglected, and the plasma is considered to be incompressible. A cylindrical tokamak approximation will be used where appropriate. The resistive MHD equations used are [5]:

$$\begin{aligned} \rho_m \frac{d\mathbf{v}}{dt} &= \mathbf{J}\times\mathbf{B}, \\ \mathbf{E} + \mathbf{v}\times\mathbf{B} &= \eta\mathbf{J}, \end{aligned} \tag{3-8}$$

where ρ_q is the charge density, ρ_m is the mass density, and $\mathbf{v}$ is the flow velocity. From these equations the following simplified set may be derived [6]:

$$\begin{aligned} \frac{\partial \mathbf{B}}{\partial t} &= \nabla\times(\mathbf{v}\times\mathbf{B}) - \frac{1}{\mu_0}\nabla\times\eta(\nabla\times\mathbf{B}), \\ \nabla\times\left(\rho_m\frac{d\mathbf{v}}{dt}\right) &= \frac{1}{\mu_0}\nabla\times[(\nabla\times\mathbf{B})\times\mathbf{B}], \\ \nabla\cdot\mathbf{v} &= 0, \end{aligned} \tag{3-9}$$

where the incompressibility has been explicitly noted. These equations would be quite difficult to solve analytically, except for a convenient fact: for values of the Lundquist number S much greater than 1, the stability is not affected by the resistivity except at narrow singular layers.

The Lundquist number, also known as the magnetic Reynolds number, is the ratio of the magnetic diffusion time to the poloidal Alfvén time and is given as [6]

$$S = \frac{\tau_R}{\tau_A} = \frac{\mu_0 r^2/\eta}{R_0/v_A} \tag{3-10}$$

where v_A is the Alfvén velocity. The Lundquist number typically varies between 100 for small plasma experiments to 10^{10} for future reactors. For illustrative purposes, at the half-

radius of the MEDUSA tokamak $S \approx 1000 - 2000$, while on the TFTR experiment $S \approx 10^7$ at the corresponding location.

In the singular layer, it is found that $\mathbf{k}\cdot\mathbf{B}=0$; this means that the instability only has components perpendicular to the magnetic field. In a tokamak, this is essentially the radial direction. This result implies that the singular layers must lie around rational surfaces where $q=m/n$. This is similar to the ideal kink mode, which requires rational flux surfaces for the instability to "bite its own tail." The tearing mode is often known as the "resistive kink ."

The growth rate of the mode is determined by matching the solutions of the MHD equations inside and outside the singular layer. It is found that there is a discontinuity in the logarithmic derivative of the perturbed magnetic field across the resistive layer [6,7]. (This is also true for the vector potential and the magnetic flux.) This discontinuity is known as Δ', and it is quantified variously for a cylindrical tokamak as [5,6,8,9,10]:

$$\Delta' = \frac{\left[\dfrac{d\tilde{A}_l(r_s)}{dr}\right]_-^+}{\tilde{A}_l(r_s)} = \frac{\left[\dfrac{d\tilde{B}_r(r_s)}{dr}\right]_-^+}{\tilde{B}_r(r_s)} = \frac{\left[\dfrac{d\psi(r_s)}{dr}\right]_-^+}{\psi(r_s)}, \tag{3-11}$$

$$\left[\xi(x)\right]_-^+ \equiv \lim_{\varepsilon \to 0}\left(\xi(x+\varepsilon) - \xi(x-\varepsilon)\right),$$

where $\mathbf{A}$ is the vector potential, ψ is the poloidal flux, r_s is the radius of the resistive layer, and the tildes refer to perturbed quantities. The growth rate is given approximately by [5,10]

$$\left(\gamma\tau_A\right)^5 \sim \left(r_s\Delta'\right)^4 \frac{m^2}{S^3}\left(\frac{r}{q}\frac{dq}{dr}\right)^2 \tag{3-12}$$

where m is the poloidal mode number and γ is the inverse growth rate. The tearing mode is unstable if $\Delta' > 0$; otherwise it is stable. The stability criterion is closely related to the slope

of the $J(r)$ profile and, by extension, the $q(r)$ profile around the resistive layer. Steeper gradients are destabilizing to tearing modes.

The "result" of a destabilized tearing mode is magnetic islands. A magnetic island is a non-axisymmetric region of closed flux within a tokamak volume. Figure 3-1 is an illustration of an $m/n = 2/1$ magnetic island. The island is created when the radial magnetic fields around the rational flux surface become large enough to reconnect and change the magnetic topology. Figure 3-2 is a schematic illustration of the production and early stage of growth of a magnetic island. The island structure typically grows linearly from a size much smaller than the resistive layer to an intermediate size (which is still, however, significantly smaller than the minor radius.) Feedback mechanisms then begin to limit the island growth; this region of nonlinear growth is called the "Rutherford regime" [11]. The main feedback mechanism is the flattening of the q profile about the island structure. This flattening decreases dq/dr, decreasing the growth rate [6]. The final island size is generally significantly larger than the resistive layer, and can be a good fraction of the minor radius.

Magnetic islands have a number of effects on plasma behavior. One of the first effects to be observed in tokamak experiments was poloidal field oscillations at the plasma edge. These fluctuations, called "Mirnov oscillations", are caused by the perturbation of the field by rotating magnetic islands. As mentioned in Chapter 2, magnetic islands can "short-circuit" transport by providing a short path around the island width via the separatrix. Different sets of magnetic islands can interfere to cause other effects. The $m/n = 1/1$ island is believed to be responsible for sawteeth. Double tearing modes can lead to rapid current penetration during startup. Major disruptions and IREs are believed to be caused by interfering chains of magnetic islands. These last effects are discussed later in this section.

The previous discussion treated magnetic islands in an extremely simple model. The effects of toroidicity and finite beta can change the stability criteria for these modes.

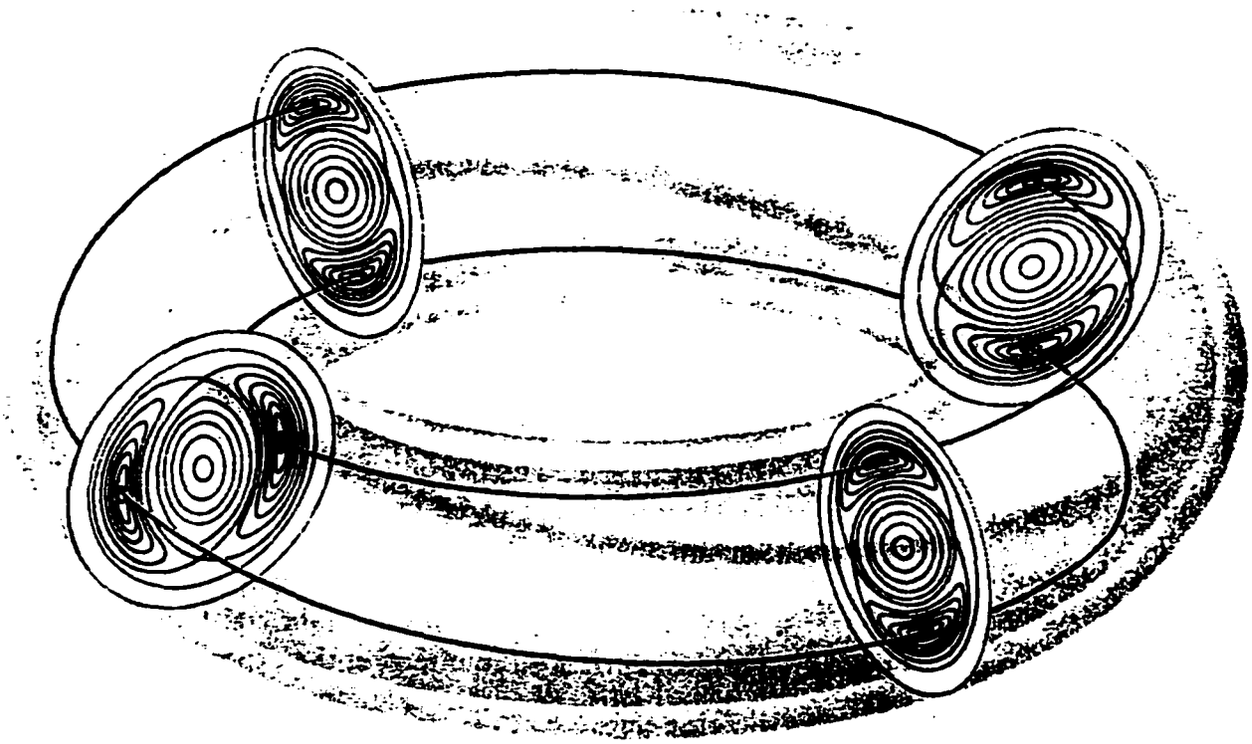

Figure 3-1. Illustration of a 2/1 magnetic island (from Furth [6]).

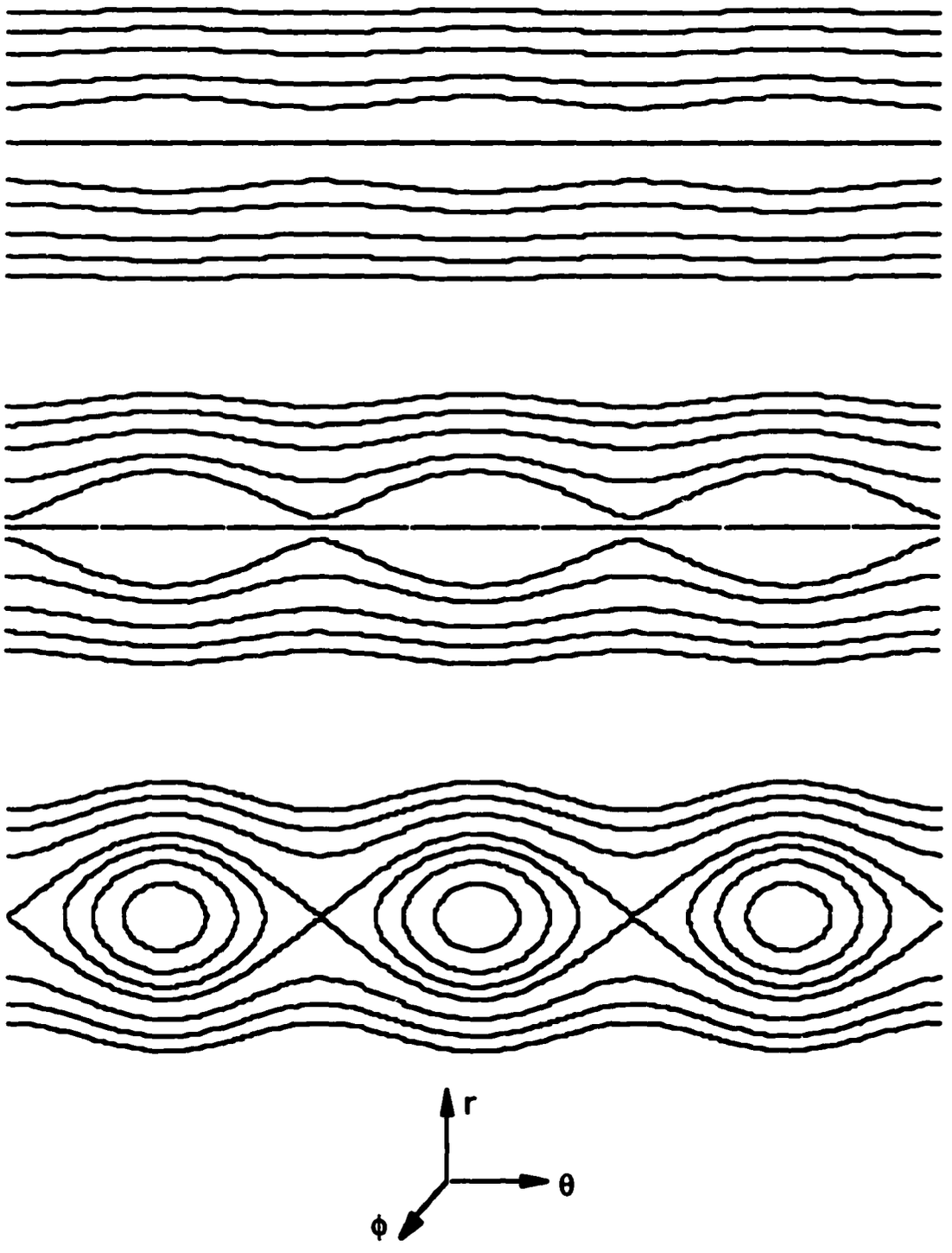

Figure 3-2. Illustration of production and early growth of a large-m magnetic island structure. The arrows show the orientation in toroidal geometry. Top shows perturbed field. Middle shows fields just prior to reconnection. Bottom shows reconnected field lines and resultant islands.

However, the qualitative process of island formation and the effects of these islands are unchanged with these additions.

When toroidicity (but not finite pressure) is included in the tearing mode formulation, some new phenomena are observed. Perhaps primary among these is the destabilization of "satellite" modes by an island structure [10,12]. This is a process whereby a growing island perturbs the current density gradient and destabilizes a nearby mode of different helicity (e.g. a 2/1 island may destabilize a 3/2 or 5/3 mode.) This phenomenon may be important in disruption phenomenology. The addition of toroidicity can also affect the saturated sizes of the evolved magnetic islands. As mentioned in Chapter 2, toroidal calculations show greatly diminished island widths at low aspect ratios [13].

When the effects of finite pressure gradients are added, an additional driving term becomes important and the destabilized modes are then known as "neoclassical tearing modes" [14,15]. This driving term arises from perturbations in the bootstrap current caused by small magnetic islands [16,17]. The bootstrap current is caused by viscous damping of the poloidal electron flow [16]; the details of the distribution of this current depend on the local pressure gradients in the plasma (see Chapter 2.) The presence of islands locally deforms the pressure contours and perturbs the bootstrap current profile. This perturbed current profile can cause small island structures to become unstable to further growth, although it cannot generate magnetic islands from an axisymmetric geometry.

In addition to the neoclassical term, there are other terms contributing to island growth that are not included in the classical tearing mode analysis. Two of these are the so-called "Glasser-Greene-Johnson" term and another term arising from polarization drift effects. The latter effect is not well characterized at this time [18] and will not be discussed here. The former term is a stabilizing term arising from good-average-curvature effects in toroidal plasmas with finite beta [19,20]. It is usually small, but can be significant for

spherical tokamaks.

All of these effects can be combined into an island growth equation like that given in Chapter 2. A slightly different version of equation 2-23 is given here [16-18,21]:

$$\frac{dW}{dt} = 1.2\frac{\eta}{\mu_0}\left[\Delta'(W) + \left(\Delta_{neo} - \Delta_{GGJ}\right)\frac{W}{W^2 + W_d^2} - \frac{\Delta_{pol}}{W^3}\right]. \qquad (3\text{-}13)$$

The terms in equation 3-13 are as follows: η is the resistivity, W is the island width, Δ' is the classical tearing mode figure of merit (equation 3-11), Δ_{neo} is the neoclassical term, W_d is the critical island width for growth of the neoclassical mode, Δ_{GGJ} is the Glasser-Greene-Johnson term, and Δ_{pol} is the polarization drift term. The middle two terms can be further specified as follows:

$$\Delta_{neo} = -9.26\left[\varepsilon\rho_s\right]^{0.5}\frac{\beta_0 q_s^2 L_q}{\varepsilon^2\rho_s^3 L_p} \approx -\varepsilon^{0.5}\frac{L_q}{L_p} \quad [16,21]$$

$$W_d \approx 5.1\left(\frac{\chi_\perp}{\chi_\parallel}\right)^{0.25}\left[\varepsilon\rho_s^2 L_q n\right]^{-0.5} \quad [21] \qquad (3\text{-}14)$$

$$\Delta_{GGJ} = -5.4\frac{\beta_p\varepsilon^2(1-q^2)}{\rho(q')^2 L_p} \approx 6.0\frac{\beta_t L_q^2(q^2-1)}{rL_p} \quad [17,21]$$

where $\rho = r/a$ is the normalized minor radius, L is a scale length given as $L_\xi = \xi/\xi'$, χ is the pressure diffusivity, n is the toroidal mode number, and the subscript "s" refers to the resistive layer.

Neoclassical effects tend to destabilize tearing modes in most tokamak configurations. In practice these modes tend to develop quite frequently [18], and must be

dealt with (and minimized if possible.)

Double Tearing Modes

A phenomenon that is often observed in tokamak experiments is a series of "minor disruptions" during the current ramp phase. These events are characterized by periodic positive loop voltage spikes, and a temporary slowing of the current ramp. The external poloidal field measurements show that these perturbations have successively lower mode numbers. This behavior has been reported on a number of experiments including LT-3 [22], Alcator A [23], PDX [24], TEXT [25], JET [26,27], T-7 [28], and HT-6M [29].

It has become evident that this phenomenon is caused by double tearing modes. A double tearing mode [8,30,31] results from the interaction of a pair of magnetic islands with the same value of m/n centered at two different resistive layers. This can obviously only occur when the safety factor profile is double-valued. The usual phase in normal tokamak operation where this condition is reached is during the initial current ramp, where the skin effect limits current diffusion in from the edge. If the current is ramped at a fast enough rate, the condition for a double-valued q profile can be met. If the plasma is also unstable to tearing modes at the appropriate flux surfaces (which is often the case), then a pair of islands can form and initiate the double tearing mode.

Figure 3-3 gives a schematic illustration of the double tearing mode after the manner of Stix [30]. The top part of the illustration shows two islands with the same helicity; these islands have a 180° shift in spatial phase due to the opposite signs of the magnetic shear [30]. A clear magnetic separatrix divides the islands. As the islands grow in the Rutherford regime, they approach the geometry shown in the middle part of this drawing, where the separatrix approaches a reconnection. Finally, the reconnection occurs, and the new magnetic topology of the bottom part of the figure is realized. As the plasma current

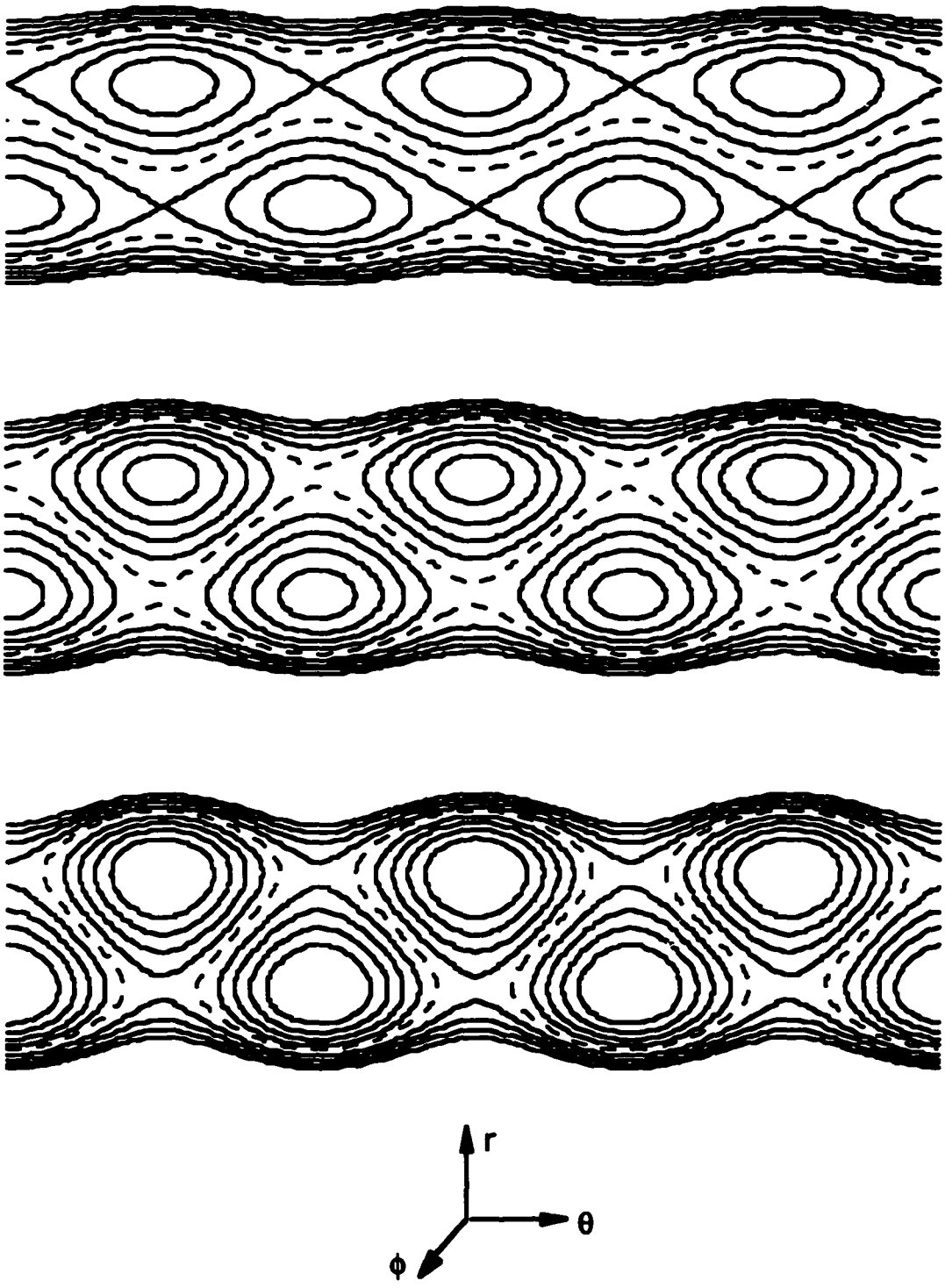

Figure 3-3. Illustration of the growth of a large-m double-tearing mode. The arrows show the orientation in toroidal geometry. The dashed line represents the $q=m/n$ surface. Top shows the islands growing together with a clear separatrix. Middle shows fields just prior to double-tearing reconnection. Bottom shows topology after reconnection. (After Stix [30].)

continues to increase, other island structures may be destabilized, starting the process over again.

The double tearing mode allows the current that has built up on the outside of the island structure to be rapidly transported inward along the newly reconnected field line; this results in a more peaked current profile, leading to a higher internal inductance. The negative loop voltage spike and decreased current ramp rate may be understood in this context. An increase in the inductance naturally leads to an increased inductive voltage, and a reduced value of dI/dt.

In general, double tearing modes degrade the plasma. The reconnection requires significantly more magnetic energy than do the saturated but un-reconnected islands [32]. This energy must be taken from the total magnetic energy of the plasma. Double tearing modes can be avoided in some cases by lowering the current ramp rate, thereby avoiding a double-valued q-profile.

Tearing Modes, Disruptions, and Internal Reconnection Events

In addition to the "soft disruptions" brought about by the double tearing mode, magnetic islands are believed to be responsible for other kinds of abrupt disruptive events. Three of these types of events will be briefly discussed here: sawteeth, hard disruptions, and internal reconnection events.

Sawteeth result from the instability of the m/n=1/1 tearing mode [33,34]. This phenomenon can only occur, for obvious reasons, when a q=1 surface exists inside the plasma. In effect, the sawtooth instability creates a new magnetic axis that "crowds out" the original one. An illustration of the sawtooth instability is shown in Figure 3-4. The typical behavior of sawteeth (called the "Kadomtsev picture" [5]) is as follows. The ohmic heating at the core of a tokamak reduces the resistivity and increases the plasma current. This

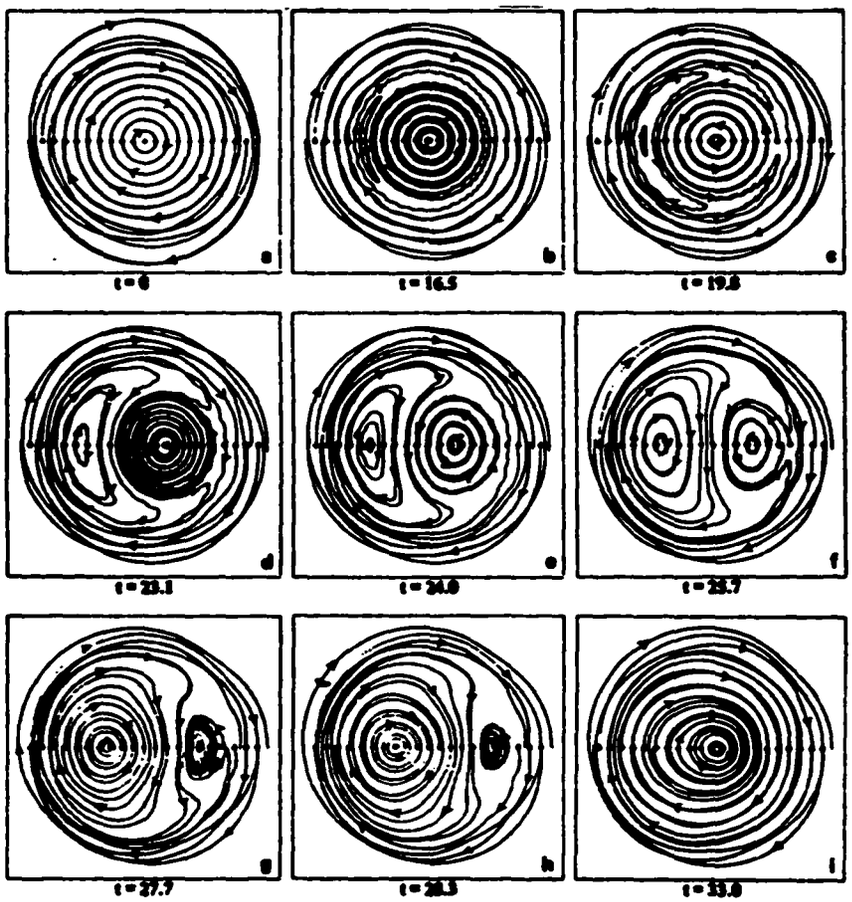

Figure 3-4. Illustration of sawtooth instability (from Sykes & Wesson [34]). Time increases from frame "a" to frame "i".

reduces q_0 to less than 1, destabilizing the tearing mode and allowing the 1/1 island to grow. This island (which has q=1 [6]) continues to grow, crowding out the original magnetic axis. Finally, this original axis collapses, leading to the appropriately-named "sawtooth crash." This process then repeats itself, the entire cycle taking significantly less time than the resistive time scale [6,33]. During most of the growth of the island, the central electron temperature increases almost linearly with time. However, when the crash occurs, the temperature profile in the core is flattened as the plasma pressure is rapidly redistributed. The temporal shape of the electron temperature leads to the term "sawteeth" to describe this phenomenon. The main effect of sawteeth is to enhance transport out of the tokamak core. The region outside the q=1 surface is essentially unaffected. This enhanced transport is certainly not desirable, but it is not usually catastrophic.

The same cannot be said for the "hard disruption," the most fearsome of the three events in this section. A hard disruption abruptly terminates the tokamak discharge, which creates large electromechanical stresses on the vacuum vessel and support structures and sputters large amounts of impurities into the vacuum. Almost all tokamaks occasionally see large, current-terminating disruptions [27]. Although disruptions are not completely understood, one well-known contributing factor is the overlap of magnetic islands with "incommensurate helicities" [5,35,36]. This overlap can be understood in the context of satellite island growth. The growth and overlap of the 2/1 and 3/2 island structures is particularly important, as these have been identified as primary actors in many disruptions. Once the 2/1 and 3/2 islands begin to overlap, their field lines interfere and become stochastic. This leads to a rapid broadening of the current profile, which causes a negative perturbation to the loop voltage and a positive spike in the plasma current [35]. Usually the rapid transport of pressure and current are enough to completely destabilize the current channel, and a major disruption results.

Recently, several spherical tokamak experiments have begun to challenge the inevitability of disruptions. These results, most notably from START [37,38,39] but also from MEDUSA [40] and CDX-U [41], indicate a resilience to hard disruptions unlike conventional tokamaks. These devices instead experience a disruption-like phenomenon known as an "internal reconnection event," or IRE. An internal reconnection event is characterized by an abrupt increase in the plasma current followed by a slower decay back to the original current, a sharply negative spike on the loop voltage, and an increase in impurity radiation. The soft X-ray emission grows before an IRE. During an IRE, the plasma is seen to elongate, and the magnetic axis moves inward. Recent results from START show a marked drop in ℓ_i and β_p after an IRE [42].

These characteristics are quite similar to those discussed for a hard disruption, except that an IRE does not result in a termination of the plasma. In fact, plasmas that experience IREs often seem to recover completely afterwards. Chapter 6 of this thesis contains a detailed analysis of measurements made on IREs in the MEDUSA tokamak which give further evidence of the kinship between IREs and disruptions.

3.4 Flux Consumption Formalism

There is a limited amount of ohmic magnetic flux (volt-seconds) available to create and drive any tokamak plasma. This limit is especially severe in spherical tokamaks, since the flux from a cylindrical tokamak solenoid is roughly proportional to $(A-1)^2$. Understanding the use of startup flux by the tokamak is important if these limited volt-seconds are to be used to best effect.

A thorough understanding of the mechanisms that govern the startup in a given tokamak discharge is nearly impossible, however. Current density can penetrate by diffusion or by double tearing modes. Both of these phenomena are affected by a nearly

innumerable set of factors, including impurity levels, radiation, temperature and density profiles and fluctuations, non-equilibrium magnetic conditions, and edge conditions. Many of these factors are unreproducible, and the effects of some are not easily quantified.

To combat this difficulty, a method of "flux consumption analysis" is employed which uses real measurements to come up with an overall figure of merit for the efficiency of the startup scenario. This method can then be used to compare different startup scenarios in order to determine which uses the flux most efficiently.

This analysis centers on a flux balance equation, which asserts that all of the poloidal flux that links the torus must appear in a plasma term. It is given as [43-45]:

$$\Phi_{in} = \Phi_{tot} = \Phi_{ext} + \Phi_{int}^{ind} + \Phi_{int}^{dis} \qquad (3\text{-}15)$$

where the *in* subscript refers to flux from external coils, *tot* refers to the total internal flux, *ext* refers to poloidal flux generated by the plasma but external to its boundary, *int* refers to plasma flux internal to the boundary, *ind* refers to flux used in magnetic fields, and *dis* refers to flux used by dissipative processes such as resistive losses, radiation, and ionization. Equation 3-15 is essentially a restatement of Faraday's Law. There are two primary means for assigning values to the right-hand side of this equation [46]. The first technique, the "axial method" [47], measures the plasma flux as the difference between the axial flux, ψ_0, and the edge flux, ψ_a. The other technique, the "Poynting method" [45], uses energy conservation to define the flux terms. This second method is widely used in practice since it involves experimentally measurable quantities. The Poynting technique will be used in this thesis, following the general convention.

This technique is derived from Poynting's theorem of energy conservation, as its name suggests. Much of the derivation presented here is taken from Lloyd *et al.* [44]. The electromagnetic energy balance over a toroidal plasma with volume V is given by [2]:

$$-\int_V (\mathbf{J}\cdot\mathbf{E})\,dV = \int_V \left\{\frac{1}{2}\frac{\partial}{\partial t}(\mathbf{E}\cdot\mathbf{D} + \mathbf{B}\cdot\mathbf{H}) + \nabla\cdot(\mathbf{E}\times\mathbf{H})\right\}dV, \tag{3-16}$$

where **J** is the current density, **E** is the electric field, **D** is the electric displacement, **B** is the magnetic induction (commonly known as the magnetic field), and **H** is the magnetic field. Assuming vacuum values of the permeability and permittivity and applying the divergence theorem gives:

$$-\frac{1}{\mu_0}\int_S (\mathbf{E}\times\mathbf{B})\cdot\hat{\mathbf{n}}\,dS = \int_V \left\{\frac{\partial}{\partial t}\left(\frac{\varepsilon_0 E^2}{2} + \frac{B^2}{2\mu_0}\right) + \mathbf{J}\cdot\mathbf{E}\right\}dV, \tag{3-17}$$

where S is the plasma surface and $\hat{\mathbf{n}}$ is the unit vector normal to S. In the above equation, the toroidal component of **B** does not enter since it is constant in time and parallel to the applied electric field. The left-hand side of equation 3-17 is identified as the power input to the plasma, which is simply the product of the plasma current and the surface loop voltage, $I_p V_s$. Further terms may be identified on the right-hand side by defining the internal inductance L_i and resistance R by:

$$L_i \equiv \frac{1}{I_p^2}\int_V \frac{B_p^2}{\mu_0}\,dV,$$

$$R \equiv \frac{1}{I_p^2}\int_V (\mathbf{J}\cdot\mathbf{E})\,dV. \tag{3-18}$$

The electric field energy density term ($\varepsilon_0 E^2$) is not as easily identified. Fortunately for this analysis, it is small compared to the magnetic energy term, and can be dropped from the derivation.

Re-writing equation 3-17 with these new definitions and simplifying gives:

$$V_S = L_i \frac{dI_p}{dt} + \frac{1}{2}\frac{dL_i}{dt} I_p + I_p R. \tag{3-19}$$

The first two terms on the RHS are identified as the internal inductive flux, while the third term is of course the resistive term. The plasma surface voltage is often not a measured quantity. If there is some flux between the measuring loop and the plasma surface, equation 3-19 may be modified to take this "annular flux" into account:

$$V_{loop} = V_S + L_a \frac{dI_p}{dt} + \frac{1}{2}\frac{dL_a}{dt} I_p \tag{3-20}$$

where V_{loop} is the measured loop voltage and L_a is the inductance of the annular flux. This treatment can be extended to include the entire amount of open plasma flux. In this case, the annular inductance is replaced by the external inductance L_{ext}.

Equation 3-20 may be related back to equation 3-15, the initial relation for poloidal flux conservation. This is done by integrating equation 3-20 with respect to time. This gives

$$\Phi_{tot} = \Phi_{ext} + \Phi_{int}^{ind} + \Phi_{int}^{dis} \tag{3-21}$$

where

$$\begin{aligned}
\Phi_{ext} &= \tfrac{1}{2} L_{ext} I_p + \tfrac{1}{2} \int_0^t dt' L_{ext}(t') \frac{dI_p}{dt'}(t'), \\
\Phi_{int}^{ind} &= \tfrac{1}{2} L_i I_p + \tfrac{1}{2} \int_0^t dt' L_i(t') \frac{dI_p}{dt'}(t'), \\
\Phi_{int}^{dis} &= \int_0^t dt' I_p(t') R(t') + \text{other dissipation},
\end{aligned} \tag{3-22}$$

and the total flux is the flux input from external coils. In principle, all of these terms except the dissipative flux can be evaluated. Usually the dissipative term is the quantity for which

equation 3-21 is solved.

All of the terms on the right-hand-side of the first part of equation 3-21 are magnetic fluxes, and as such can be assigned appropriate "inductances". The internal inductance was defined previously in equation 3-18. It can also be re-cast in terms of the normalized internal inductance ℓ_i:

$$L_i = \frac{\mu_0 V \ell_i}{C^2}, \tag{3-23}$$

where V is the plasma volume and C is the circumference of the plasma cross-section. The external inductance is not as easily evaluated. A calculated approximation of the external inductance for elongated, finite-aspect-ratio plasmas was given by Hirshman and Neilson [48]. It is as follows [43,48]:

$$L_{ext} = L_s - \mu_0 R_0 \frac{(M-1)}{4}\left[\ln\left(\frac{8}{\varepsilon}\right) + \beta_p + \frac{\ell_i}{2} - \frac{3}{2}\right] \tag{3-24}$$

where ε is the inverse aspect ratio,

$$L_s = \mu_0 R_0 \frac{f_1(\varepsilon)(1-\varepsilon)}{1-\varepsilon+\kappa f_2(\varepsilon)}, \tag{3-25}$$

$$M = \frac{(1-\varepsilon)^2}{(1-\varepsilon)^2 f_3(\varepsilon)+\sqrt{\kappa}\, f_4(\varepsilon)}, \tag{3-26}$$

and

$$\begin{aligned} f_1(\varepsilon) &= \left(1+1.81\sqrt{\varepsilon}+2.05\varepsilon\right)\ln\left[8/\varepsilon\right] - \left(2+9.25\sqrt{\varepsilon}-1.21\varepsilon\right) \\ f_2(\varepsilon) &= 0.73\sqrt{\varepsilon}\left(1+2\varepsilon^4-6\varepsilon^6+3.7\varepsilon^6\right) \\ f_3(\varepsilon) &= 1+0.98\varepsilon^2+0.49\varepsilon^4+1.47\varepsilon^6 \\ f_4(\varepsilon) &= 0.25\varepsilon\left(1+0.84\varepsilon-1.44\varepsilon^2\right). \end{aligned} \tag{3-27}$$

As mentioned above, the resistive term in equations 3-21 and 3-22 is not easy to evaluate. There are several dissipative processes at work; energy is lost through resistive heating, breakdown, current channel formation, vacuum vessel currents, MHD activity, radiation, and transport. Luckily, there is no need to evaluate all of these terms in practice, since all of the other terms in equation 3-21 can be readily found for a properly diagnosed plasma. In order to complete the flux consumption analysis, a "resistive inductance" L_R is assigned to the resistive term. This "inductance" is given as

$$\Phi_{int}^{dis} = L_R I_p = C_E \mu_0 R_0 I_p \tag{3-28}$$

where C_E is a dimensionless quantity known as the "Ejima coefficient." Substituting equation 3-28 into equation 3-21, one can obtain a direct expression for C_E:

$$C_E = \frac{1}{\mu_0 R_0 I_p}\left(\Phi_{in} - \Phi_{ext} - \Phi_{int}^{ind}\right), \tag{3-29}$$

where the inductive fluxes are as given in equation 3-22:

$$\begin{aligned} \Phi_{ext} &= \tfrac{1}{2} L_{ext} I_p + \tfrac{1}{2} \int_0^t dt' L_{ext}(t') \frac{dI_p}{dt'}(t'), \\ \Phi_{int}^{ind} &= \tfrac{1}{2} L_i I_p + \tfrac{1}{2} \int_0^t dt' L_i(t') \frac{dI_p}{dt'}(t'). \end{aligned} \tag{3-30}$$

The Ejima coefficient is the figure of merit for the flux consumption analysis of a given tokamak startup scenario. It can be determined at any time in the discharge, but is usually only meaningful during a specified startup interval. Once the plasma has become steady-state, all of the input flux becomes dissipative, and C_E increases accordingly. The quoted value of the Ejima coefficient for a given shot is typically given at a specified point in the discharge. One such reference point is the time when the internal inductance reaches a

specified value at a specified plasma current [46]. This method is particularly useful for large tokamaks with significant steady-state discharges. For this thesis, the Ejima coefficient will be quoted at the point when the plasma current reaches its maximum value. Typical values of C_E range from 0.4 (minimum on large tokamaks) to 1 or 2 for less efficient startup techniques and smaller tokamaks.

3.5 References

1. CHEN, F.F., *Introduction to Plasma Physics and Controlled Fusion, Vol. 1: Plasma Physics*, Plenum Press, New York, 1984.

2. JACKSON, J.D., *Classical Electrodynamics*, John Wiley and Sons, New York, 1975.

3. DÜCHS, D.F., FURTH, H.P., RUTHERFORD, P.H., Nucl. Fusion **12** (1972) 341.

4. JARDIN, S.C., et al., J. Comput. Phys. **66** (1986) 481.

5. CALLEN, J.D., "Models of Plasma Confinement and Heating in Tokamaks", U. of Wisconsin Center for plasma Theory and Computation Report UWPR 89-2, 1989.

6. FURTH, H.P., Phys. Fluids **28** (1985) 1595.

7. COPPI, B., GREENE, J.M., JOHNSON, J.L., Nucl. Fusion **6** (1966) 101.

8. FURTH, H.P., RUTHERFORD, P.H., SELBERG, H., Phys. Fluids **16** (1973) 1054.

9. HENDER, T.C., HASTIE, R.J., ROBINSON, D.C., Nucl. Fusion **27** (1987) 1389.

10. CONNOR, J.W., et al., Phys. Fluids **31** (1988) 577.

11. RUTHERFORD, P.H., Phys. Fluids **16** (1973) 1903.

12. GLASSER, A.H., FURTH, H.P., RUTHERFORD, P.H., Phys. Rev. Lett. **38** (1977) 234.

13. CARRERAS, B.A., et al., Plasma Physics and Controlled Nuclear Fusion Research 1986 (Proc. 11th Int. Conf., Kyoto, 1986), Vol. 2, IAEA, Vienna (1987) 53.

14. CARRERA, R., HAZELTINE, R.D., KOTSCHENREUTHER, M., Phys. Fluids **29** (1986) 899.

15. QU, W.X., CALLEN, J.D., U.W. Plasma Report 85-5 (1985).

16. GIANAKON, T.A., HEGNA, C.C., CALLEN, J.D., Phys. Plasmas **3** (1996) 4637.

17. GOLELENKOV, N.N., et al., Phys. Plasmas **3** (1996) 3379.

18. CHANG, Z., CALLEN, J.D., FREDRICKSON, E.D., et al., Phys. Rev. Lett. **74** (1995) 4663.

19. GLASSER, A.H., GREENE, J.M., JOHNSON, J.L., Phys. Fluids **18** (1975) 875.

20. GLASSER, A.H., GREENE, J.M., JOHNSON, J.L., Phys. Fluids **19** (1976) 567.

21. KRUGER, S.E., HEGNA, C.C., CALLEN, J.D., "Geometrical Influences on Neoclassical Magnetohydrodynamic Tearing Modes," Report UW-CPTC 97-10, July 1997.

22. HUTCHINSON, I.H., MORTON, A.H., Nucl. Fusion **16** (1976) 447.

23. GRANETZ, R.S., HUTCHINSON, I.H., OVERSKEI, D.O., Nucl. Fusion **19** (1979) 1587.

24. MEYERHOFER, D.D., GOLDSTON, R.J., KAITA, R., et al., Nucl. Fusion **25** (1985) 321.

25. PORTER, J.L., et al., Nucl. Fusion **27** (1987) 205.

26. CAMPBELL, D.J., LAZZARO, E., NAVE, M.F.F., et al., Nucl. Fusion **28** (1988) 981.

27. WESSON, J.A., et al., Nucl. Fusion **29** (1989) 641.

28. VASIN, N.L., VOLKOV, V.V., et al., Sov. J. Plasma Phys. **14** (1988) 517.

29. GAO, X., Trans. Fusion Technol. **27** (1995) 477.

30. STIX, T.H., Phys. Rev. Lett. **36** (1976) 521.

31. MAHAJAN, S.M., HAZELTINE, R.D., Nucl. Fusion **22** (1982) 1191.

32. CARRERAS, B., HICKS, H.R., WADDELL, B.V., Nucl. Fusion **19** (1979) 583.

33. WADDELL, B.V., et al., Nucl. Fusion **16** (1976) 528.

34. SYKES, A., WESSON, J.A., Phys. Rev. Lett. **37** (1976) 140.

35. CARRERAS, B., et al., Phys. Fluids **23** (1980) 1811.

36. DIAMOND, P.H., et al., Phys. Fluids **27** (1984) 1449.

37. SYKES, A., et al., Plasma Phys. Control. Fusion **35** (1993) 1051.

38. COLCHIN, R.J., Phys. Fluids B **5** (1993) 2481.

39. WALSH, M., Plasma Physics Seminar, University of Wisconsin-Madison, November 14, 1994.

40. GARSTKA, G.D., et al., Bull. Am. Phys. Soc. **41** (1996) 1401.

41. BRESLAU, J., ET AL., Bull. Am. Phys. Soc. **41** (1996) 1402.

42. BUTTERY, R.J., et al., in the Proceedings of the International Workshop on Spherical Torus and US-Japan Workshop for Low Aspect Ratio Tokamaks, Vol. II, Abingdon, Oxfordshire U.K., December 4-6, 1996, 676, 672.

43. JONES, T.G., Ph.D. Thesis, Princeton University, November 1995.

44. LLOYD, B., JACKSON, G.L., TAYLOR, T.S., et al., Nucl. Fusion **31** (1991) 2031.

45. EJIMA, S., et al., Nucl. Fusion **22** (1982) 1313.

46. JARDIN, S.C., KESSEL, C.E., POMPHREY, N., Nucl. Fusion **34** (1994) 1145.

47. HAWRYLUK, R.J., BOL, K., JOHNSON, D., Princeton Plasma Physics Laboratory Report PPPL-1508, 1979.

48. HIRSHMAN, S.P., NEILSON, G.H., Phys. Fluids **29** (1986) 790.

4. The MEDUSA Tokamak

4.1 Introduction

The experiments described in this work were conducted on the Madison EDUcational Small-Aspect-ratio (MEDUSA) tokamak. MEDUSA is a small-scale spherical tokamak designed and built to allow the observation of ohmically produced spherical tokamak plasmas on a laboratory scale. It has also served as a test-bed for and lead-in to the Pegasus ultra-low-aspect-ratio toroidal experiment currently under construction.

The accessible size and relative flexibility of MEDUSA, coupled with its set of magnetic diagnostics (discussed later), make it an excellent tool for the analysis of MHD phenomena in STs. The insulating vacuum vessel produces no eddy currents to complicate the analysis. The power supplies and coils may be modified to change the operational scenario. The relatively short pulse length and cold (by fusion standards) temperatures allow plasma diagnosis by electrostatic and magnetic probes.

MEDUSA was first conceived as an undergraduate student project in early 1992. The original design of the "Minimac" was a conventional tokamak with $R = 25$ cm, $a = 7$ cm, $B_T \leq 0.5$ T, and $I_p \leq 15$ kA. Construction began in the summer of 1992. Later that year, early results from the START experiment [1,2] hinted at interesting research possibilities for spherical tokamaks. This provided an impetus to convert the nascent Minimac into MEDUSA, which was done before much construction had been completed. The construction of MEDUSA was completed in the spring of 1994, and the first plasma was achieved in October of that year.

This chapter will describe the MEDUSA tokamak and the associated experimental facility. It includes information on the machine structure, vacuum and power systems, control, data acquisition, and diagnostics. Table 4-1 contains a summary of MEDUSA

Parameter	Typical Value
Major Radius	0.09 m - 0.14 m
Minor Radius	0.04 m - 0.10 m
Aspect Ratio	1.5 (1.35 min)
Plasma Current	20 kA (40 kA max)
Toroidal Field	0.3 T (0.5 T max)
Pulse Length	1 ms (3 ms max)
OH Flux Swing	10 mV-s (single swing)
Available Capacitive Energy:	
Toroidal Field	41 kJ
Ohmic Heating	116 kJ
Vertical Field	17 kJ

Table 4-1. Design and Operating Parameters for the MEDUSA tokamak.

design and operating parameters. Figure 4-1 is a photograph of MEDUSA, and Figure 4-2 is a cross-sectional drawing of the experiment.

4.2 Vacuum Vessel and Pumping System

The MEDUSA vacuum vessel is constructed entirely out of insulating materials, primarily glass. See Figure 4-2. The vessel cross-section is rectangular. The top and bottom

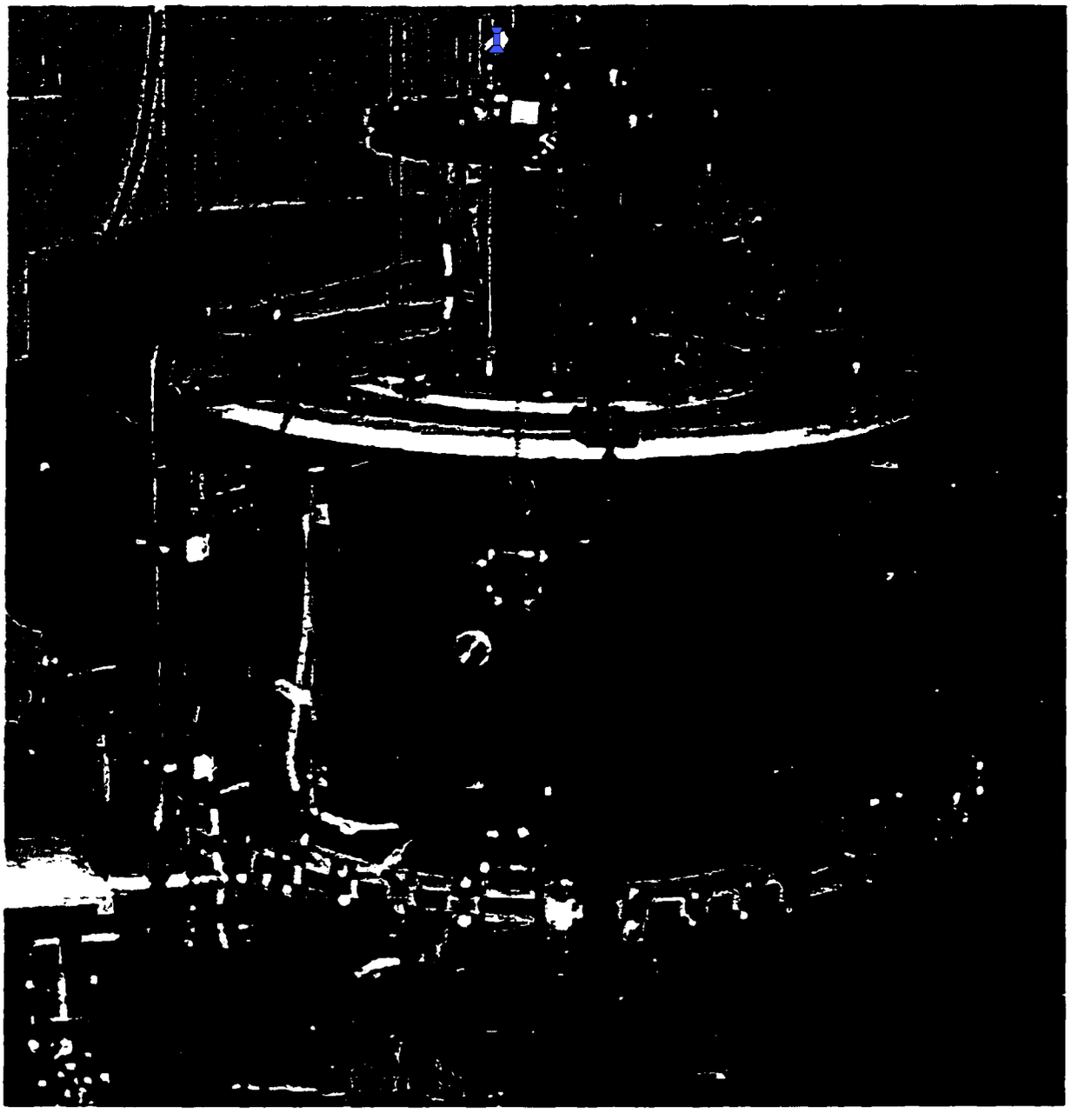

Figure 4-1. Photograph of the MEDUSA tokamak.

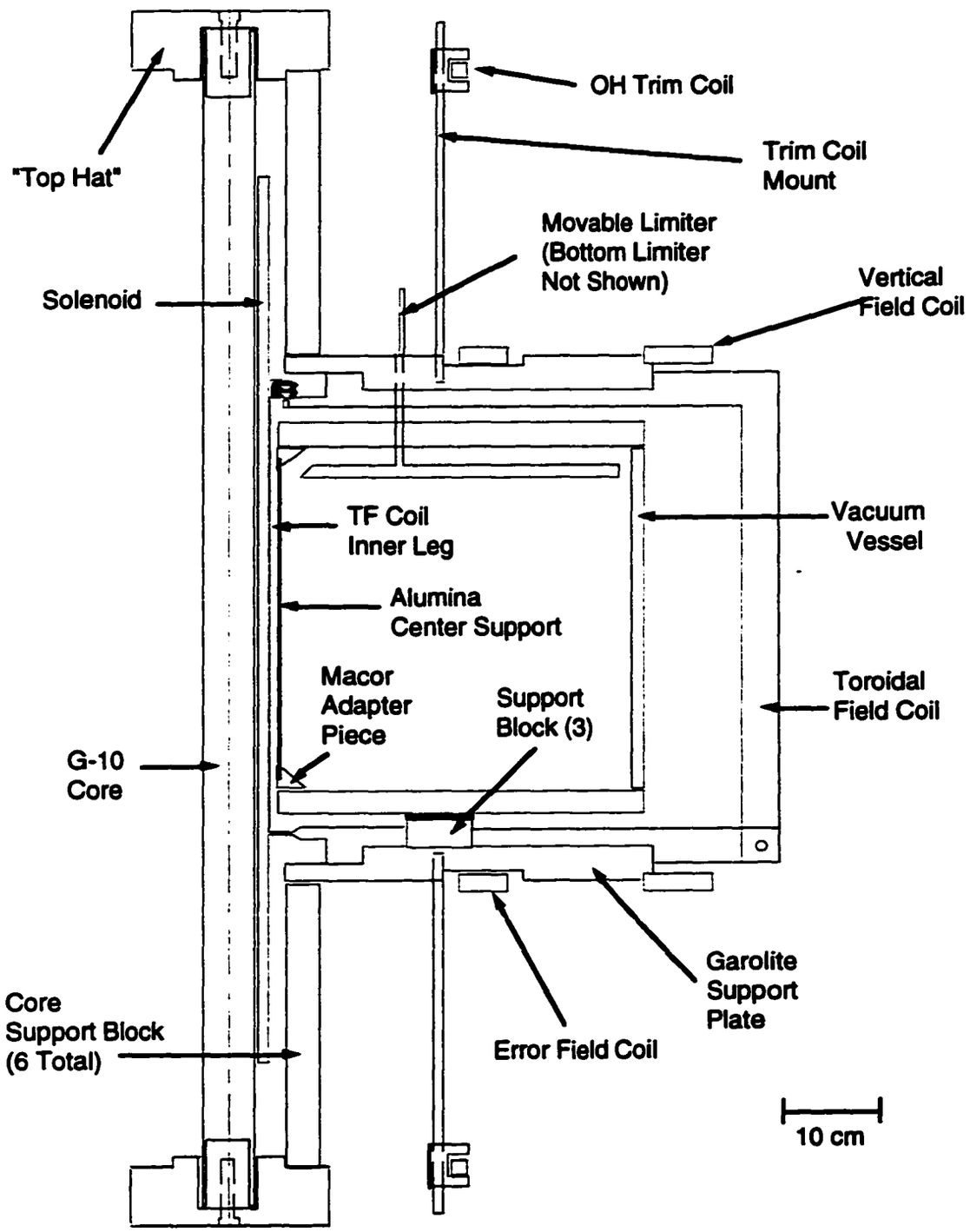

Figure 4-2. Cross-sectional drawing of the MEDUSA tokamak.

walls are cylindrical plates, 30.5 cm in radius, of 2 cm thick glass. This thickness is required to handle the large shearing load applied to these surfaces by 3 tonnes of atmospheric pressure. The outer wall is a thin-wall borosilicate glass cylinder originally used on the High-Beta Tokamak (HBT) experiment. This cylinder is 30 cm tall, with an outer radius of 30.5 cm and a wall thickness of 0.6 cm. The inner wall is a 24 cm tall cylinder of alumina ceramic (Al_2O_3), with a 3.6 cm radius and 0.3 cm wall thickness. The inner cylinder is mated to the top and bottom plates by macor transition pieces that are epoxied to the alumina. The transition pieces on the inside, and the glass cylinder on the outside, butt against the top and bottom plates through viton pads, which are the major vacuum seals for the vessel.

Glass was chosen for the outer surfaces of the vacuum vessel for several reasons. First, glass is relatively inexpensive to produce and machine. Since MEDUSA was built with essentially no budget, this was a tremendous cost saving over metal. Second, glass allows direct optical diagnosis of the plasma, which makes visible light and camera measurements quite simple. Third, glass is an insulator, so it cannot carry induced and/or eddy currents that would distort the plasma equilibrium measurements and perturb the startup. The inner wall was manufactured from alumina since the inner wall need not be transparent, and alumina is significantly stronger than glass in compression and tension (the modulus of rupture of alumina is 210-340 MPa, while that of glass is 69-107 MPa [3]).

The limiting surfaces of the vacuum vessel are all stainless steel. The inner surface, which is almost always the only limiter the plasma contacts, is a thin (50 micron) sheet of stainless steel wrapped around the alumina cylinder. This wall was installed early in the program after it was determined that sputtered impurities from the alumina cylinder were seriously degrading the performance of the plasma. The plasma is limited top and bottom at one toroidal location by movable stainless rail limiters. The limiter assemblies consist of two

cylindrical rods of stainless steel; the end of a 0.6 cm rod is welded into a 1.2 cm rod. The thinner rod passes through a vacuum port and allows the thicker rod, which limits the plasma, to move up and down. In practice, these limiters are almost always used in the fully retracted position. The outer wall is not covered with any stainless steel; this is a deliberate omission, since the plasma rarely, if ever, contacts this wall.

Access to the plasma is provided by seven 5.1 cm diameter holes cut in the top and bottom plates. The holes are located at two major radii, 12 and 25 centimeters. These ports are sealed by circular aluminum flanges that are 10 cm in diameter. Viton O-rings are used for the vacuum seal. These flanges are held in place by atmospheric pressure (approximately 200 N per flange.) The positions of the ports are illustrated in Figure 4-3. Two of the ports connect directly to the vacuum pumping stack and are not used with flanges. The rail limiters take up one port each, one on the top and one on the bottom. A titanium gettering assembly (discussed later in this section) uses a port on the bottom plate. Another port is used for a combined assembly for gas puffing and preionization filaments (also discussed later). The final port is used for diagnostics, and has housed magnetic and electrostatic probes. Additional port access is provided by two small ports (1 cm diameter) on the outer wall at the plasma midplane. These ports have been used to house probes (the most notable of which was an "IRE making" probe, a steel rod inserted deep into the plasma specifically to spew impurities) and a quartz window to provide access to plasma O VI (381 and 383 nm) radiation. These ports are also sealed with viton O-rings and held in place by atmospheric pressure.

The working gas for plasma discharges is usually hydrogen or deuterium. Approximately once each run day, this gas is transported from the cylinder into a storage tank at an intermediate pressure, typically 1 torr. This tank is then valved off from the cylinder. The gas for a shot is introduced into the vacuum chamber by a computer-controlled

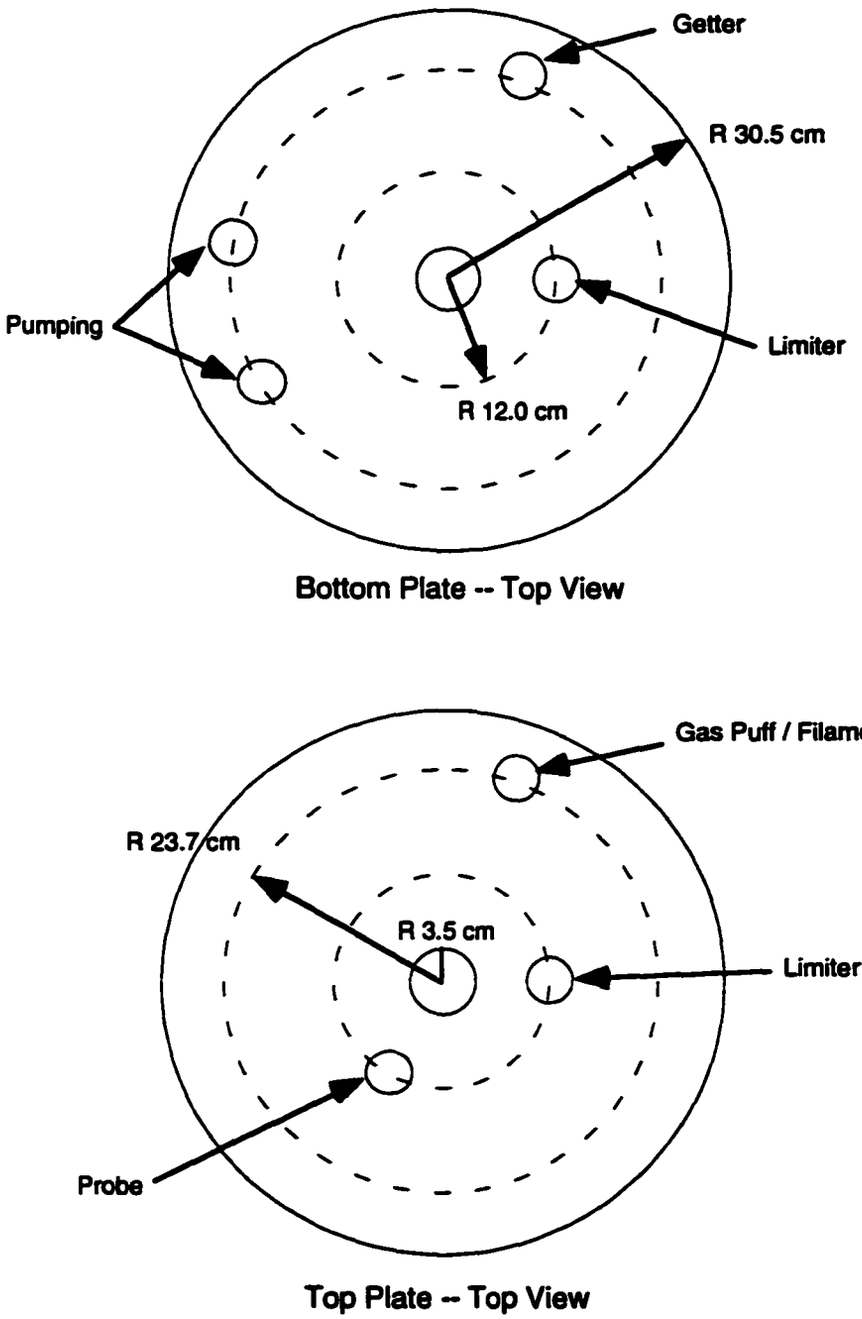

Figure 4-3. Locations of MEDUSA ports. All ports shown have 5.1 cm diameter. Ports are labelled by current use.

solenoid valve. A needle valve in series with this control valve is used to adjust the flow rate, and hence the pressure, of the working gas. Gas is puffed 1.9 seconds before the discharge is initiated in order for the pressure to equilibrate. This method has proven to be an extremely stable and repeatable method of gas puffing.

Titanium gettering is used to control low-Z impurities. A tungsten filament wrapped with titanium wire is electrically heated. This sublimates titanium into the vessel and onto the walls. The filament is partially surrounded by a cooled copper shell which acts as a heat shield, protecting the glass of the nearby vessel walls from direct radiation. The present system coats approximately 30% of the vessel surface with titanium; getter runs are usually ten minutes long, and are performed once or twice per run day.

The vacuum pump system is mounted in a stand separate from the tokamak. It is illustrated in Figure 4-4. The pump manifold is connected to the tokamak by a pair of bellows epoxied into two ports on the bottom of the vessel (see Figure 4-3.) The connection is made by a quick-connect fitting on each bellows, which allows the vacuum system to be completely disconnected from the vessel. The pump manifold is connected by an L-shaped section of 15 cm diameter pipe to the high-speed vacuum pump, a Leybold-Heraus 300 liter per second turbomolecular pump (TMP). The TMP is backed by a standard mechanical pump. All of the vacuum gauges are located in this pump stack. An unshielded ionization gauge and a thermocouple gauge are located in a Conflat tee near the pump manifold. Another thermocouple gauge is located between the TMP and the roughing pump to give the fore-line pressure. Two hydraulic gate valves are incorporated into the pump stand; these are used to isolate various parts of the vacuum system for safety or maintenance purposes. A 15 cm VAT gate valve is installed between the pump manifold and the TMP; this valve isolates the vacuum vessel from the TMP in case the pump stops for any reason (e.g., power or mechanical failures), and protects the TMP from an accidental vent of the vessel to

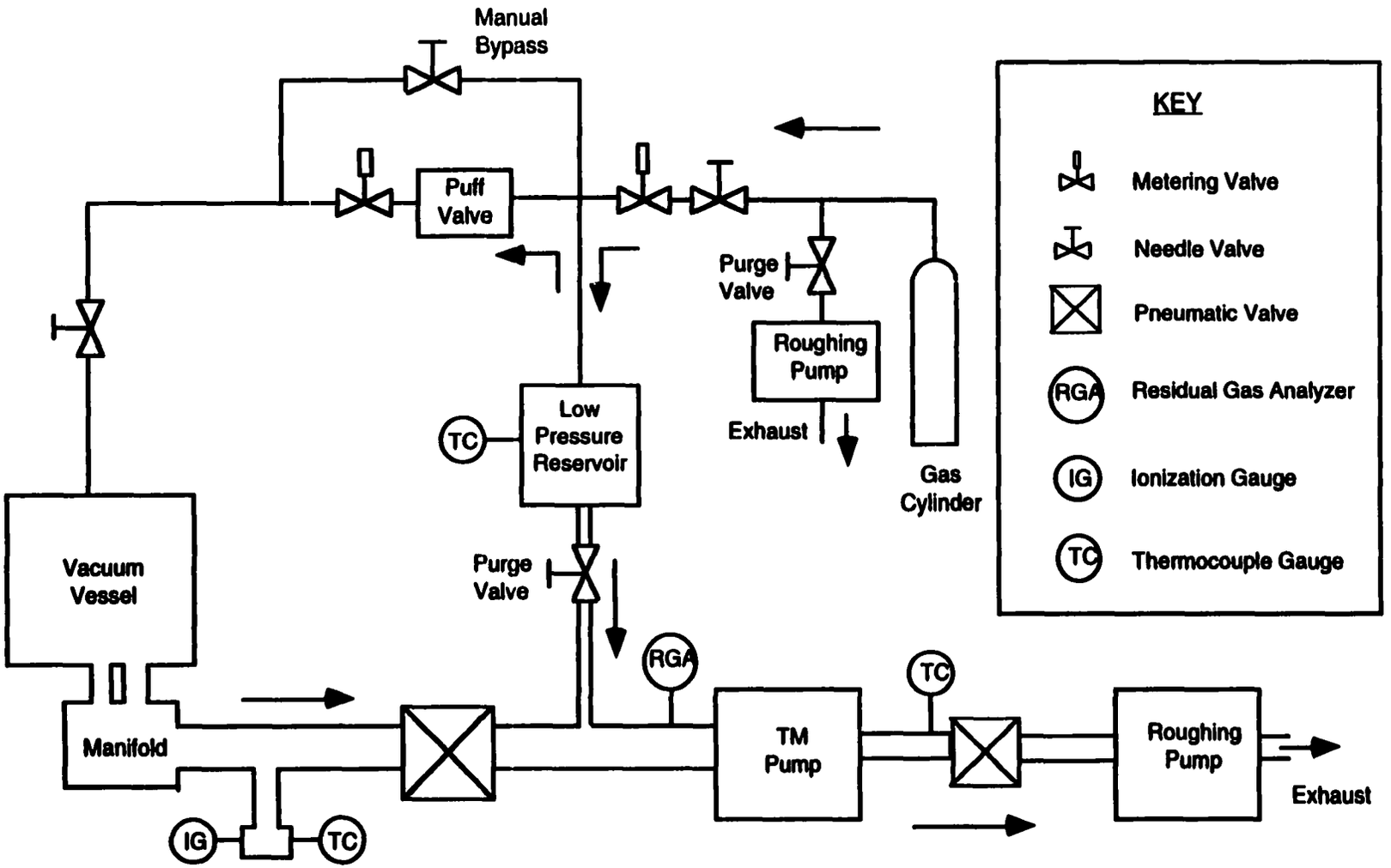

Figure 4-4. Schematic of the MEDUSA vacuum and gas supply systems. Thin lines are 0.5-cm gas pipe; open lines indicate vacuum ducting. Arrows indicate normal directions of gas flow.

the atmosphere. A smaller VAT gate valve between the TMP and the roughing pump protects the TMP from overpressure in the fore line. The various pumps, valves, and gauges are all connected through a relay interlock system, which has a logic flow that protects the pump and/or vessel under any number of failures. This system will automatically shut valves and turn off pumps if certain criteria (such as overpressures, or a weak flow of cooling water to the TMP) are met. It also allows these systems to be reset once the adverse conditions are eliminated. Finally, a Balzers QMG 064 residual gas analyzer (RGA) is also located in the pump stand. The RGA is used for helium leak checking and for determining what gases are present in the vacuum system. The entire vacuum system ductwork (apart from the bellows) is made of stainless steel.

The combination of strong pumping, titanium gettering, plasma scrubbing, laboratory climate control, and careful vacuum procedures gives a typical base pressure of the MEDUSA vacuum of around 2×10^{-7} torr, which is approximately 2.7×10^{-5} Pa. After a ten minute getter cycle, the base pressure is usually on the order of 5×10^{-8} torr.

4.3 Magnet Coils

There are four independently-driven magnet coil sets on MEDUSA: the toroidal field (TF) set, the ohmic induction set (OH), the vertical or equilibrium set (VF), and a radial error field correction set. These coils are shown in Figure 4-2. All of these coils are made of copper.

The toroidal field system is comprised of nine three-turn coils. The coils are essentially square in shape, with an outer dimension of 37 cm. The three non-core (i.e., top, bottom, and outer) legs of each coil are constructed of rectangular copper bar stock with sides of 2.5 cm and 0.625 cm. The narrow sides face the vacuum vessel; this arrangement

makes the coils much stronger against expansion stresses. The coils are held in place by the garolite plates and tokamak torque frame that are discussed in the next section. The three turns that comprise each coil are electrically insulated from each other by thin sheets of "blue paper" mylar insulation inserted into all the coils.The twenty-seven inner legs are distributed uniformly and sequentially around the induction solenoid. These inner legs are 32.7 centimeters long and have a 6 mm by 25 mm rectangular cross-section. The inner legs are epoxied together with 3M Scotch-Weld™ EC-2216 epoxy, and are electrically insulated from the induction solenoid.

The TF coils are demountable from the tokamak. The outer and upper legs of each turn are soldered together into an "L." The inner legs are bent and twisted 90° at their bottom ends so that they can be soldered to the bottom legs. The bottom leg of each coil is connected to the outer leg by a removable, insulated 1/4"-20 bolt. The upper leg meets the inner leg by means of two mating pads. A length of 6 mm by 25 mm copper stock is soldered to the inner end of the top leg; a small copper block is soldered to the other end of each of these strips. This pad is mated to a similar pad soldered to each of the inner legs; these two pads are held together by two 6-32 bolts. By removing the large bolt at the lower outer corner and the two small bolts at the upper inner corner of each coil, the top halves of all of the TF coils can be removed for access to the vacuum vessel.

The jump from one turn to the next, and from one coil to the next, is made at the outer lower corner. Current is carried between the coils by 13 mm × 1.5 mm copper straps. These straps are soldered to 2.5 cm square copper plates, which are held together with the bolt assembly at these corners. The return for the entire system is made of the same strap and runs anti-parallel to these strips. The return travels completely around the TF cage in order to minimize field errors associated with the coil feeds.

The maximum toroidal field achievable on MEDUSA is 0.45 Tesla at a major radius

of 0.12 m (1.8 Tesla at the inner coil), which corresponds to a coil current of 10 kA. This limit is set by resistive heating of the thin inner legs. Typically the toroidal field is set to 0.25 or 0.3 Tesla for operation. This coil system has a resistance of 29 milliohms and an inductance of 2.9×10^{-4} H.

Ohmic induction for startup and current drive is provided by the ohmic heating system. This system consists of two sets of coils connected in series. The primary coil in this system is the induction solenoid. The solenoid is constructed of 3 mm by 6.5 mm copper strip wound in two layers around a hollow G-10 cylinder with a 1.9 cm radius. The solenoid has a 2.7 cm radius and is 68 cm tall; there are 188 total turns. The solenoid is strengthened with fiberglass tape and sheets, and is held together with 3M 2216 epoxy. The central tube of the solenoid is fitted for water cooling, but this has not been implemented. The second component in the OH system is the trim coil set. This is a pair of circular coils, three turns each, wound of 1.5 mm by 13 mm copper strip. These coils have a mean radius of 16 cm, and are located 41.5 cm above and below the vessel midplane.

These two coil sets combine to produce an ohmic startup null, illustrated in Figure 4-5. This null arrangement keeps the OH poloidal field on the plasma midplane to below 5 Gauss at 10 kA of coil current. The current limit of the OH system is set by the stress limit on the copper in the induction solenoid. This stress exceeds one-quarter of the yield stress of copper at 16 kA (which is one-half the current required to reach this stress.) Therefore, the OH system is limited to 16 kA to maintain the life of the core. This produces a maximum field of 5.6 Tesla in the magnet, which gives 10 mV-s of poloidal flux with a single swing. This coil set has a resistance of 35 milliohms and an inductance of 9.7×10^{-5} H.

The third coil system to discuss is the vertical field (VF) system. This system is composed of a pair of seven-turn coils located at a height of 0.20 m and radii between 0.30 and 0.35 m. These coils are potted in 3M 2216 epoxy. The pair is run in series. The VF coil

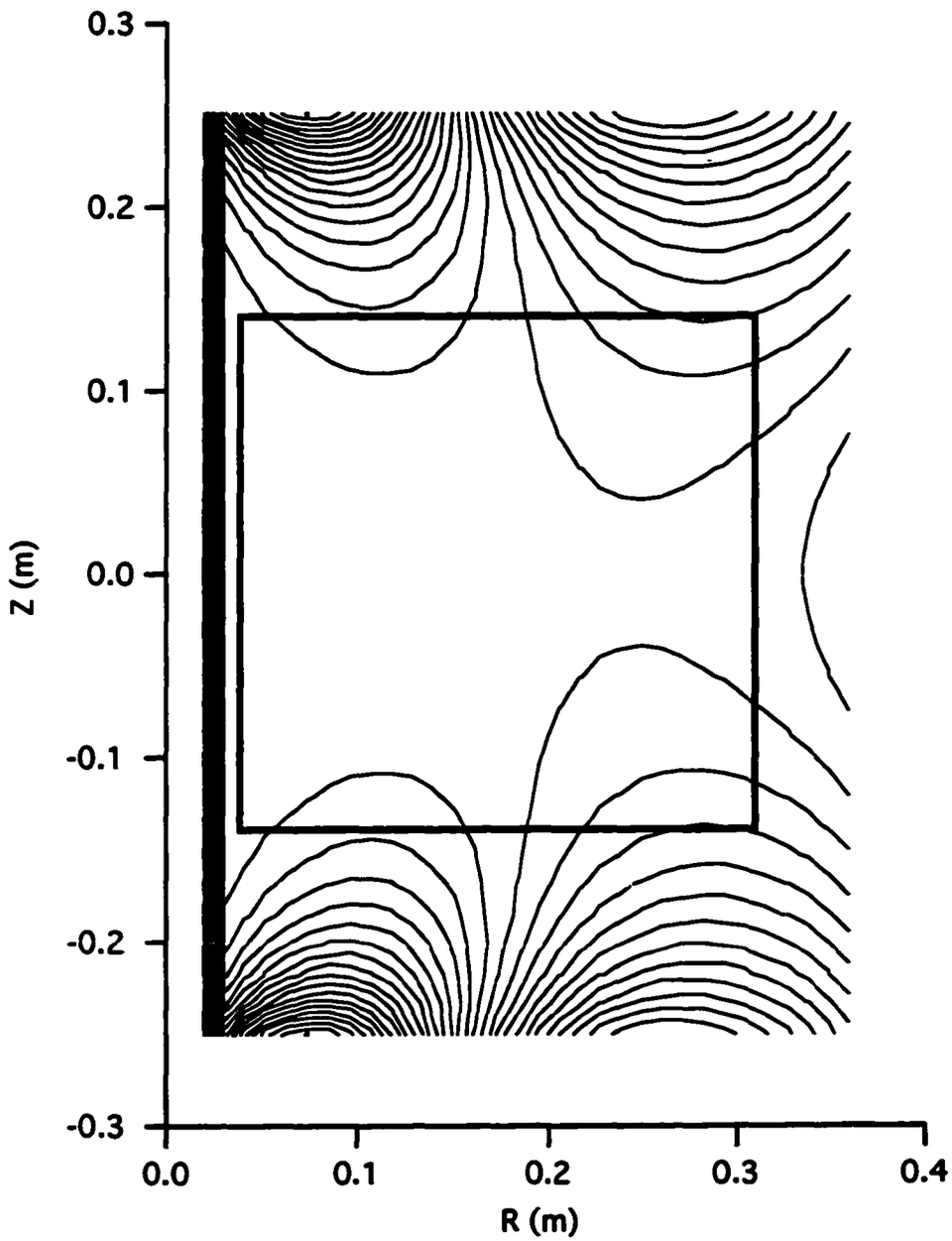

Figure 4-5. Ohmic startup null. Contours are vacuum flux surfaces. The heavy lines represent the vacuum vessel.

system has a resistance of 15 milliohms and an inductance of 1.8×10^{-4} H. The vacuum flux contours of the VF system are illustrated in Figure 4-6.

Since the OH and VF systems both produce poloidal flux, they are linked magnetically. The mutual inductance between two coils, 1 and 2, that intercept flux from each other, is

$$M_{12} = \frac{\Phi_{12}}{I_1} = \frac{1}{I_1}\oint_2 \mathbf{A}_1 \cdot d\mathbf{l} \qquad (4\text{-}1)$$

where M_{12} is the mutual inductance of circuit 2 with respect to circuit 1, Φ_{12} is the flux from circuit 1 intercepted by circuit 2, and $\mathbf{A}_1$ is the vector potential of circuit 1 [6]. The equation for an un-driven circuit containing a mutual inductance is

$$\frac{1}{C_1}\int_0^t I_1(\tau)d\tau + R_1 I_1 + L_1\frac{dI_1}{dt} + M_{21}\frac{dI_2}{dt} = 0 \qquad (4\text{-}2)$$

where the subscripts refer to circuit numbers. The meaning of these equations for MEDUSA is that changing current in either the OH or VF coils causes a back-voltage on the other. This effect is counteracted by introducing an additional mutual inductance into the system. This additional inductance has a magnitude equal to the mutual inductance due to the coils, but has opposite sign. This additional mutual inductance is added in the form of a decoupling transformer in the transmission lines for the OH and VF systems, where the handedness of one of the coils is reversed with regard to their relationship on the tokamak. With this addition, the control of these two coil systems are essentially independent.

The fourth coil system on MEDUSA is the error field correction set. These coils are similar in construction to the VF coils. They are located at a height of 0.20 m above and below the midplane and a radius of 0.16 m. Each coil has 5 turns in series. These coils are

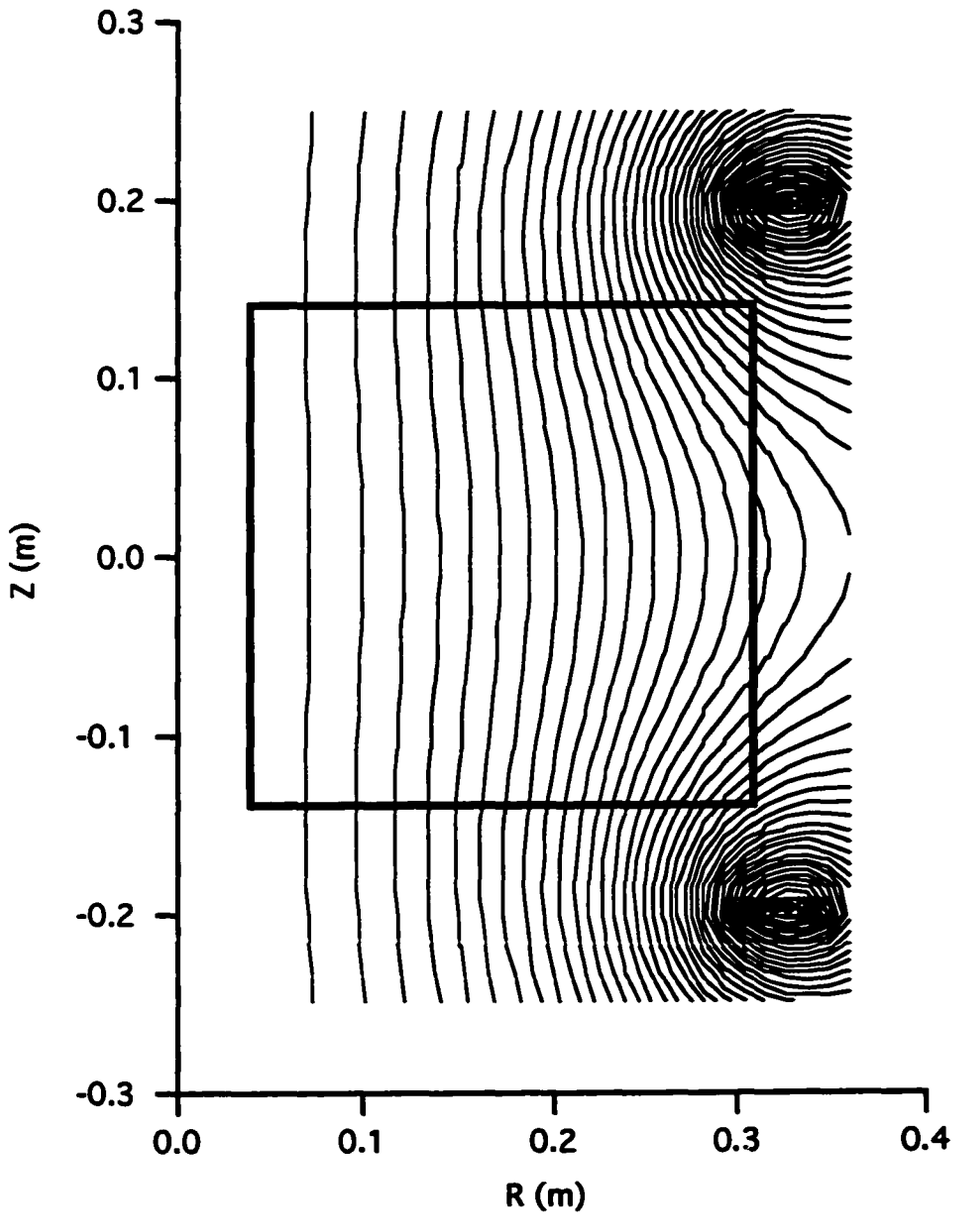

Figure 4-6. Vacuum flux contours of the vertical field system.

operated with opposing helicities in order to generate a small inward radial field to correct errors in the OH system. Typically this coil system operated at currents of less than 100 A. This system has not been used since the new OH system was installed, as this upgrade eliminated the major field error that was present previously.

4.4 Mechanical Assembly

The MEDUSA vacuum vessel and magnet coils are held together by a mechanical superstructure. The primary features of this superstructure are two garolite (phenolic) plates above and below the vacuum vessel. These plates are circular, with a radius of 0.33 m and a thickness of 2.5 cm. All of the coils discussed in Section 4.3 are mounted directly to these plates. The support structure is designed so that there is a minimum clearance of 0.6 cm between the vacuum vessel and any magnet coil. The toroidal field coils are held in radial grooves cut in the in-sides of the plates; cap screws through the plates thread into these coils to hold them tightly. The vertical field and error correction coils are fit into annular grooves cut into the out-sides of the plates, and are clamped down. The solenoid is anchored to the plates by hold-down assemblies on the top and bottom of the central rod. The trim coils are attached by threaded rods that screw into the plates and into the coil forms. The vacuum vessel is supported by three aluminum blocks attached to the top side of the lower plate; viton pads between the blocks and the bottom glass plate act as shock absorbers. Other than this, the vessel has no connection to the support structure. Circular holes cut in the plates correspond to the port locations in the vacuum vessel and allow diagnostics to pass through. However, none of the equipment passing through these holes is connected to the support plates; the impulse caused by the plasma discharge could otherwise force them loose from the vacuum seals and vent the tokamak. The lower support plate attaches to an aluminum stand (designed to minimize eddy currents) which is anchored to the floor; the stand holds

the tokamak approximately 1 meter above the floor.

Another feature of the superstructure is the torque frame. In any tokamak, the current in the toroidal field coils crossed with the magnetic field of the equilibrium system leads to an overturning moment. In MEDUSA, the resultant torque is on the order of 4 kN-m for a typical 0.3 T shot. This moment tends to collapse the TF cage by counter-rotating the top and bottom legs of the coils. To prevent this, the torque frame holds the TF coils stiffly together. In MEDUSA, the torque frame consists of lengths of angle aluminum, 2.5 cm per side, which are clamped tightly near the top and bottom of each TF coil. The resultant box structure is quite strong. The torque frame, coupled with the stiff support plates, effectively counteracts the overturning moment.

In general, the magnet coils and current feeds on the tokamak are strongly clamped. The MEDUSA coils are high current / low voltage coils; they must therefore be strongly clamped. Most current feed straps are secured by simple bar clamps every few centimeters. For example, the current straps for the TF feed and return, which see a repulsive force of approximately 5 kN/m, are clamped every 6 cm. The OH feeds are clamped at about the same interval, while the other systems are not as heavily restrained.

A final component of the mechanical structure is the shrapnel shield. The glass vessel demands a large degree of caution while under vacuum. In case of a catastrophic failure of the chamber, lexan sheets are attached between all of the outside legs of the toroidal field cage. These sheets of bulletproof plastic would contain any shrapnel travelling radially outward from such a failure. The support plates would of course contain upward and downward moving shrapnel. The lexan sheets and support plates also protect the vessel from inadvertent damage from tools and other hazards in the laboratory.

4.5 Power Supplies

Electrical power for the various MEDUSA coil sets is supplied by banks of capacitors. The majority of these capacitors are 450 V, 1.5 mF electrolytics, although a few banks for the OH system are composed of oil-based capacitors. Table 4-2 lists all of the capacitor banks on MEDUSA. Each capacitor bank is grouped with other banks to form the power supply for one individual coil set. Current to the coil sets is measured by Rogowski coils on the transmission lines. Each bank can be charged to a voltage independent of the other banks, and can be fired independently at an arbitrary time. These voltages and firing times are set in the control system, discussed in Section 4.6.

Each bank is fired through a silicon controlled-rectifier (SCR), which acts essentially as a triggerable diode. Several different models of SCR are used, but the most commonly used ones are Power Semiconductors Inc. part Z1200 38 and International Rectifier part ST1200C22K0. Each SCR is fired by a 30 volt, 20 microsecond pulse provided by the control system. An SCR may be turned off by forcing the anode to a higher voltage than the cathode; the resulting negative current will commutate the SCR out of the circuit.

The entire power supply system shares a common ground plane at the tokamak. This plane is connected by 4/0 welding cable to a hard ground outside the building. No other grounds exist on the capacitor banks; the capacitor terminals are not grounded during a shot, and usually sit several tens of volts below ground due to resistive losses in the transmission lines. Transmission lines for all the banks are 4/0 or 1/0 stranded welding cable, fastened tightly together to minimize stray magnetic fields and counteract the repulsive JxB forces generated during a shot.

The capacitor banks are charged by several DC power supplies. The 450 V banks share one 450 V power supply; the control system sets the voltage of each bank. The higher voltage banks each have their own supply, although the charging is still monitored by

System / Bank	Number of Banks	Capacitance (mF)	Max Voltage (V)
TF	**5**		
TF-1 *	1	42	900
TF-2,3,4,5 *	4	60	450
OH	**6**		
OH-0 *	1	0.75 - 9	3800
OH-BB *	1	1 - 3	3800
OH-1	1	6.8	1800
OH-2,3,4	3	60	450
VF	**3**		
VF-0 *	1	0.25 - 5	900 - 1800
VF-1	1	24	450
VF-2	1	120	450
RE	**1**		
RE-1	1	24	450

Table 4-2. List of all MEDUSA capacitor banks. Starred (*) banks are those used routinely.

the control system. See Section 4.6 for more detail.

The operation of each capacitor bank set can be illustrated by examining the toroidal field system. The electrical circuit for the TF power supply is illustrated in Figure 4-7. A typical TF current waveform is illustrated in Figure 4-8. There are five banks, each with its own charging line and SCR. Each SCR is "snubbed" with a resistor and capacitor in parallel with the switch. This snubber circuit filters out high-frequency voltage spikes that can damage the SCR. The banks are brought to the preprogrammed voltages and held there until a shot is initiated. When the discharge is initiated, the first bank (TF-1) is fired, ramping the current up to the target value in about 3 ms. At this point the voltage on the first bank has fallen from the initial setting of 500-900 V to near zero. Now the succeeding bank is fired to maintain the flat-top. Since this bank is at a higher voltage than TF-1, the reverse current commutates the first bank out of the circuit, leaving the second bank driving the coil. This bank maintains the flat-top for 1 ms, when another bank is used to continue the flat-top. In typical operation, TF-1, TF-3 and TF-4 are used. After the final bank has fired, its voltage drops below zero as the current peaks. Since these banks are composed of electrolytic capacitors, which cannot stand a reverse polarity condition, a diode is installed in parallel to the bank and capacitor leg of the circuit. The diode closes, effectively removing the capacitor bank from the circuit and allowing the current in the coil to decay with its L/R time.

The other coil systems function similarly, albeit with different waveforms. The OH system typically uses one or two banks, and the VF system is almost always operated with one bank, relying on the long L/R time of this coil (12 ms) to maintain the plasma equilibrium after the bank has discharged.

In the interest of safety, emergency dump relays are incorporated into each individual bank. These switches connect the active terminals of the banks, through bleed resistors, directly to ground. (The common terminals are grounded through the transmission lines.)

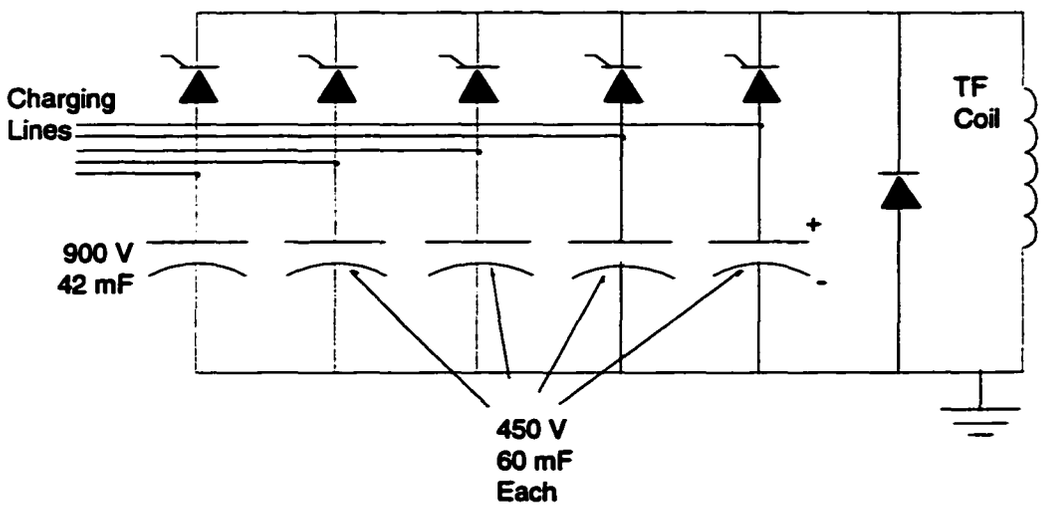

Figure 4-7. Schematic of the toroidal field power supply system.

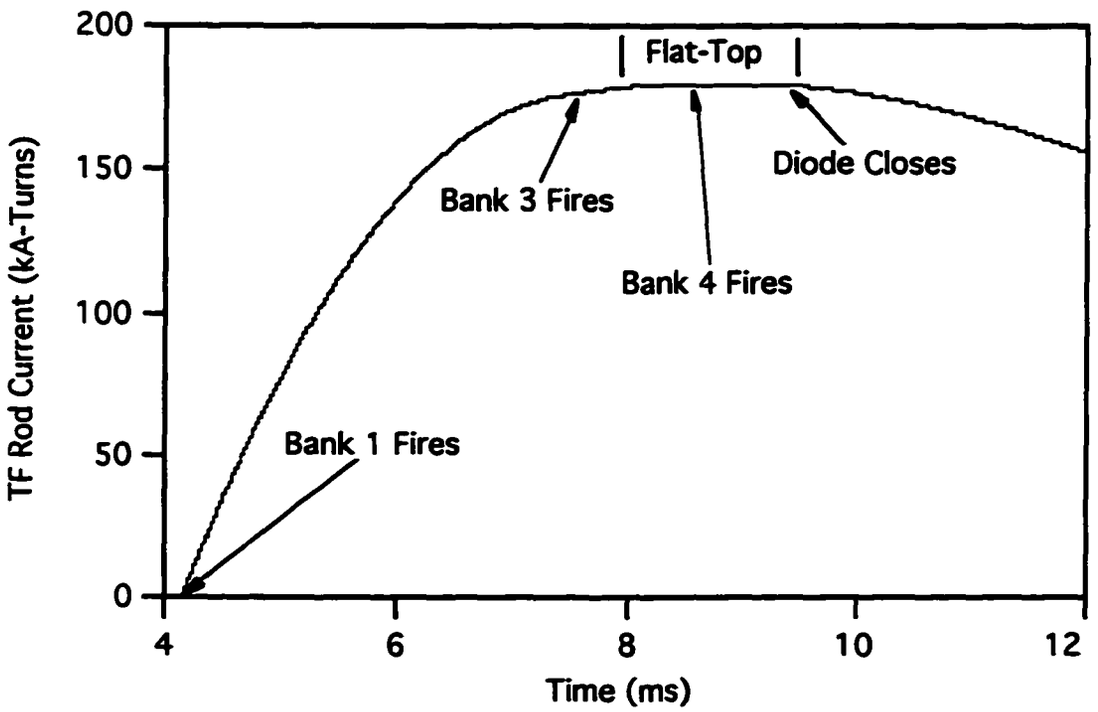

Figure 4-8. Typical toroidal field current waveform.

When the relays close, they effectively discharge the banks over a few seconds. The relays are normally closed, and can only be opened when energized by the operator. They naturally close during power outages, providing a fail-safe condition. The relays are always closed when any work is performed on the tokamak, power supplies, or control electronics.

4.6 Control System

Control and data acquisition for MEDUSA are performed by desktop computers working with interface electronics. Figure 4-9 provides a schematic overview of the control and data acquisition systems. This section will discuss the control system, while Section 4.7 describes the data acquisition system.

Control for MEDUSA is provided by a Gateway 486/66 MHz PC. The control software is written using National Instruments' LabView for Windows package; LabView is a graphical programming language. The control program offers the operator a graphical interface, which is used to set parameters for the tokamak operation. The operator is able to set individual capacitor bank voltages and discharge times, timings for the gas puff and ECR systems, and various other trigger times for diagnostics and data acquisition; he or she can control whether each individual timing pulse is sent. The operator also determines the state of the power supply safety relays and the state of capacitor bank charging (on or off). The operator can, of course, initiate the discharge. The user interface provides the operator with real-time information on the capacitor bank voltages, base vacuum pressure, and the state of the safety relays and charging system. It keeps track of the shot number, and provides the time elapsed since the latest shot.

The capacitor bank charge control and monitor system is illustrated in Figure 4-10. The control computer houses two National Instruments LabPC I/O boards. One of these boards (the digital control board) controls TTL-level signals sent to interface electronics.

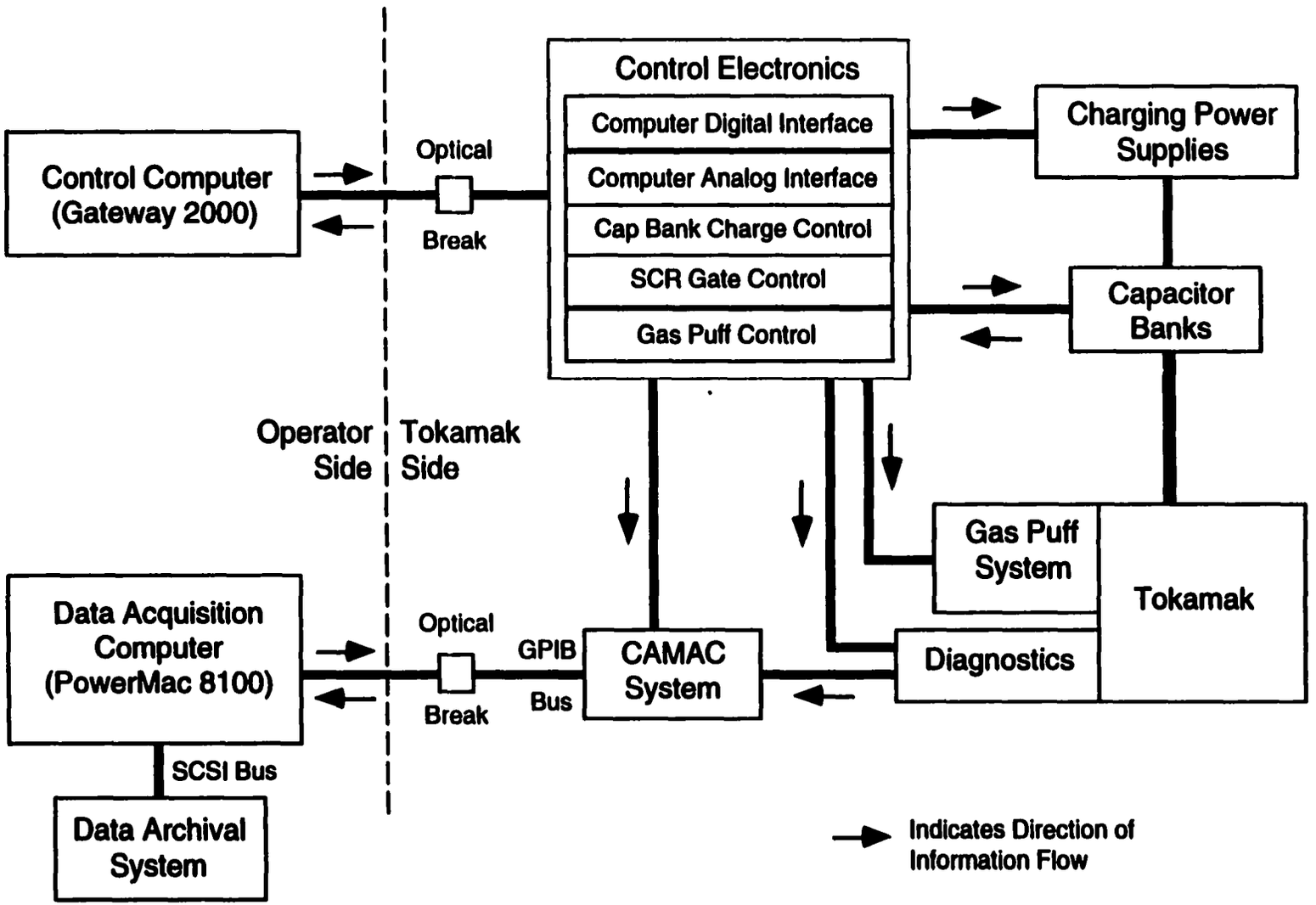

Figure 4-9. Schematic overview of MEDUSA control and data acquisition systems.

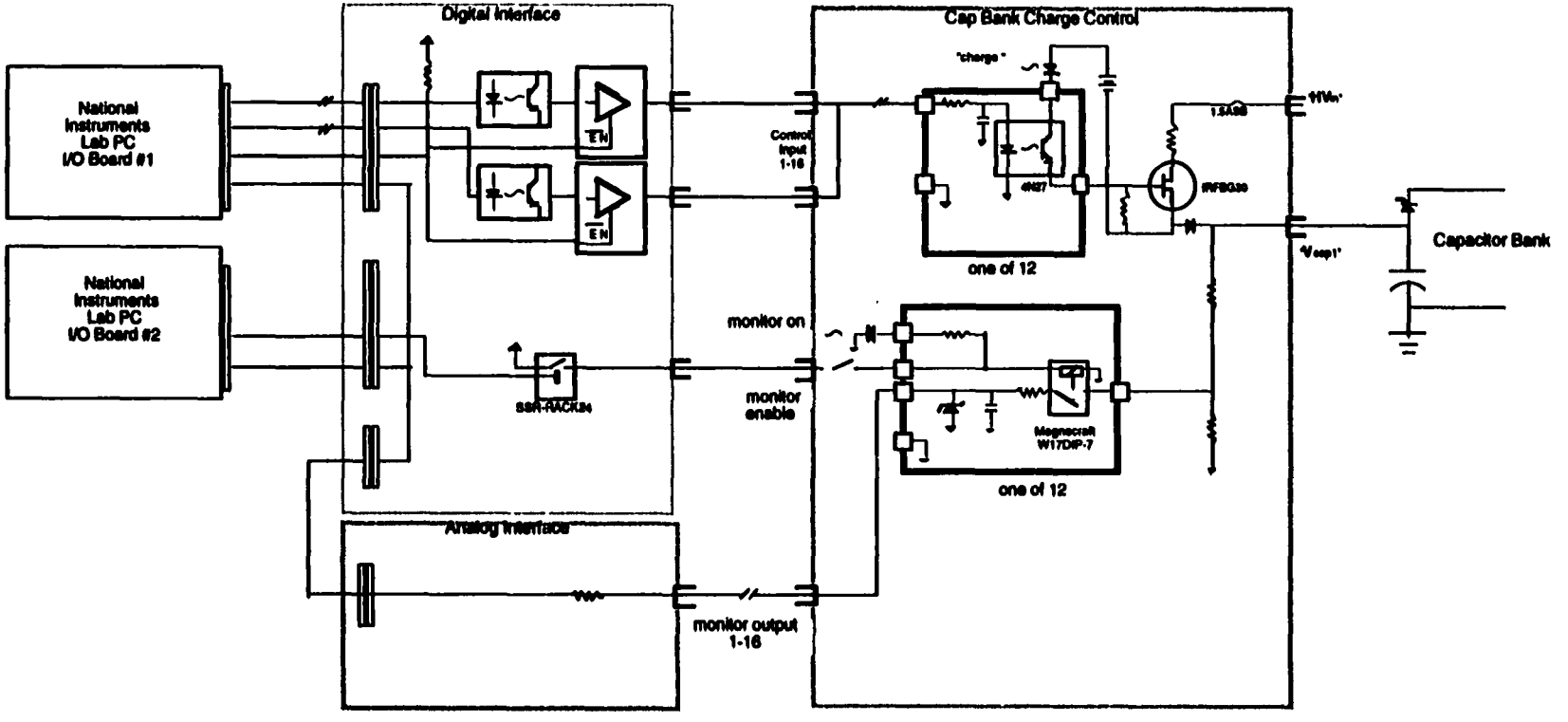

Figure 4-10. Capacitor bank charge control and monitor circuits

Each capacitor bank has its own "channel." Each interface channel consists primarily of an optical break and a switch, either a MOSFET for the 450 V banks (as illustrated) or a relay for the higher voltage banks. The switches allow current from the charging power supplies to pass to the capacitor banks; the state of the switches is set by the control levels sent by the digital board. Meanwhile, the bank voltages are monitored (through another set of interface electronics) by the second control board (A/D). This board reports these voltages to the LabView control program. LabView compares the reported voltages to the setpoint voltages entered by the operator. The state of each control line is then set based on the comparison of the two voltages. This bang-bang control system can simultaneously charge and monitor 16 separate capacitor banks.

Timing pulses are provided by two National Instruments Lab PC TIO-10 timing boards that reside in the control computer. Each of these boards can supply eight independently timed TTL-level pulses with 1 microsecond precision. One of these sixteen signals is used as a data acquisition trigger. Another signal is used to control the fill gas puff, and a third is used to trigger the ECR system. Yet another timing signal triggers the fast LCD shutter for the CCD camera, if it is in use. The remainder of the pulses can be used to fire the capacitor bank SCRs. A single channel of the SCR firing control circuitry is illustrated in Figure 4-11. The timing pulse for a particular channel is first passed through an opto-isolator. The resulting signal is used to trigger a very small SCR, discharging a small capacitor, which is charged to 30 V, through a pulse transformer. The secondary of the transformer carries the signal to the bank SCR, which is floating with regard to ground. The signal is terminated and snubbed (to protect against high-voltage transients) at the SCR.

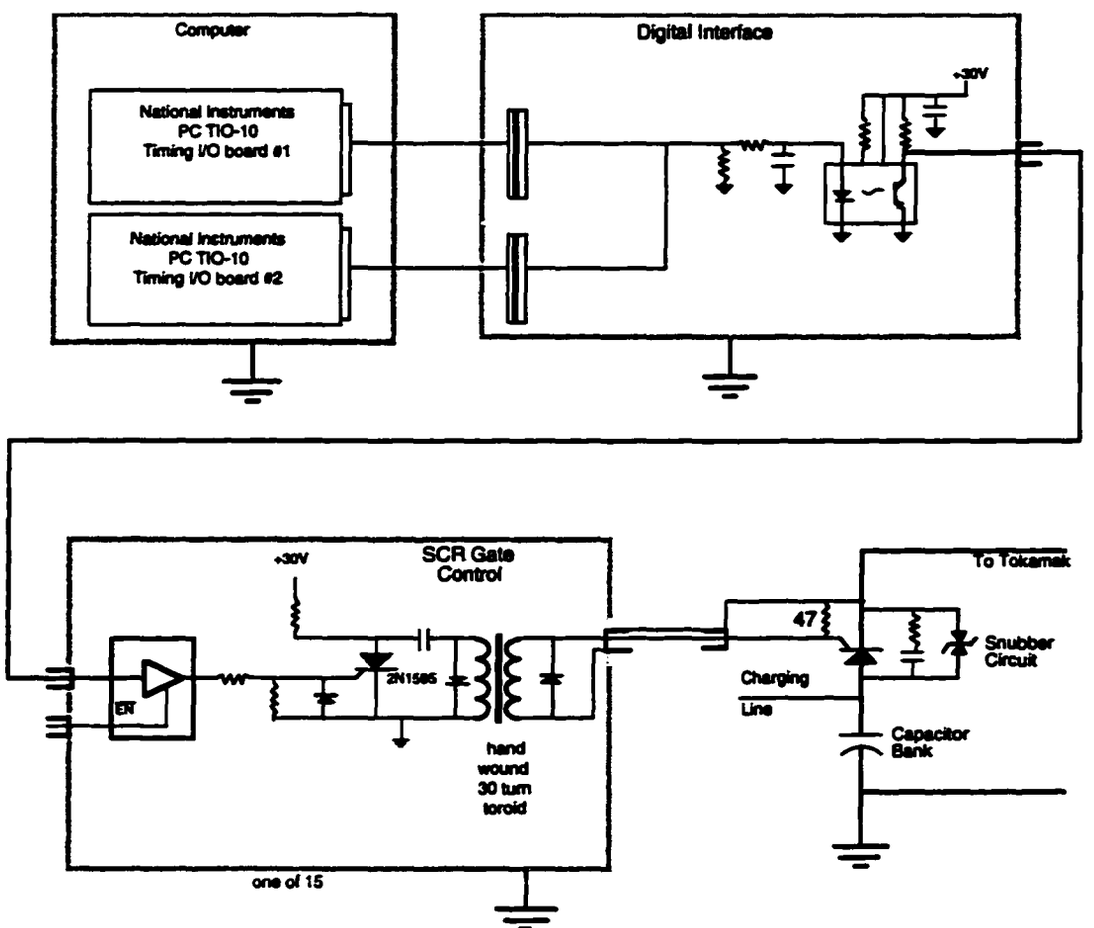

Figure 4-11. SCR firing circuit.

4.7 Data Acquisition System

The MEDUSA data acquisition system (DAS) is CAMAC based, with a desktop computer to provide the data download, analysis, and storage functions. The DAS is illustrated schematically in Figure 4-12..

The actual diagnostic waveform recording is provided by a CAMAC system. Two CAMAC crates house three different types of waveform digitizers. The "primary" digitizers are two Joerger Instruments' 612/3 (6 channels each, 1 MHz, 12 bit, ±10 V). The 612s are usually used to record coil currents, loop voltage, plasma current, and magnetic and electrostatic probe data. The second set of digitizers are four LeCroy 6810 modules (4 channels each, 12 bit, 1 MHz, ±100 V). The 6810s are used primarily for flux loops and Mirnov coils. The final set of digitizers are LeCroy 8212 waveform recorders (4 channels each, 12 bit, 40 KHz, ± 10 V). The 8212s are not routinely used because of their slow sampling rate.

The control modules for the CAMAC crates are designed for use with the GPIB (General Purpose Interface Bus) data transfer protocol. These modules are connected via GPIB data highway to the acquisition computer. The highway contains an optical break that protects the operator from voltage surges on the diagnostics or crate power supplies. The data highway terminates at a GPIB interface board housed in the DAS computer.

An Apple Power Macintosh 8100/100 MHz computer controls the DAS. Wavemetrics' Igor Pro software package (essentially a high-level data manipulation language) is used to handle the data and communicate with the hardware. The computer configures the digitizers (sample rate and size, number of channels, voltage range, etc.) The computer also arms the digitizers before each shot. Data is retrieved from the digitizers following each discharge, and is automatically displayed by the computer. Certain waveforms are processed before display, such as coil and plasma currents.

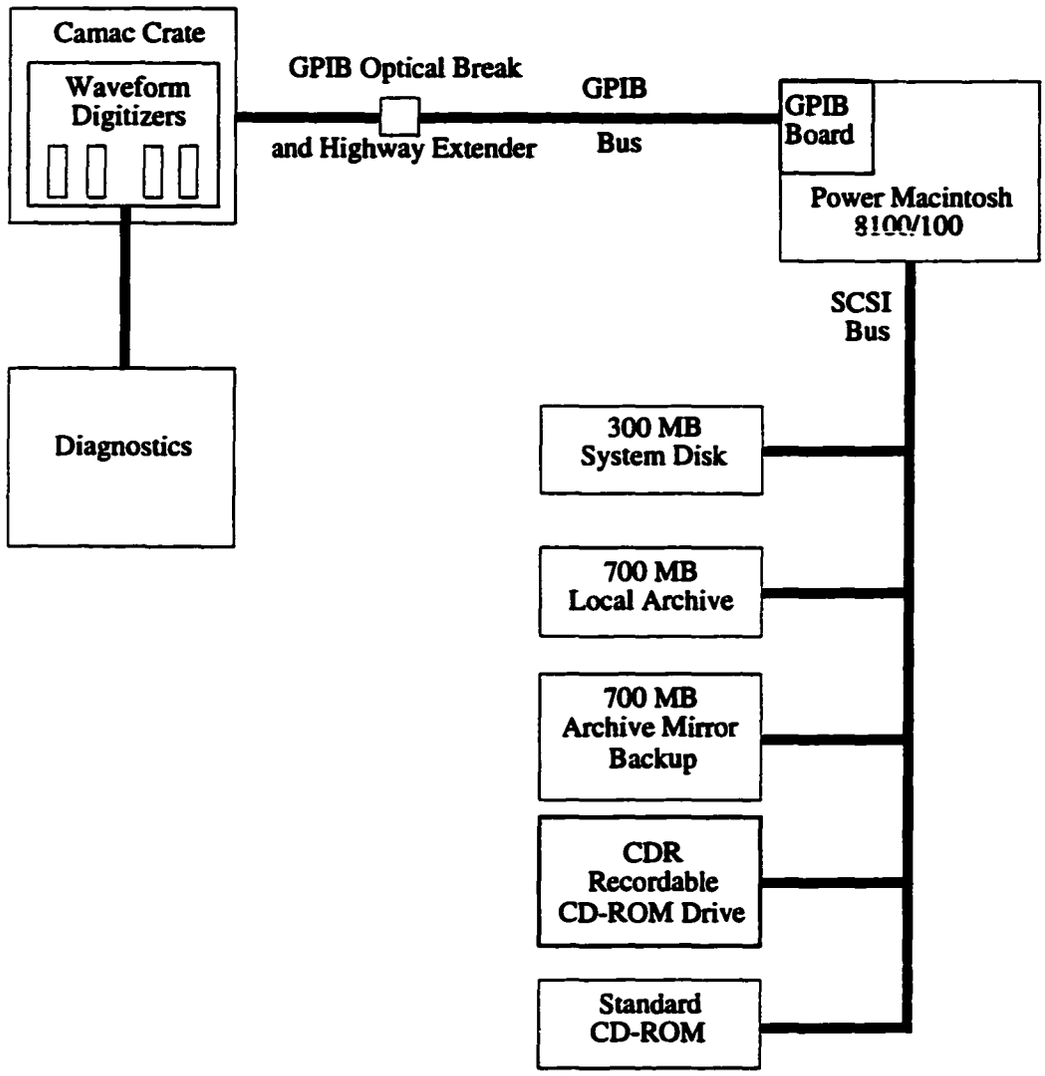

Figure 4-12. MEDUSA data acquisition system.

All of the data is immediately archived upon retrieval. Data is archived on three different storage systems. After a shot, all of the raw data is read into the computer memory. It is then written to a local 700 MB archive disk and an identical archive mirror. Each data wave is stored in its own file which is named by shot number and diagnostic (e.g. "13563_PL_Rogow"). At intervals (as the disks fill up), this data is transferred to compact disk by a CDR recordable CD-ROM drive. This data can then be read from the CDs by a standard CD-ROM drive in the control computer.

4.8 Diagnostics

The primary diagnostics on MEDUSA are external magnetics. These include coil current Rogowski coils, the plasma Rogowski coil, flux loops, and Mirnov coils. The coil current Rogowski coils are located on the capacitor bank transmission lines. The positions of the other external magnetic diagnostics are shown in Figure 4-13.

A flux loop is, in its simplest form, a wire located at a single poloidal location but making a complete toroidal rotation around a tokamak. (Some of this discussion of flux loops and Rogowski coils is from [7].) The leads from this loop are twisted together so that the only field it measures is in the loop itself. Faraday's law relates the magnetic field within this loop to the integrated electric field (the loop voltage) along the contour:

$$V_{loop} = \oint_C \mathbf{E}\cdot d\mathbf{l} = -\int_S \frac{d\mathbf{B}}{dt}\cdot d\mathbf{A} = -\frac{d\Phi}{dt} \qquad (4\text{-}3)$$

where the contour integral is taken around the loop and the area integral is taken over the surface enclosed by *C*. Thus the integral of the measured voltage with respect to time gives a direct measurement of the magnetic flux passing through such a loop. The measurement of these fluxes is extremely useful in reconstructing the plasma equilibrium, which is essentially the determination of the flux at points inside and about the plasma.

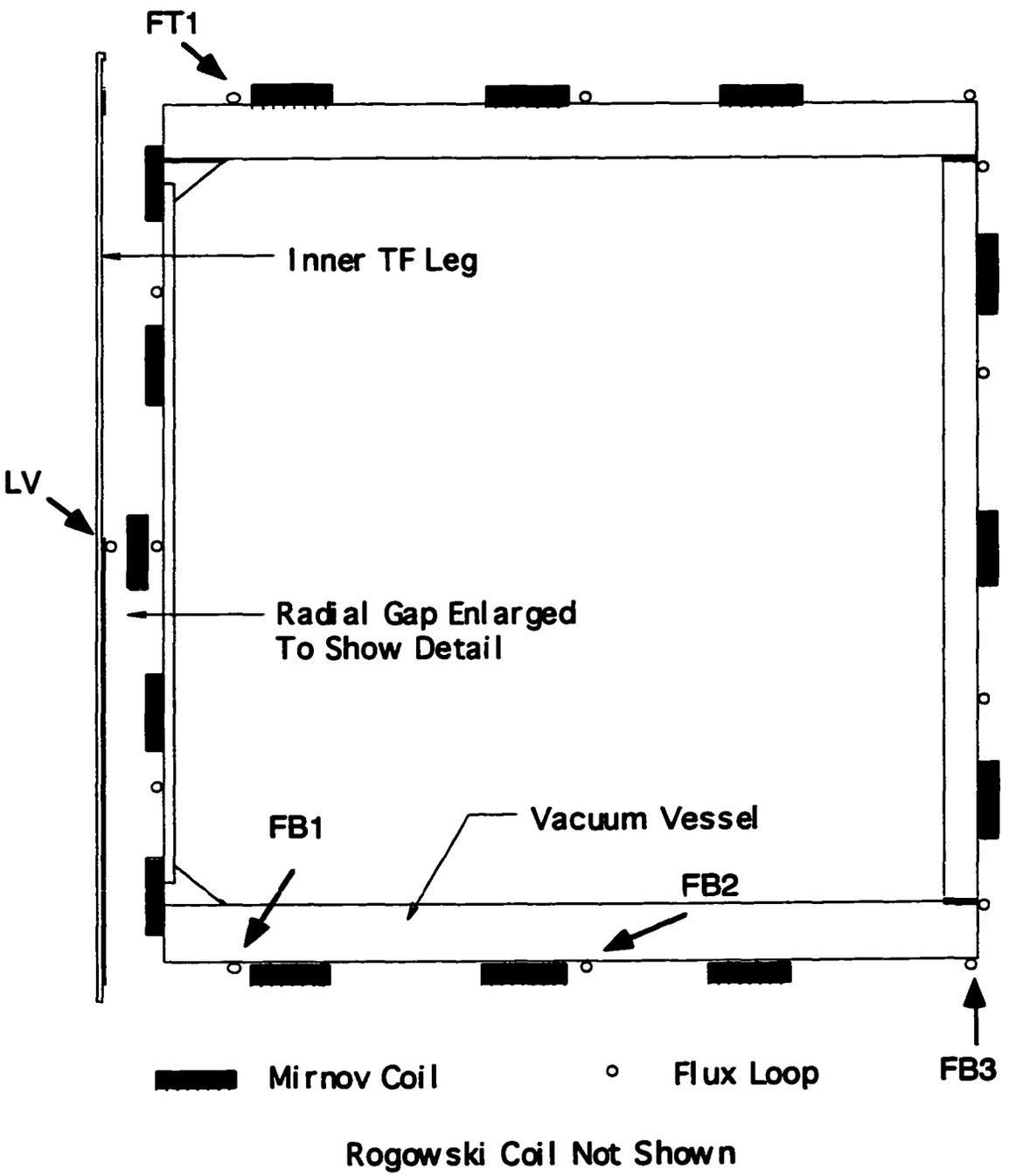

Figure 4-13. Positions of MEDUSA external magnetics.

A Rogowski coil is a solenoid that has been wrapped onto a closed contour around some current-carrying element. The coil is either back-wound, with two layers of windings, or else one lead of the coil follows the contour of the coil back to the other lead. This is done so that the coil measures only the poloidal field of the current-carrying element. Generalizing equation 4-3 for a solenoid with *n* turns per unit length arranged around a contour gives, for *1/n* much larger than the scale length of the magnetic field:

$$\Phi = nA\oint_C \mathbf{B}\cdot d\mathbf{l} \tag{4-4}$$

where *A* is the area of the loop and *B* is near constant over *A*.

Finally, Ampere's law states:

$$\oint_l \mathbf{B}\cdot d\mathbf{l} = \mu_0 I \tag{4-5}$$

where the integral is taken over a contour around a conductor and *I* is the current in the conductor. Combining equations 4-4 and 4-5 and taking the derivative with respect to time gives:

$$V = \frac{d\Phi}{dt} = nA\mu_0 \frac{dI}{dt} \tag{4-6}$$

where *V* is the measured voltage out of the Rogowski coil. Thus the measured voltage out of such a coil is a direct measurement of the *dI/dt*; integrating this voltage gives the total current in the current-carrying element.

Mirnov, or pickup, coils are simply small coils located in a single toroidal plane that measure the poloidal field of the plasma. Since these coils are located in poloidal space, they see spatial and temporal variations in the field that a Rogowski coil would integrate out. Thus Mirnov coils are well-suited to measuring perturbations associated with MHD instabilities such as magnetic islands.

MEDUSA has fourteen flux loops, fourteen Mirnov coils, and one plasma Rogowski coil. The Mirnov and Rogowski coils consist of insulated magnet wire wound tightly around a rectangular garolite form, 2.5 mm by 5 mm in cross-section. Each individual coil is coated with a thin layer of household epoxy to maintain its shape. The Rogowski coil consists of four straight, independent legs in a single toroidal plane. The legs are placed flush against the outer surfaces of the vacuum vessel, and the ends of each leg are butted against the adjacent legs. The legs are connected electrically (in series) away from the tokamak. The Mirnov coils are also located in a single toroidal plane, and are similar in construction to the Rogowski coils. The Mirnov coils are approximately 2 cm long. Since the Mirnov coils are laid flush against the vessel wall and the MEDUSA vacuum vessel has a rectangular cross-section, the Mirnov coils do not in fact measure the poloidal field strictly. Rather, they measure either the Z component of the field (inner and outer coils) or the R component (top and bottom coils). The flux loops are single turns of magnet wire located at various poloidal positions. Two loops inside the inner wall are arranged concentrically so that the plasma surface loop voltage may be extrapolated.

MEDUSA is equipped with a fast-framing CCD camera that can take one exposure of the plasma each shot. The camera is a Cohu video CCD camera that is fitted with a Displaytech VS2200 fast liquid-crystal shutter. This shutter allows exposures as short as 50 microseconds. The camera has been used mostly in the early stages of the MEDUSA program, and provided much useful macroscopic information on plasma shape, motion during the shot, and discharge initiation and termination locations. A photograph taken with the camera is shown in Figure 4-14.

Visible light (radiation) monitors are also in place on MEDUSA. These consist simply of a lens that focuses plasma light onto a fiber optic bundle, bandpass filters, and a photomultiplier for each filter. The radiation monitors are used to give estimates of plasma

Figure 4-14. Photograph of a MEDUSA plasma. The dark vertical bar to the left is a TF coil; the disc next to it is a side port. The thin dark bar is a part of the support structure. The large central bar is the inner wall. The horizontal lines are flux loops.

temperature. Each bandpass filter passes radiation from certain atomic transitions. In ionization equilibrium, the prevalent ionization state of each atomic species is a very strong function of electron temperature [7]. By observing the radiance of various spectral lines, therefore, a crude estimate of the electron temperature may be made. The filters available on MEDUSA are Hα (656 nm, IP ≈ 13 eV), OII (442 nm, IP ≈ 35 eV), CIII (466 nm, IP ≈ 50 eV), OVI (381 & 383 nm, IP ≈ 140 eV), and a visible bremsstrahlung filter (525 nm).

Electrostatic probes have been used to a limited extent in MEDUSA. A triple probe [8,9] was the primary diagnostic of this type. This type of probe works by inserting three probe tips into the plasma. One tip rests at the floating potential. The other two tips are biased differentially by a known voltage, which should be greater than 3 or 4 times the electron temperature. The negatively biased probe is assumed to be in ion saturation, and draws the ion saturation current

$$I_{is} = n_i e A \sqrt{\frac{eT_e}{m_i}} \tag{4-7}$$

where I_{is} is the ion saturation current and A is the effective area of the probe. The voltage difference between the "high" tip and the floating tip is approximately $T_e ln2$, which is approximately the slope of the plasma I-V characteristic at that point. Once the electron temperature is known, the ion density can then be inferred from equation 4-7. There are severe limitations to using this method in tokamaks, however. If the probe bias is not large enough, then it is likely that the estimate for T_e will be low and that the probe will not be in ion saturation. In MEDUSA it was found that electron temperatures up to about 30 eV could be measured, but that the probe could not reach a higher value of T_e. This is believed to be due to the limited bias available (120 V). After this bias was exceeded, the tips appeared to become emissive, rendering those measurements useless. However, the MEDUSA triple

probe did collect some useful information on edge conditions, and provided some idea of the qualitative behavior of the density in the core.

One of the key diagnostic instruments in the present work is the MEDUSA internal magnetic probe array. Figure 4-15 shows a schematic illustration of this diagnostic. The probe measures the major radial component of the plasma poloidal field (i.e., $\mathbf{B}\cdot\mathbf{e}_R$) at five separate spatial locations along a vertical chord at a major radius of 12 cm. The pickup coils themselves are manufactured by Microwave Components, Inc. (part number 15-30-40-CA); they consist of 15 turns of 40 AWG copper wire wound around a 0.76 mm diameter form. One of the leads is pulled through the center of the coil, and both leads are soldered to 32 AWG magnet wire. This pair of conductors is twisted (3 turns/cm) to minimize magnetic pickup. The coils are inserted into holes in a specially machined rectangular form, 2.5 mm by 2.1 mm by 16.1 cm long, made of delrin plastic. This form aligns the coils and guarantees precise positioning. The twisted pair signal cables are positioned in shallow grooves cut in two of the four sides of the form. The entire assembly is wrapped tightly in teflon tape to hold all of the parts in place. This piece is housed by a stainless steel tube sheath (304 SS, 37.5 cm long, 3.0 mm ID, 3.2 mm OD). The tube has one end silver-soldered shut and is a vacuum wall; the probe coil/delrin assembly itself is open to the atmosphere. The sheath is held in place by a Cajon vacuum fitting in the standard MEDUSA probe port (see Section 4.2). The signal cables are brought out of the sheath as twisted pairs, which run to the instrumentation rack. There the signal is amplified (by differential amps) by 100 times and then passed to the digitizers.

The probe array was calibrated with a small Helmholtz coil assembly, and later recalibrated by rotating the probe in the vacuum vessel while pulsing the toroidal field. The effective areas and poloidal angles (that is, deviation from purely major radial field, measured from the probe axis) are given in Table 4-3. The variations shown in Table 4-3,

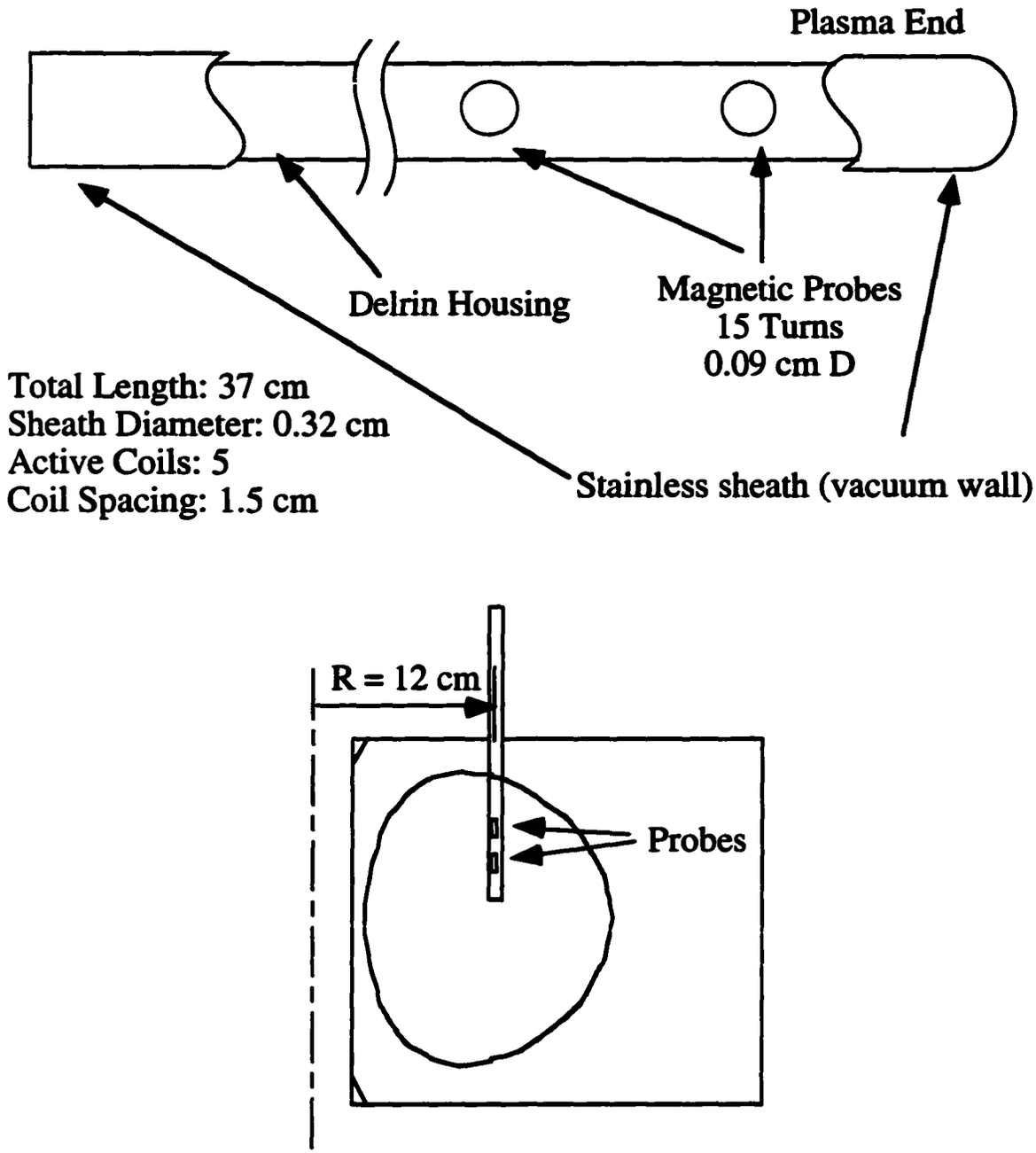

Figure 4-15. Top: Schematic drawing of MEDUSA internal magnetic probe array. Bottom: Probe location in plasma.

Coil Number	Effective Area (mm^2)	Effective Poloidal Angle (degrees)
2	6.7	4.5
3	7.2	-12.2
4	8.7	8.1
5	7.5	0.0 (Reference)
7	8.4	-18.0

Table 4-3. Effective areas and cylindrical poloidal angles of the magnetic probe coils.

particularly those of angle, are due to four identifiable causes. First, the process of pulling leads through the coils often would remove some number of weakly bonded turns, from zero to 1-1/2 turns. Second, the pulled-through lead may not be symmetric in the center of the coil, contributing another effective area to the coil parallel to the toroidal field. This effect alone can change the effective area by 0.8 square mm and the effective angle by 7 degrees. The third cause of these variations are open areas in the twisted pairs; these are made inevitable by the solder joints between the coils and the twisted pairs. Finally, there are likely to be some small misalignment of the coils in the form, although this effect should be small since the coils are relatively tight-fitting. These angles and areas are of course taken into account in the data analysis. However, these alignment issues are not as critical as they may seem. One point is that, since the signal depends on the cosine of the poloidal angle, small angular errors contribute only small errors. For example, a coil turned 20 degrees off of the major radial direction still sees 94% of the radial field. Another point to consider is

that the data from this probe is usually used as input to the equilibrium code; the code fits the equilibrium to the input data inside specified error bars, which makes high accuracy less of a priority. The error bars for the coil measurements are estimated to be well less than 20% of the reported signal.

4.9 Experiment Operation

Some data from a representative MEDUSA discharge are shown in Figure 4-16. Typical shots have a lifetime of 1-2 ms, with peak plasma current values between 15 and 40 kA. Average electron densities (inferred from fill gas pressures and triple probe measurements) are typically 2 - 5×10^{19} m^{-3}. Average electron temperatures (from impurity emission and triple probe measurements) are typically 50 eV.

A shot begins when the operator presses the "fire" button on the control computer interface. Immediately after this occurs, the gas valve is opened. In order for the gas pressure to stabilize to repeatable values from shot to shot, the gas fill continues for 1.9 seconds. The data acquisition trigger then occurs; this time is labelled t=2.05 ms for reasons internal to the DAS. The first TF bank is then fired at t=3.55 ms, and the toroidal field ramps up to its steady-state value, usually 0.3 Tesla. The second banks are then fired at t=6.95 ms and subsequent 1 ms intervals.

To help initiate the discharge, two complementary preionization (PI) techniques are used. The first PI tool is a bank of tungsten filaments located in the gas puff port. This bank provides free electrons in the vacuum vessel directly by thermionic emission, and indirectly by ionization of bulk fill gas atoms by radiated UV. The electric current to the filaments is turned off in the few milliseconds bracketing the shot; this is done to prevent electromechanical forces from destroying the bank. The free electrons created by the filaments are then used by the second PI technique, electron cyclotron resonance (ECR)

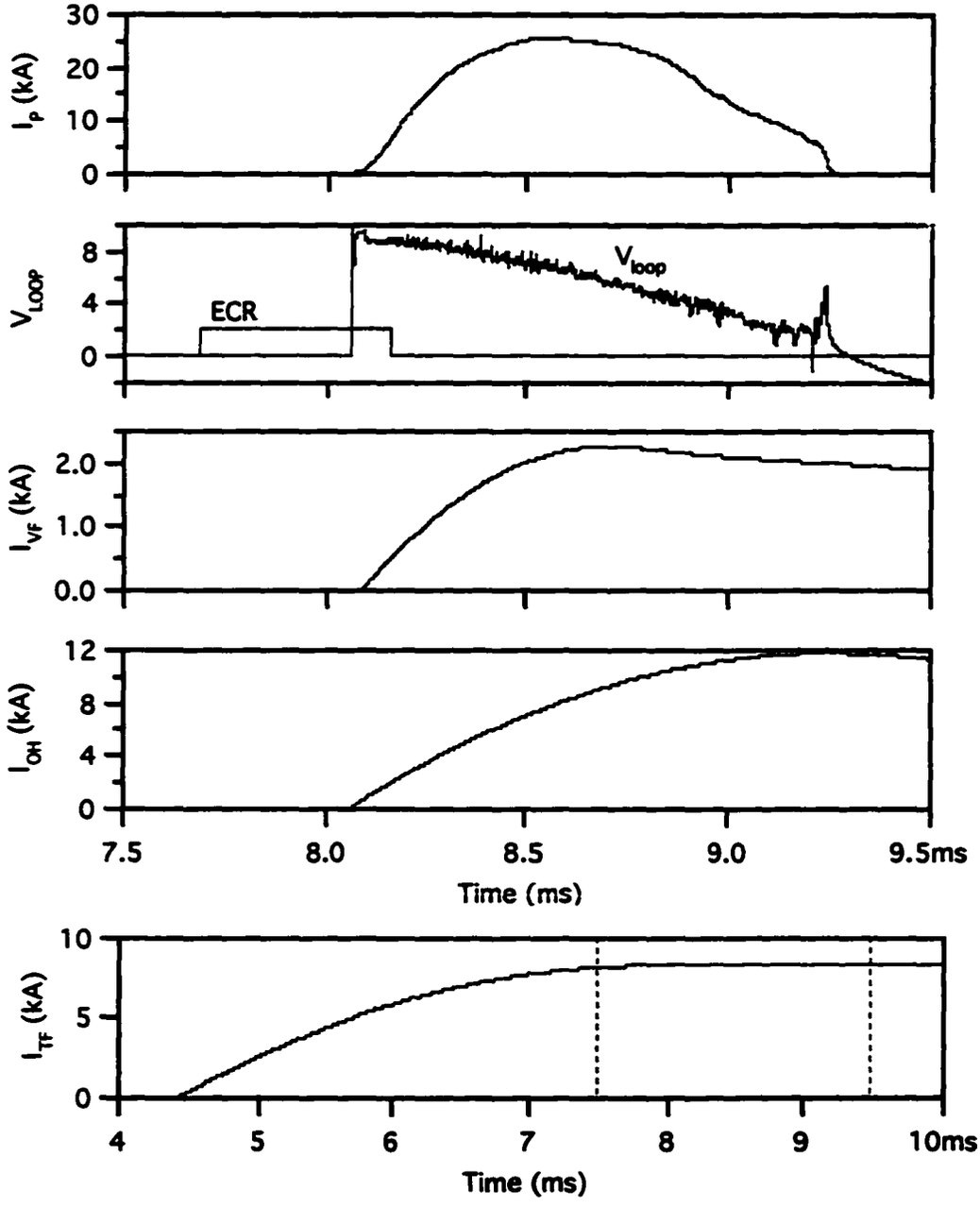

Figure 4-16. Data from a representative MEDUSA shot. From top to bottom: Plasma current, loop voltage and ECR timing, VF current, OH current, and TF current (note change in time scale; dashed lines indicate time window of other graphs.)

preionization. In this technique, microwaves are launched into the vacuum vessel and interact with free electrons at the electron cyclotron resonance. The electrons gain energy and ionize the bulk fill gas, creating a low-density (by tokamak standards) plasma; as the plasma density increases, the microwave absorption moves to the upper hybrid resonance [10]. In MEDUSA, the ECR frequency is 5.5 GHz, which puts the electron cyclotron resonance at 18 cm major radius for a 0.3 Tesla toroidal field. The nominal input power at the source is 70 kW, and the pulse length is 560 microseconds. The microwave radiation is transmitted from the source through standard waveguides, and is launched into the vacuum by a microwave horn located immediately outside the vessel. The horn is oriented for O-mode launch, which has been found to work more effectively than X-mode for preionization [11]. The pulse is usually initiated at t=7.60 ms, 460 microseconds before the loop voltage is applied; this gives a 100 microsecond overlap between the two.

The first OH bank is fired at t=8.06 ms, generating a loop voltage between 5 and 10 volts. The first VF bank is fired soon after, usually at t=8.095 ms. Subsequent OH and VF banks are fired at less fixed times; they are usually set to match desired experimental goals. The plasma forms almost immediately after the OH is applied, and the current ramps up as the VF current is initiated. The plasma current generally peaks between t=8.4 ms to t=8.8 ms, and then decays. Since the L/R time of the VF system is much longer than the plasma lifetime, the discharge ends as the plasma is pushed into the center column (as verified by photographs and reconstructed equilibria.)

The shot cycle is set to 5 minutes in length. This allows the conductors, particularly the OH solenoid, to cool to room temperature before the next shot. This also allows a brief period of time to retrieve the shot data from the digitizers and to give it a brief first look. Usually once or twice per run day a getter cycle is performed, although this is not a set procedure.

4.10 References

1. SYKES, A., et al., Nucl. Fusion **32** (1992) 694.

2. GRYAZNEVICH, M., AEA FUS 242, UKAEA/Euratom Fusion Association (1993).

3. SHACKLEFORD, J.F., *Introduction to Materials Science for Engineers*, Macmillan Publishing Company, New York, 1988.

4. GARSTKA, G.D., et al., Bull. Am. Phys. Soc. **38** (1993) 2007.

5. GARSTKA, G.D., et al., Bull. Am. Phys. Soc. **39** (1994) 1574.

6. STACEY, W.M., *Fusion: An Introduction to the Physics and Technology of Magnetic Confinement Fusion*, John Wiley & Sons, New York, 1984.

7. HUTCHINSON, I.H., *Principles of Plasma Diagnostics*, Cambridge University Press, Cambridge, 1987.

8. CHEN, S-L., and SEKIGUCHI, T., J. Appl. Phys. **36** (1965) 2363.

9. DIEBOLD, D., WANG, E.Y., et al., Rev. Sci. Instrum. **61** (1990) 2870.

10. GILGENBACH, R.M., ENGLAND, A.C., et al., Nucl Fusion **21** (1981) 319.

11. WHALEY, D.R., GOODMAN, T.P., POCHELON, A., et al., Nucl. Fusion **32** (1992) 757.

5. Equilibrium and Flux Consumption on MEDUSA

This chapter details the general behavior of MEDUSA plasmas and the results of the flux consumption analysis of several types of discharges. It begins with a description of typical MEDUSA equilibria, including shot phenomenology such as plasma current, temperature and density. Data from the internal magnetic probe array are presented and discussed in detail. The results from the flux consumption analysis are then presented. Trends in the results are identified and discussed. Chapter 6 will continue the discussion with an analysis of current penetration, particularly in the presence of double tearing modes.

5.1 MEDUSA Equilibria

Much of the analysis of MEDUSA plasmas is done with the Tokamac 2.0 code, which numerically solves the Grad-Shafranov MHD equilibrium equation (discussed in Chapter 2) subject to the constraints of real measurements. On MEDUSA, this data consists of magnetics measurements. For this work, twelve measured quantities were used to constrain each equilibrium "time slice." These quantities were: plasma current, VF current, five flux loops from around the vacuum vessel (LV1, FT1, FB1, FB2, FB3), and the five internal magnetic probe measurements. Sample equilibrium data are given in Table 5-1 and Figure 5-1. Table 5-1 gives a comparison between the measured input values and the fitted output values for shot 14111 at 8.6 ms. Most of the results show good agreement with the measured values. The primary exceptions are the three inner flux loops (LV, FT1, FB1), which represent small fractions of the measured signals; these differences are due to effects such as perturbations in the OH system current during plasma shots, eddy currents in the inner wall, and inaccuracies in the coil positioning.

Figure 5-1 contains graphs of several equilibrium parameters. At the top of the figure

Quantity	Measured	Fit	Deviation (%)
Currents			
I_p (kA)	18.0	16.0	-11
I_{VF} (kA)	1.4	1.5	+7
Flux Loops			
LV (mV-s) R=0.03, Z=0	-0.2	-0.11	-45
FT1 (mV-s) R=0.066, Z=0.142	0.024	0.013	-46
FB1 (mV-s) R=0.066, Z=-0.148	0.023	0.034	+48
FB2 (mV-s) R=0.184, Z=-0.148	1.6	1.4	-12
FB3 (mV-s) R=0.31, Z=0.148	6.6	7.7	+17
Internal Probes			
MP2 (Gauss) R=0.12, Z=0.019	71	83	+17
MP3 (Gauss) R=0.12, Z=0.034	150	150	<7
MP4 (Gauss) R=0.12, Z=0.049	210	200	-5
MP5 (Gauss) R=0.12, Z=0.064	240	240	<5
MP7 (Gauss) R=0.12, Z=0.094	240	260	+8

Table 5-1. Equilibrium fit results for shot 14111, time 8.6 ms.

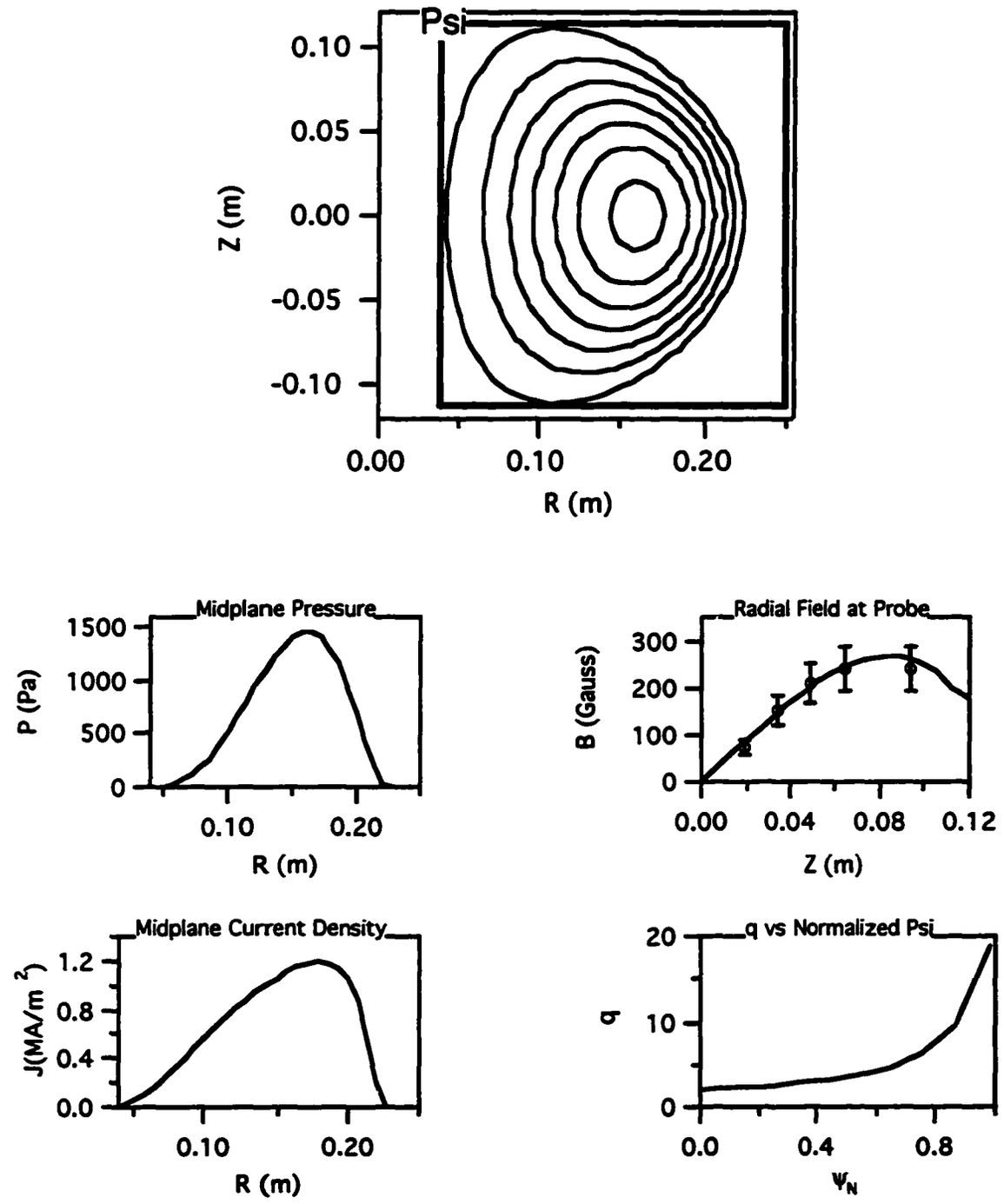

Figure 5-1. Typical MEDUSA equilibrium data from shot 14111, time 8.6 ms (near peak current.) Additional equilibrium parameters: I_p=16.0 kA, R_0=0.132 m, a=0.095 m, ℓ_i=1.00, κ=1.12, β_N=2.36, β_p=1.18.

is a plot of poloidal flux contours. Middle left is a plot of pressure versus major radius at the midplane, while bottom left is a graph of current density at the midplane. Middle right is a plot of the measured (data points) and fitted (solid line) value of the radial field at the magnetic probe. Finally, the plot at bottom right gives the value of q versus normalized psi (ψ_N), where ψ_N is defined as

$$\psi_N \equiv \frac{\psi - \psi_0}{\psi_a - \psi_0} \tag{5-1}$$

and the a and 0 subscripts indicate the plasma edge and center, respectively.

Since much of the analysis presented here depends on the magnetic probe constraints on the equilibrium equation, it is desirable to determine the sensitivity of the equilibria to errors in the probe signals. A Monte Carlo analysis was performed to determine the effects of random errors in these measurements. Most of the error in these measurements is systematic. It stems from sources such as angular misalignment of the probe and open pickup areas in the leads. These errors will appear consistently from shot to shot and will not affect the overall analysis. The effects of random errors are more significant to cross-comparison between discharges. Random errors can be caused by amplifier noise, capacitive pickup, and coupling to capacitor bank noise. The 98% confidence limits in the probe measurements are taken to be 20% of the signals. These error bars are due mostly to the systematic errors, and hence are overestimates for random errors. Nevertheless, the Monte Carlo analysis used ±20% as the 98% limits for error generation.

The Monte Carlo analysis proceeded as follows. One time slice was chosen for the study. This time slice is the same as given in Table 5-1 and Figure 5-1, shot 14111 at 8.6 ms. The original values for the probe signals were called the "base case," or case 0. An equilibrium was generated from these measurements and the other input measurements.

Then, ten additional cases were produced by randomly varying the probe measurements in a Gaussian distribution centered at the base case with the predetermined error bars. Each measurement was varied independently of every other measurement. Equilibria were then generated for each of these cases. Some of the results of these equilibria are given in Table 5-2. Included in this Table are the probe measurements, plasma current, internal inductance, total beta, and the value of χ^2 for each case. (The goodness-of-fit parameter χ^2 is defined as

$$\chi^2 = \sum \left[\frac{(a_{fit} - a_{meas})}{\Delta a} \right]^2$$

where a is a measurement, the subscripts "meas" and "fit" refer to the measured input value and the fitted output value, respectively, Δa is the uncertainty in the measurement, and the summation is over all of the measurements.) The results from this analysis reveal that the characteristics of the equilibrium are not significantly changed by random errors in the probe measurements. The plasma current varies by only ± 2.5%, while beta varies by ±0.08%. The variation in the internal inductance is ±0.05, which is used in the estimates of error in the flux consumption calculations. Finally, only one of the error cases (#8) produced a smaller value of χ^2 than case 0; case 8, which is close to the base case, had a marginally smaller value of χ^2 (3.79 vs 4.06). All of the other cases produced larger values of χ^2, indicating that the base case is close to the best-fit answer.

Typical MEDUSA plasmas attain maximum currents between 10 and 40 kA, and last between 1 to 2 ms in duration. Figure 5-2 shows a set of equilibrium results for a representative shot; this figure gives the plasma current, major radii, internal inductance, actual β and β_N, and q_0 and q_{98} calculated for this discharge. (The two major radii are the

Case	MP2	MP3	MP4	MP5	MP7	I_p	ℓ_i	β	χ^2
0	71	150	210	240	240	16.0	1.00	1.46	4.06
1	60	140	230	220	240	16.0	0.95	1.45	5.68
2	59	160	200	270	230	16.1	0.97	1.46	6.47
3	74	150	240	240	240	16.0	1.03	1.44	4.74
4	82	140	190	230	200	15.7	1.03	1.38	4.89
5	64	140	220	240	190	15.7	0.98	1.38	6.66
6	73	150	200	220	210	15.7	1.00	1.39	4.76
7	61	160	210	270	230	16.0	0.98	1.47	6.31
8	79	160	200	240	240	16.0	1.04	1.44	3.79
9	67	150	230	260	290	16.4	0.99	1.53	5.15
10	73	160	230	230	230	15.9	1.03	1.43	4.95

Table 5-2. Results of Monte Carlo analysis of shot 14111 at 8.6 ms. Units: magnetic probes: Gauss; plasma current: kA; beta: percent. Case 0 is the baseline. Results for χ^2 do not include the three inner fluix loops (LV, FT1, FB1).

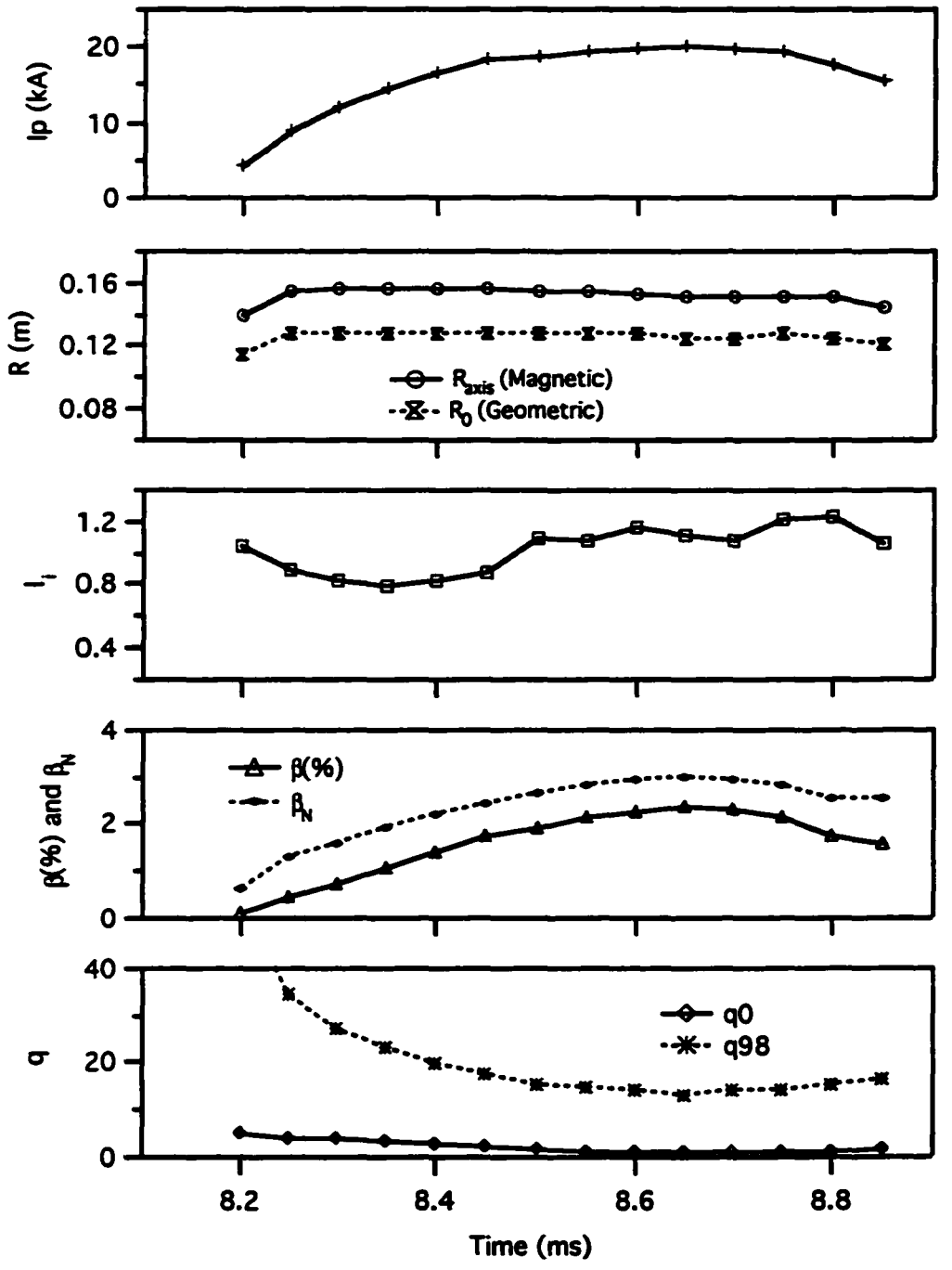

Figure 5-2. Equilibrium code output for startup of shot 14060. From top to bottom: plasma current, major radius and magnetic axis, internal inductance, total beta and beta normal, and q_0 and q_{98}.

magnetic axis, which is the point where $\nabla\psi=0$, and the geometric axis, which is the midpoint between the inner and outer edges of the plasma.) Typically the plasma is initiated at a geometric major radius ($R_0 \equiv R_{outer} - R_{inner}$) of 9 - 11 cm, and rapidly grows outward in the first 100 μs. The major radius normally grows to 12 - 13 cm, and the magnetic axis grows to 15 - 16 cm. These radii then tend to slowly decrease during the remainder of the discharge. The value of q_0 generally reaches a minimum of 1 - 2 near the current peak. Average current densities can be as high as 1 MA/m^2. Beta increases throughout the current ramp. Values of β_N have been found approaching 3.5, and β_p typically is near 1 to 1.2, giving values of $\varepsilon\beta_p$ of approximately 0.6-0.9. Core pressures can reach as high as 4 kPa, but are typically closer to 2 kPa.

These pressures are confirmed by isolated independent measurements from both the triple probe and visible light monitors. Visible light data shows that H_α, OII, and CIII reach burnout, while OVI clearly does not (although the OVI measurement may be dominated by background light). This indicates that the temperature of a large fraction of the plasma is between 50 and 140 eV. Sample visible radiation data is given in Figure 5-3. This figure gives the plasma current, H_α, CIII, and OVI signals for shot 4786. These data clearly show burnout in the H_α and CIII signals, while this is not observed in the noisier OVI signal.

The triple probe, as discussed in Chapter 4, had severe limitations in MEDUSA. However, the probe data can give some indication of the temperature and density profiles. The temperature measurement is found to saturate around 20-30 eV at a short distance in from the edge. This saturation is due to limitations in the biasing power supply. As discussed in Chapter 4, the bias in a triple probe must be much greater than the temperature

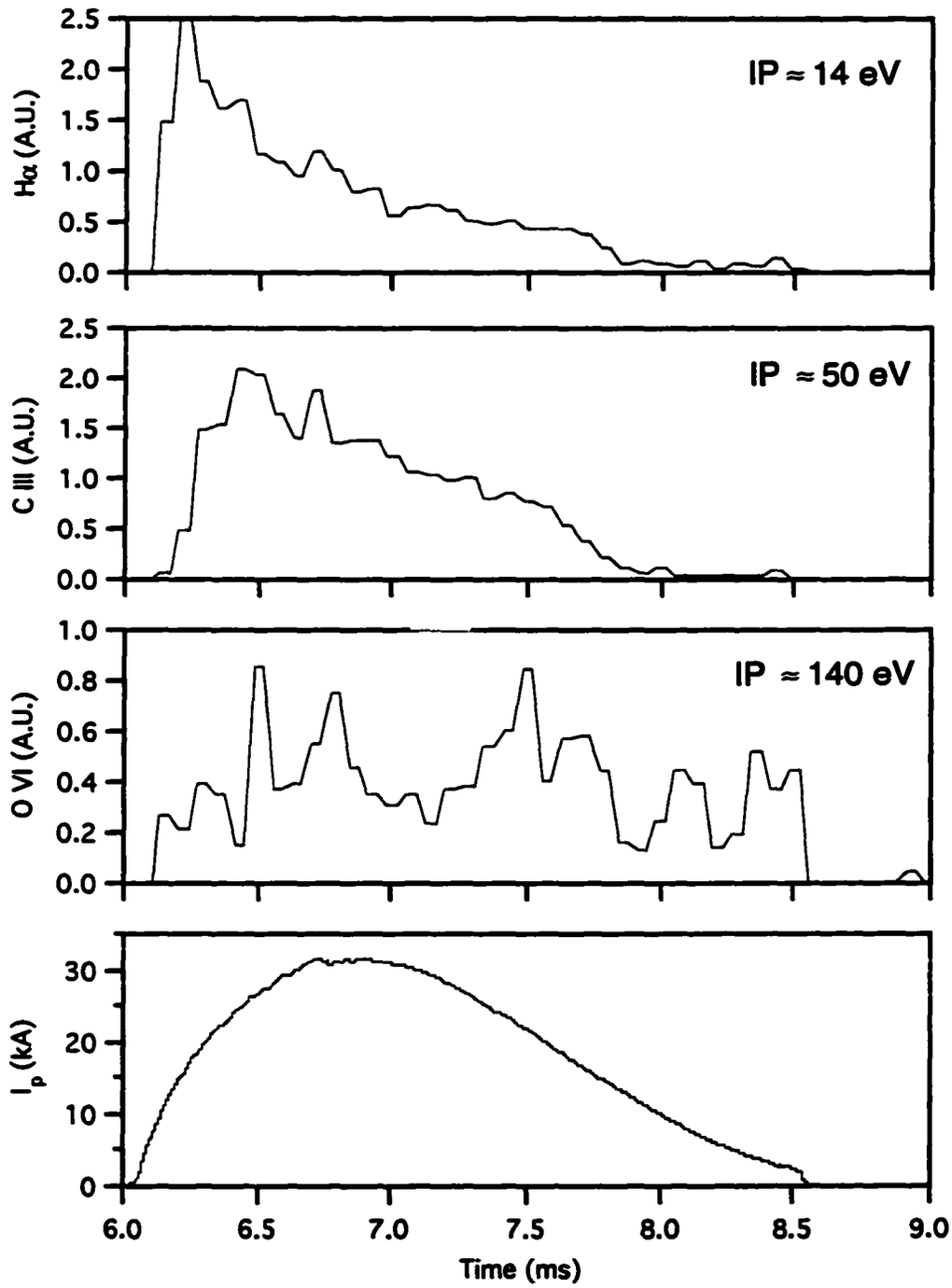

Figure 5-3. Sample visible radiation data from shot 4786.
IP is the ionization potential.

being measured, or the measurement will saturate. The bias could unfortunately not be raised, as the probe tips began arcing together above 120 V. Meanwhile, the density data shows a strong peaking toward the plasma center, with "core" (R=12 cm, Z=0) electron densities often exceeding 10^{20} m^{-3}. This measurement is somewhat inaccurate, since the triple probe density calculation depends on the temperature measurement (as $T_e^{-1/2}$); this effect would cause a density over-measurement of a factor of 2 in the core. Further complicating this picture is the effect of "flux tube depletion," which is due to the slow rate of cross-field particle diffusion in tokamaks relative to transport on a flux surface; this will result in a reduced density measurement. Core densities approaching 10^{20} m^{-3} therefore do not seem unreasonable.

Macroscopic considerations can also help determine average temperatures and densities. The fill gas pressure can be used to estimate the average plasma density. Hydrogen is puffed into MEDUSA at a pressure of approximately 0.24 mtorr, which represents an atom density of 1.5×10^{19} m^{-3}. The volume of the plasma is roughly 0.022 m^3, while the volume of the vacuum vessel is roughly 0.08 m^3, giving a vessel/plasma volume ratio of about 4. The plasma is an effective pump on the fill gas; the plasma density should therefore be increased roughly by the volume ratio. This results in an average density of 6×10^{19} m^{-3}; if a linear density profile is assumed, the resultant core density is 1.8×10^{20} m^{-3}. The effects of wall recycling, fill gas ionization, and particle transport will of course affect this estimate.

The average temperature can likewise be estimated by considering the plasma current and loop voltage when the plasma current and inductance are constant. Ohm's law gives the plasma resistance, which can then be used to calculate a "resistivity temperature." Taking for example the data for shot 14060 in Figure 5-2, one observes that the plasma current and

inductance are approximately constant at 8.7 ms. At this point in time the loop voltage is approximately 6 volts and the plasma current is 19.7 kA. Ohm's law gives an average resistance of 3.0×10^{-4} ohms. The central temperature can be back-calculated using Spitzer resistivity. Taking $Z_{eff}=4$, $\ln\Lambda=15$, and a parabolic temperature profile of the form

$$T(r)=T_0\left(1-\frac{r^2}{a^2}\right) \qquad (5\text{-}2)$$

where a is the minor radius, the peak temperature T_0 is calculated to be 85 eV.

The results from the preceding sets of calculations support the pressure values output by the equilibrium code. The central electron density is estimated from gas fill arguments to be 1.8×10^{20} m^{-3}; the results from the triple probe give central electron densities around 10^{20} m^{-3}. Meanwhile, the central temperature is estimated to be between 50 and 140 eV from visible light measurements, and approximately 85 eV from the resistivity argument. Canonically, then, the measured electron density and temperature in MEDUSA are 1.5×10^{20} m^{-3} and 100 eV, respectively. These results give a central electron pressure of 2400 Pa, which is in good agreement with the equilibrium code output values of 2000-4000 Pa.

The raw data from the internal magnetic probe array deserves some discussion. The probe, as described in the previous chapter, has 5 pickup coils arranged to measure the major radial component of the poloidal field. As implied earlier, these probes provide a constraint on both the current density, $J(R,Z)$, and the pressure, $p(\psi)$. For most of this study, the probes were located at a major radius of 12 cm and the following heights relative to the geometric center of the vacuum chamber: probe 2, 1.9 cm; probe 3, 3.4 cm; probe 4, 4.9 cm; probe 5, 6.4 cm; probe 7, 9.4 cm. The analysis of the probe data was conducted as follows. The raw signals were differentially amplified by 100 and then digitized (raw

voltages were on the order of 1 mV or less.) The digitized signals were then corrected for background effects. Each shot to be analyzed was accompanied by a "vacuum shot," which was identical to the "plasma shot" except that fill gas was not introduced. The background shot signals were subtracted from the plasma signals, correcting for pickup of vacuum fields by uncompensated dipoles in the probe transmission lines, and for the pickup of the toroidal field by the open area around each probe's leads. The background signals can be quite significant when compared to the plasma signals. In probe 5, the background signal is roughly 25% of the plasma signal; in probe 7, which has the worst alignment, the background signal is more than twice as large as the plasma signal, and is mostly due to pickup of the toroidal field. Equilibrium analyses show that plasma paramagnetism and diamagnetism, while present, are quite small; they generally only contribute a few Gauss to the total toroidal field on axis and hence do not strongly affect the probe signals. The lack of paramagnetism in MEDUSA is due to the relatively large value of β_p, which has a diamagnetic effect.

One of the original concerns with using the internal probe array was that the probe would seriously degrade the plasma performance. This concern was found to be overstated. The probe did decrease the plasma performance somewhat—comparisons of identical shots with the probe inserted and withdrawn show about a 10% decrease in plasma current and a 10-20% decrease in shot length with the probe inserted. The plasma behavior, however, did not appear to be qualitatively changed. Double tearing modes (discussed in Chapter 6) are still observed at approximately the same times in the discharge, and the initial plasma ramp rates are almost identical. The decrease in performance with the probe is likely attributable to impurities sputtered off of the stainless steel probe casing.

Magnetic probe data for a typical shot (14060) are given in Figures 5-4 and 5-5; Figure 5-4 contains plots of each probe's signal, while Figure 5-5 is a 3-D plot showing the

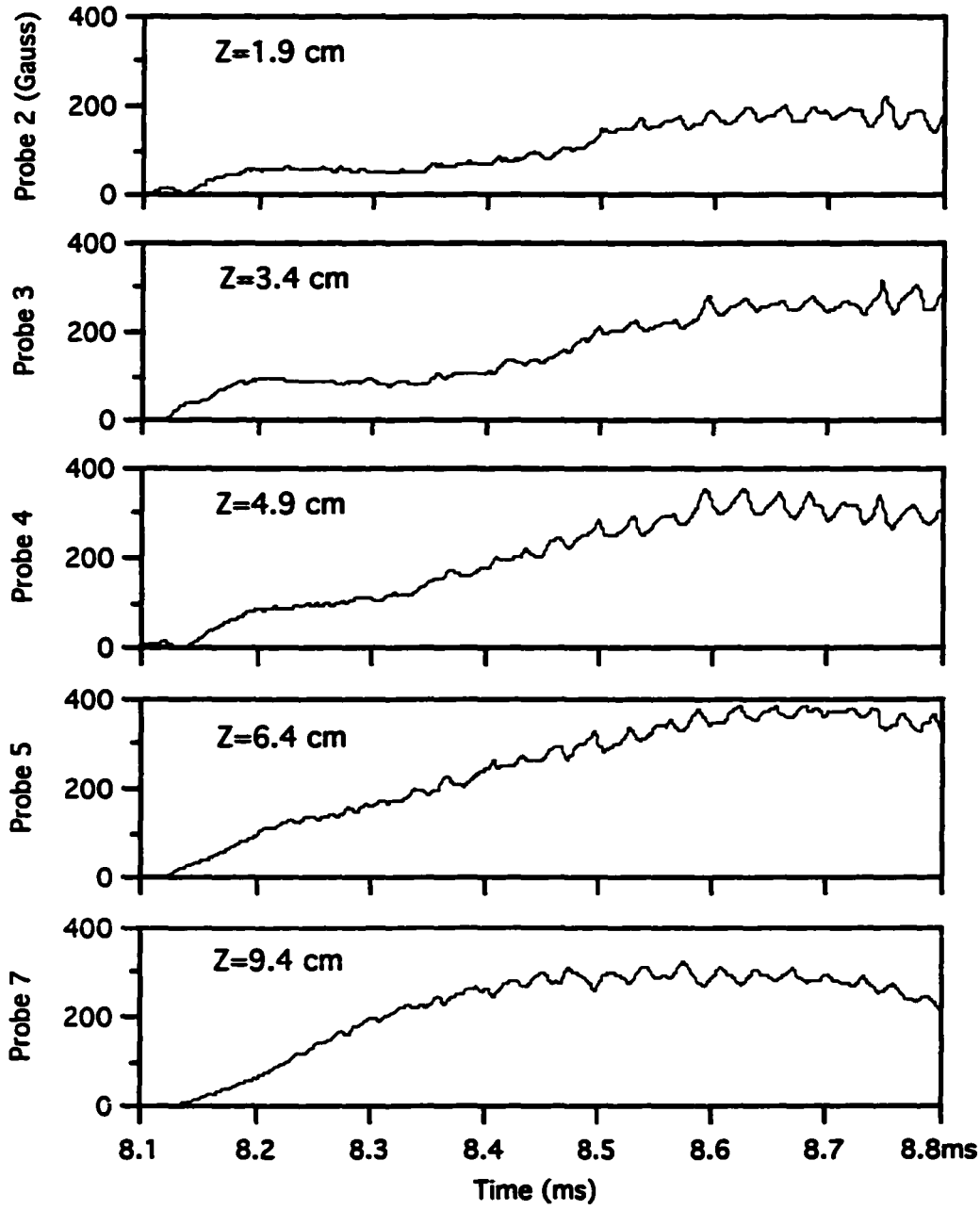

Figure 5-4. Plots of raw probe data for shot 14060.

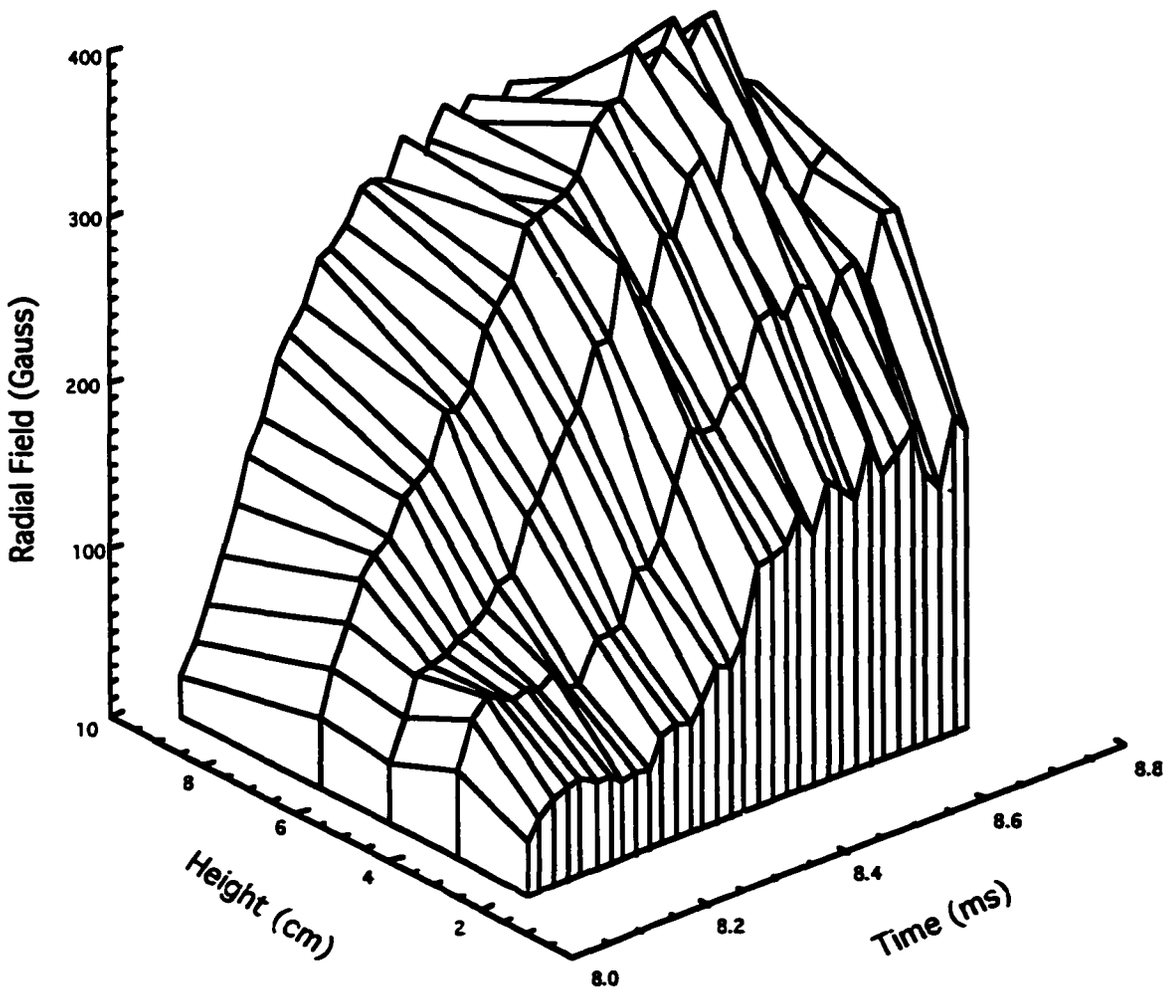

Figure 5-5. Three-dimensional plot of magnetic probe data from shot 14060.

internal field evolution. There are several features worthy of note in these figures, which are quite representative of the set of discharges analyzed. Typically, the outermost probe (7) shows the quickest rise in signal at the beginning of the discharge. This probe is often near the plasma edge, and is sometimes outside the last closed flux surface. Probe 5 usually comes up somewhat more slowly than probe 7. Further into the core, a "plateauing" effect can be observed. All of the probes show an abrupt rise to 50-100 Gauss in the first few tens of microseconds of the discharge. After this, though, the inner probe signals level off. The deeper into the core the measurement is taken, the more pronounced is the plateauing. Eventually each of the probe signals begin to rise again, with this rise occurring later for the deeper core measurements. This plateauing is an indication of the broadness of the current profile, which is strongly correlated with the internal inductance ℓ_i.

As the shot progresses, the probe signals begin to show an irregular fluctuating component on top of the longer time-scale signals. This fluctuating component can represent a substantial fraction of the "DC" signal, at the level of 10 to 20 percent for the outer probes and 40-50 percent for the innermost probe. The fluctuations begin earliest on the outermost probe, and occur later as the probes are closer to the core. They are present when q_0 is well above 1, making them unlikely to be sawteeth. As discussed in the next chapter, these fluctuations appear to be associated with double tearing modes. There is a definite phase relationship between the probe signals, and the fluctuations are positively correlated with perturbations in the loop voltage measurement.

5.2 Flux Consumption - Constant B_T, Variable Voltage Waveform

This section presents the results of the first of two sets of operation campaigns to collect flux consumption data. The method used to obtain the flux consumption data is discussed. The discharge types studied in the first run campaign are described. The results

of the analysis for the various discharges are presented and discussed.

The flux consumption analysis was conducted as follows. The shot data was processed into magnetics measurements that could be entered into the equilibrium code. For example, the flux loop data was zeroed and integrated to give measurements in volt-seconds. The magnetic probe data was smoothed with a 50 microsecond window in order to remove some of the effects of the strong fluctuations on the equilibrium fits. Time slices of this data were taken at 50 microsecond intervals throughout the startup period. These data sets were then input into the equilibrium fitting code (TokaMac 2.0), and equilibria were found at each 50 μs interval. The equilibrium code produces almost all of the necessary information for the flux consumption analysis, as discussed in Chapter 3. The equilibrium data for each shot, along with the input flux calculated from the OH and VF coil currents, were then put together into a second processing code. This code solved the integral equations for the flux consumption on the 50 μs intervals. At each time step the various flux components were calculated, and an Ejima coefficient calculated. Figure 5-6 shows the results of this analysis for shot 14060.

The Ejima coefficient is defined in Chapter 3 as:

$$C_E = \frac{1}{\mu_0 R_0 I_p}\left(\Phi_{in} - \Phi_{ext} - \Phi_{int}^{ind}\right). \tag{5-3}$$

There is an ambiguity with this definition. The issue is the time at which C_E is evaluated. As stated in Chapter 3, for this thesis the Ejima coefficient is evaluated at the point when the plasma current is at its maximum value. There are other definitions that are useful, though.

One coefficient, C_{90}, is evaluated when the plasma current reaches 90% of its maximum. This coefficient can provide a fairer comparison of dissimilar discharges. As an

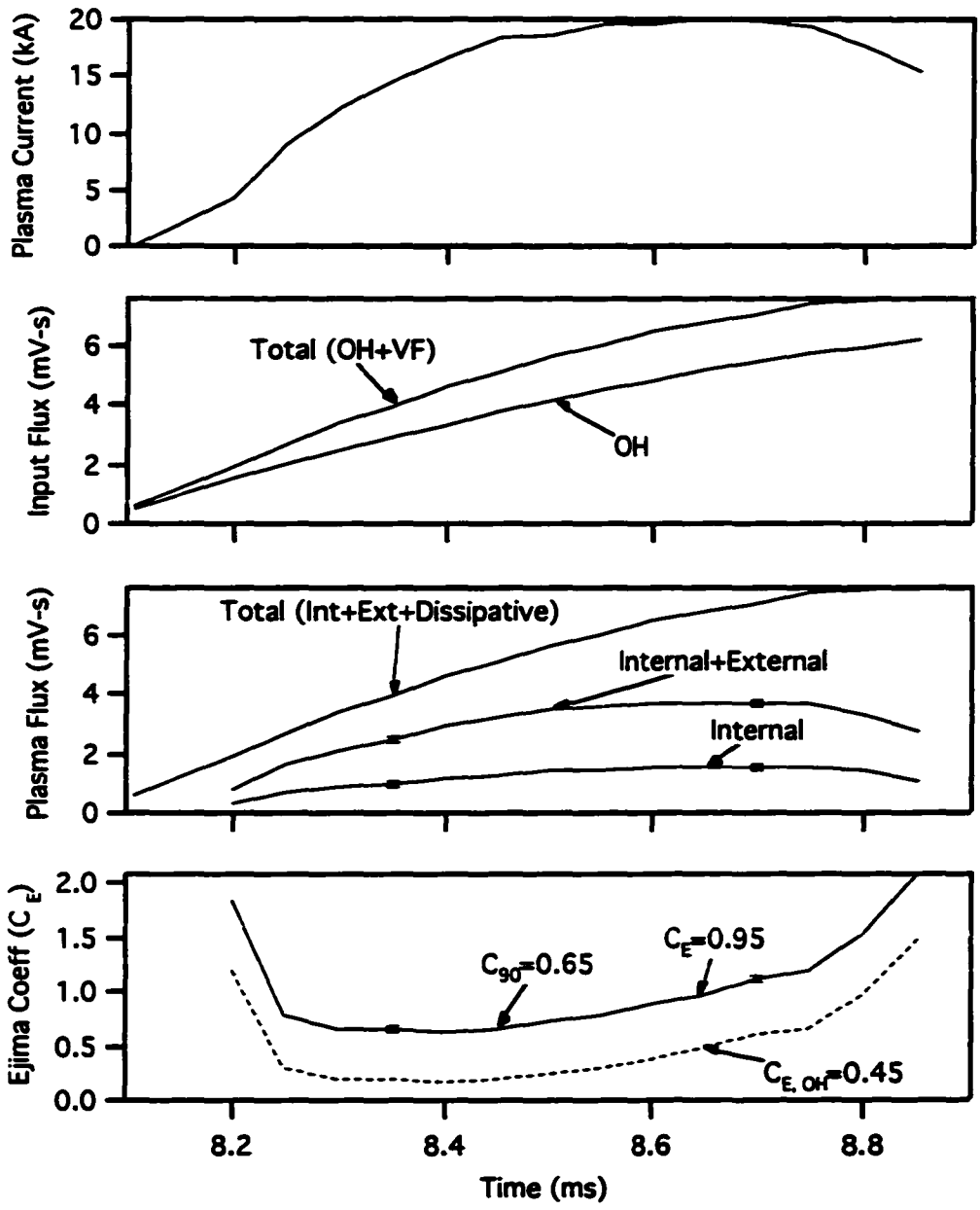

Figure 5-6. An example of flux consumption analysis from shot 14060.

example, consider two shots—one shot has a maximum in plasma current late in the discharge after a long "flat-top," while the other peaks early in time and decays into a flat-top. The C_{90} coefficient helps eliminate the ambiguities caused by changes in the time of the current peak.

Another Ejima-like coefficient useful for discussing startup in spherical tokamaks is C_{OH}. This coefficient is evaluated similarly to the Ejima coefficient, except that the input flux from the vertical field system is ignored. The coefficient is evaluated at the same time as C_E. (One can imagine $C_{OH,90}$, but this seems excessive.) This coefficient has utility as a figure of merit in spherical tokamaks due to the small amount of ohmic flux available.

A final quantity of interest, which will be called "FC" for wont of a better term, is the ratio of maximum plasma current to input flux. This can be defined for the total input flux, or solely for the ohmic flux. This figure of merit is often useful as a first analysis of performance, since it can be evaluated with unprocessed experimental data. This quantity is not as useful as the Ejima coefficient, though, as it does not take some important details of the plasma, such as geometry and ℓ_i, into account

Two separate operational campaigns were conducted to collect flux consumption data. The first campaign yielded three different kinds of shots for analysis. The shots discussed in this section are numbers 13493, 13521, and 13587, each of which is representative of tens of similar discharges. All of these discharges were conducted at 0.3 T at 0.12 m major radius. Shot 13493 had a maximum current of 17 kA, and peaked relatively early in time at 8.4 ms. Shot 13521 had an initial current ramp similar to that of 13493, but managed to obtain a higher ultimate current of 22 kA at 8.55 ms. Shot 13587 was conducted with a double current ramp. The initial ramp took the plasma current to 13 kA, and the second ramp led to a 21 kA maximum current at 8.75 ms. The plasma current and loop voltage waveforms for these three shots are given in Figure 5-7, along with the derived

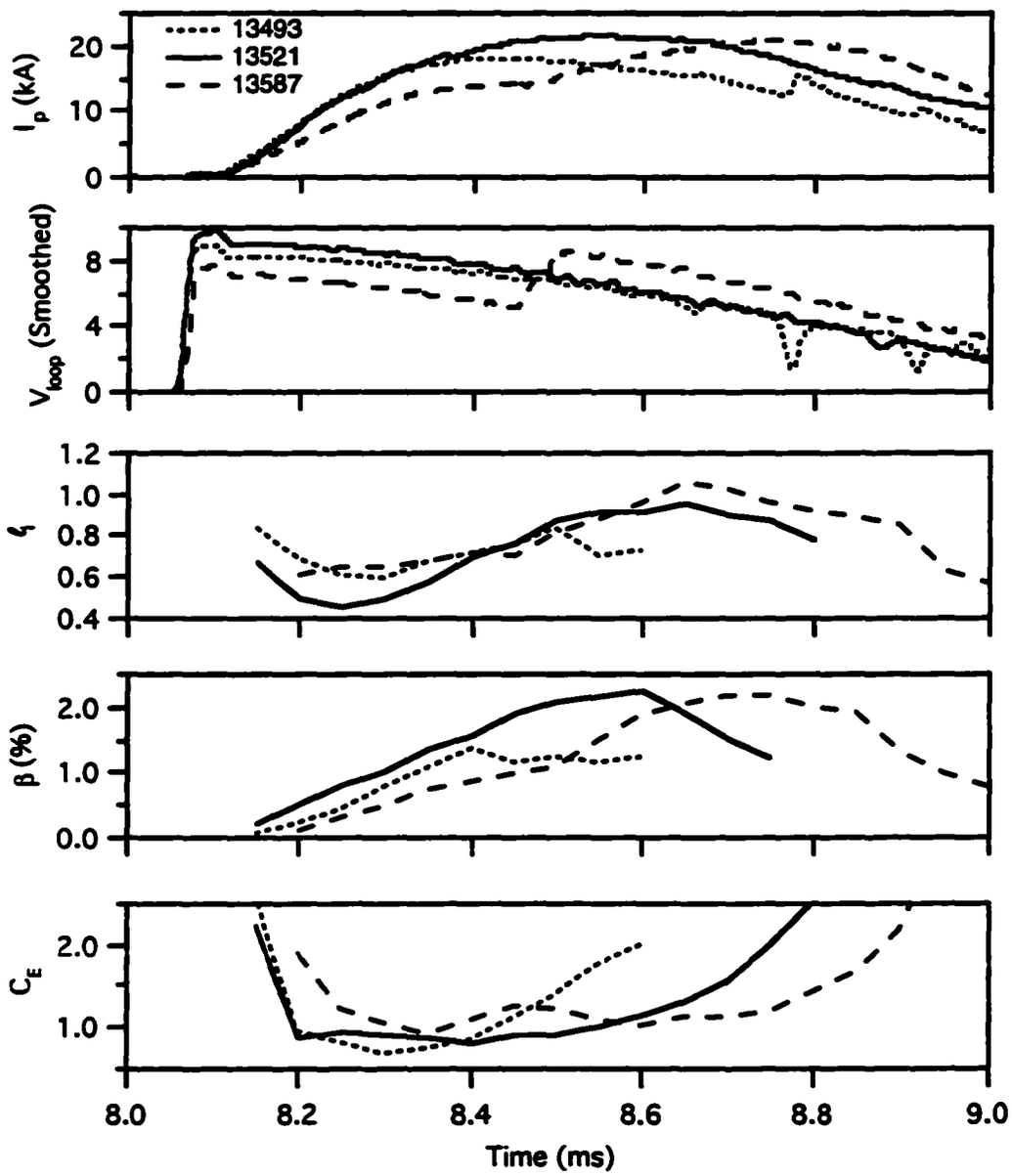

Figure 5-7. Plasma current and loop voltage data for first set of shots. The spikes late in time of 13493 are IREs.

quantities ℓ_i, β, and C_E.

The flux consumption results for these shots are given in Table 5-3. Shot 13493 appears to have the best flux consumption in every figure of merit, while the comparison between 13521 and 13587 is not as clear. The result for shot 13493 is confusing; this shot is certainly the poorest of the three by most measures. It is shorter, has less current, and has a lower value of beta than the other two shots in this campaign.

This difficulty can be addressed by considering some details of the evolution of these shots. Especially helpful is the comparison between 13493 and 13521, since these two discharges are fairly similar. The data in Figure 5-7 show that shot 13493 has a value of ℓ_i somewhat higher than that of 13521 during the current ramp. This means that the plasma in shot 13493 has more internal flux than that of 13521 for the same plasma current (provided that the plasmas are the same size, which they are). Further, shot 13493 obtains its performance with less input flux than 13521, which necessarily implies improved use of the available flux. Another important factor is that the plasma current in shot 13493 peaks early in time relative to that of 13521. This early peaking improves the reported flux consumption

SHOT	C_E	C_{90}	C_{OH}	FC (kA/mV-s) (Total | OH)
13493 Shorter ramp 17 kA, 0.3 T	0.85	0.74	0.34	3.6 | 5.0
13521 Longer ramp 22 kA, 0.3 T	1.15	0.89	0.64	3.0 | 4.0
13587 Double ramp 21 kA, 0.3 T	1.10	1.01	0.60	2.9 | 3.8

Table 5-3. Flux consumption results for constant B_T , variable V_l shots.

results. Figure 5-7 indicates that these two discharges have approximately the same value of C_E at the instant when 13493 peaks. Finally, shot 13521 has a significantly higher value of beta than 13493. This difference is especially notable after the current peak in 13493, when the β for shot 13493 levels off at 1.4%, while β for shot 13521 continues to increase to 2.2%. This increased beta implies that much of the dissipative flux was consumed in plasma heating.

The conclusion to be drawn from the previous paragraph is the limited utility of the flux consumption figures of merit. They can be useful for describing similar shots, but they must be discussed in the context of the discharges (or discharge scenarios) under consideration. An important point to consider is that the Ejima method of flux consumption analysis ignores plasma heating, treating it as a dissipative loss. (Plasma heating is considered indirectly, in that it lowers the plasma resistivity.) This is not necessarily a shortcoming, as a higher current plasma with low beta may be more desirable in some cases than a lower current, higher beta plasma.

The double ramp shot, 13587, was run in an attempt to obtain a longer, higher-current discharge than would be possible with a single current ramp. The reasoning behind this attempt was that the initial voltage pulse would establish and heat a base plasma. The second pulse would increase the plasma current further and more efficiently, since the volt-seconds of the second pulse would be expended when the plasma was less resistive than in the single-ramp cases.

One counterintuitive result of this shot was that the current profile did not broaden during the second current ramp, as might be expected by current diffusion arguments. In fact, the data in Figure 5-7 show that the current profile in shot 13587 becomes more peaked (i.e. ℓ_i increases) when the second voltage pulse is applied. Concurrent with current profile

steepening is a dramatic increase in beta, which more than doubles in the 200 μs of the second ramp. The flux consumption results, meanwhile, are comparable to those of the single-ramp shot 13521 (see Table 5-3). The fact that the flux consumption results did not improve over the single-ramp scenario can be attributed to increased dissipative losses in the cold base plasma.

The startup data for 13587 are difficult to interpret in terms of the physical picture of current diffusion presented above. It is true that the current peaking during the second ramp occurs approximately on the diffusive time scale, which for an average temperature of 30 eV and a minor radius of 8 cm is roughly 300 μs. However, this peaking is not observed during the initial ramp, when the plasma was colder and more resistive, and hence should have had a shorter diffusion time scale. The obvious mechanism to suspect for this rapid current penetration and subsequent heating is the double tearing mode. Other factors, besides the faster-than-expected current penetration, also point in this direction. The internal probe measurements for shot 13587 are shown in Figure 5-8. This data show that strong fluctuations appear on probes 2 and 3 concurrent with the application of the second voltage pulse. Further, these fluctuations are strongly suppressed at nearly the same time that the internal inductance peaks. These fluctuations are symptomatic of double tearing modes. More evidence for this supposition is given in the next chapter. Another argument to be made in favor of tearing-mode-assisted current penetration is the destabilizing effect of lower q on these modes. Equations 3-11 and 3-13 indicate that magnetic island growth is strongly inhibited by the increasing values of q on the resonant flux surface ψ_s. The plasma of shot 13587 would then naturally be more susceptible to double tearing modes when the second voltage pulse was applied. The modes could have been much more easily destabilized by this pulse, which would lead to double-valued q profiles. Double-valued q-profiles were not

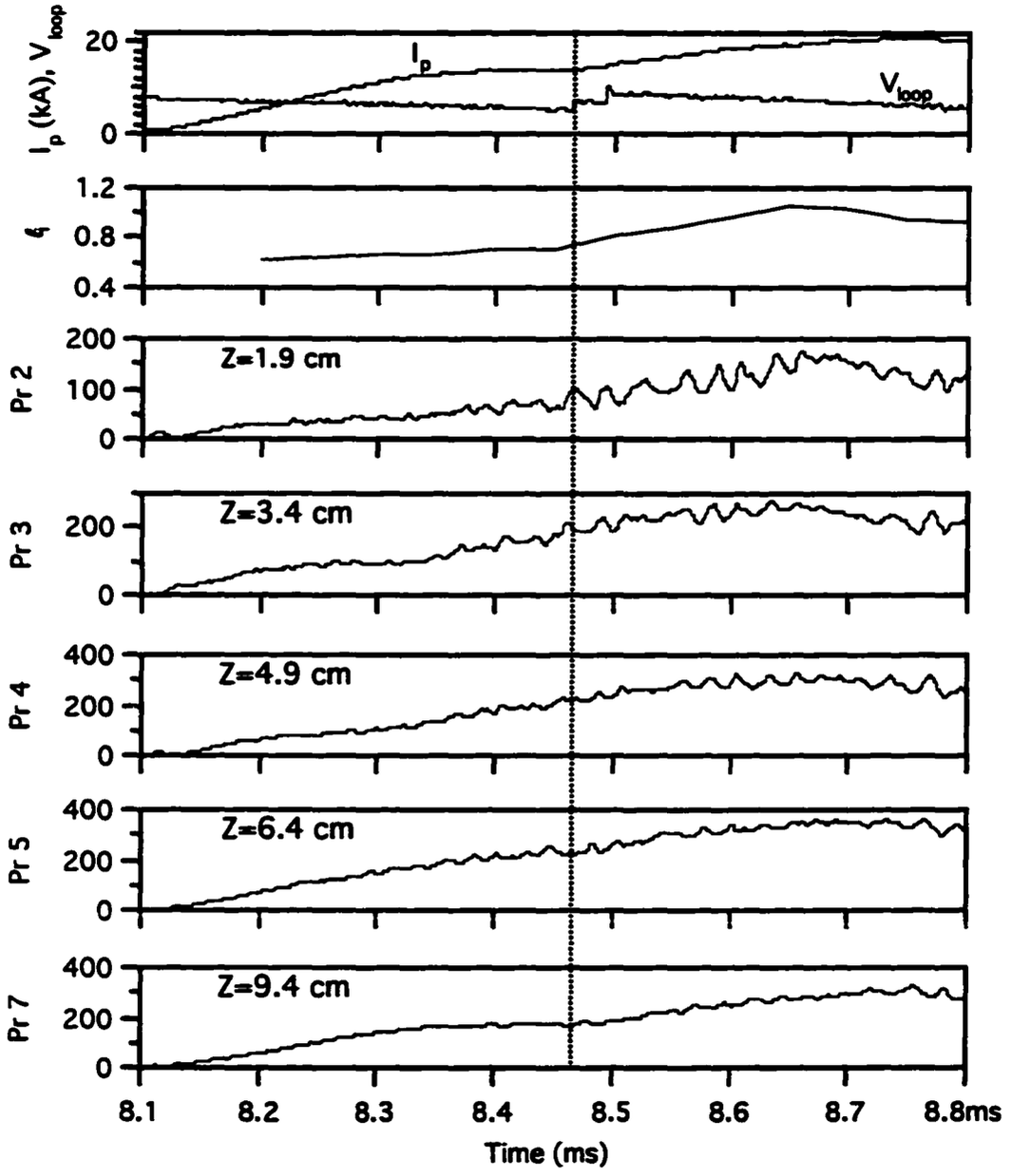

Figure 5-8. Magnetics measurements for shot 13587, showing evidence for double tearing modes. Vertical line indicates application of second voltage pulse. From top to bottom: Plasma current and loop voltage, ℓ_i, and the five magnetic probes, in units of Gauss.

generated by the equilibrium code, however. The five-point magnetic probe measurement and the seven-term parameterization of *FF'* are not sensitive enough to detect a small region of negative shear. As will be discussed in Chapter 6, the q-profiles for fully-formed MEDUSA plasmas are generally quite flat at the plasma center; only small perturbations to these profiles would be required to produce double-valued q-profiles.

5.3 Flux Consumption - Variable B_T and Loop Voltage

A second run campaign, focusing on single-ramp shots like 13521 and 13493, produced another comprehensive survey of plasma performance. Six different operating scenarios were chosen for this survey, and seven shots were chosen for detailed equilibrium analysis. These shots were conducted at four different values of toroidal field and two different loop voltage waveforms. One waveform, the "high-voltage scenario," had an initial voltage of 9.4 volts that decayed to zero at 9.3 ms. The second waveform, the "low-voltage scenario," had an initial voltage of 7.8 volts and decayed to zero at 9.5 ms. Both of these waveforms produced the same maximum current in the OH system, 11.6 kA. The vertical field programming was adjusted for each discharge scenario to provide the best match to the plasma performance. The fill gas pressure was the same for each shot: 1.6×10^{-4} torr of hydrogen measured in the pumping stack.

Four of the analyzed shots were conducted with the high-voltage scenario (the toroidal field is specified at 0.12 m major radius): 14068 at 0.375 T, 14054 at 0.35 T, 14060 and 14021 at 0.3 T, and 14039 at 0.2 T. Two of the shots were conducted with the low-voltage scenario: 14111 at 0.3 T, and 14119 at 0.2 T. The results from the flux consumption data for these shots are given in Table 5-4. The data are summarized in graphical form in Figure 5-9.

Two major trends are evident in these data. The first is the shot performance with

SHOT	C_E	C_{90}	C_{OH}	FC (kA/mV-s) (Total | OH)
14068 High LV 24 kA, 0.375 T	0.61	0.54	0.13	3.8 | 5.3
14054 High LV 22 kA, 0.35 T	0.84	0.58	0.35	3.3 | 4.4
14060 High LV 20 kA, 0.3 T	0.95	0.65	0.45	3.0 | 3.9
14021 High LV 20 kA, 0.3 T	0.81	0.57	0.33	3.2 | 4.3
14039 High LV 16 kA, 0.2 T	1.05	0.81	0.55	2.8 | 3.6
14111 Low LV 16 kA, 0.3 T	0.99	0.90	0.50	2.9 | 3.7
14119 Low LV 12 kA, 0.2 T	1.44	1.00	0.95	2.3 | 2.8

Table 5-4. Flux consumption results for second campaign shots.

toroidal field. The shots improve in every figure of merit with increasing B_T, for both the low and high loop voltage cases; the current per flux (FC) and the maximum plasma current increase with toroidal field, and the Ejima coefficients decrease with it. This result is not unexpected, since the plasma initiation improves with toroidal field. Further, many models of plasma confinement, such as Rebut-Lallia-Watkins and neo-Alcator-START, indicate a positive correlation between τ_E and toroidal field or q_*, which is of course dependent on B_T.

The second trend is that the higher voltage shots outperform the corresponding lower voltage shots. This improvement is again apparent in all of the figures of merit.

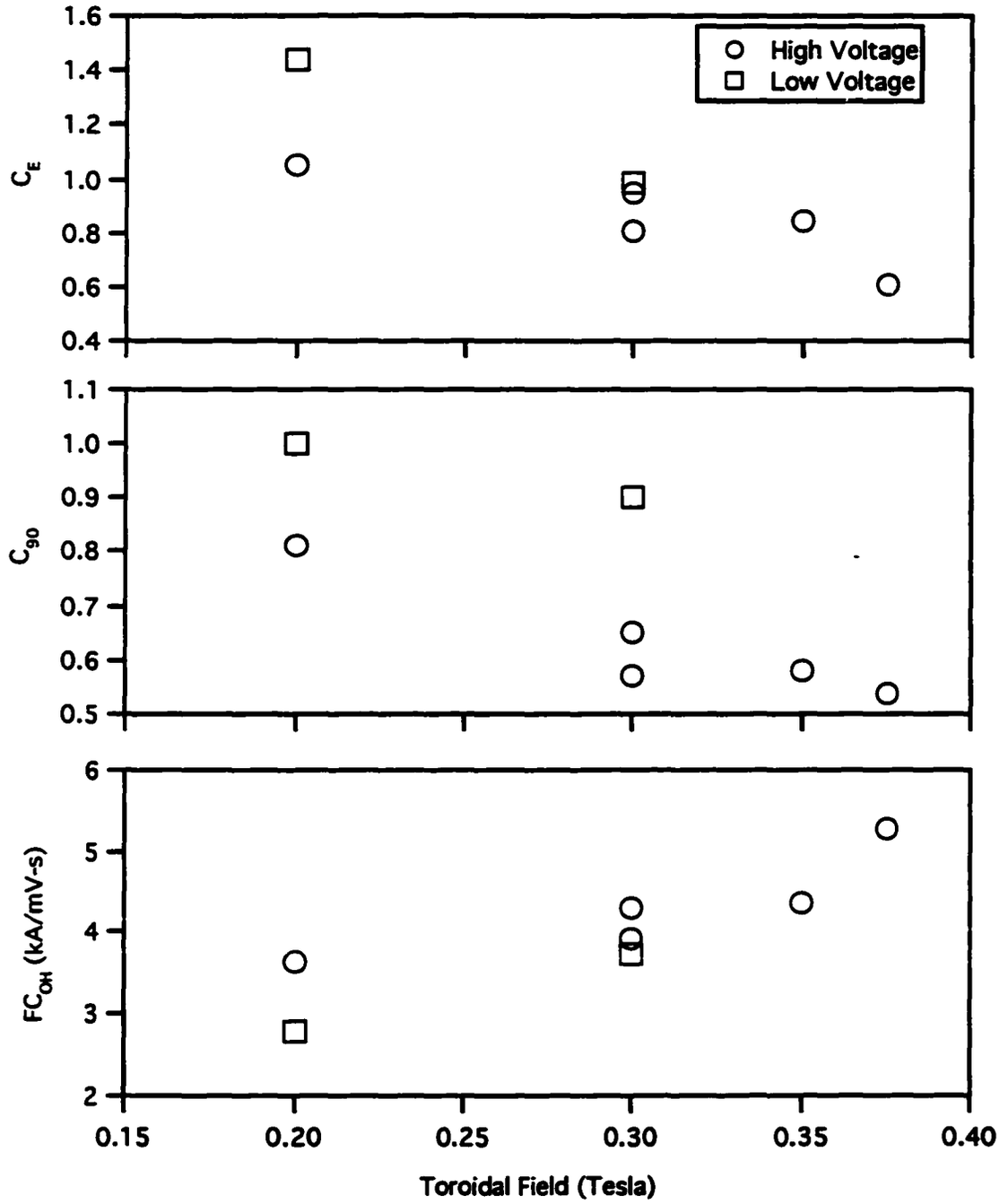

Figure 5-9. Flux consumption figures of merit vs toroidal field for selected shots.

To understand these distinctions, it is useful to examine the behavior of the plasma internal inductance, as this variable is strongly linked to the internal plasma flux Φ_{int}^{ind}. Figure 5-10 contains plots of the evolution of ℓ_i for six of the seven shots studied. (Shot 14021 was not included, but will be discussed below.) Figure 5-10 shows a strong dependence of the ℓ_i waveform on the shot conditions. Examining the high-voltage discharges first, one observes a definite trend in the evolution of ℓ_i with increasing toroidal field. As B_T increases in the high-voltage cases, the internal inductance achieves a lower value during the current ramp, and stays lower until the current maximum has been reached. The behavior of the low-voltage cases in this regard is less clear, but the value of ℓ_i is definitely much lower for shot 14111 (0.3 T) than for 14119 (0.2 T) over most of the discharge.

The comparison between the high- and low-voltage shots in Figure 5-10 is perhaps the most interesting result. It is plainly evident that the lower voltage discharges (14111, 14119) achieve significantly lower values of ℓ_i during the current ramp than do the corresponding higher voltage shots (14060, 14039). One would expect the higher voltage discharges to produce more of a skin effect during the startup period, leading to broader current profiles during the current ramp. That this does not happen indicates that some other mechanism, presumably double tearing modes, must be at work in these discharges.

A final comparison to make is between the supposedly equivalent discharges 14021 and 14060. These shots had identical control parameters, yet produced significantly different flux consumption results. The results for 14021 and 14060 were, respectively: C_E = 0.81, 0.95; C_{90} = 0.57, 0.65; C_{OH} = 0.33, 0.45; FC = 3.23, 3.00 kA/mV-s. Figure 5-11 gives equilibrium data for these two discharges. This figure shows that shot 14021 retains a higher value of ℓ_i over 250 μs of the discharges, spanning most of the current

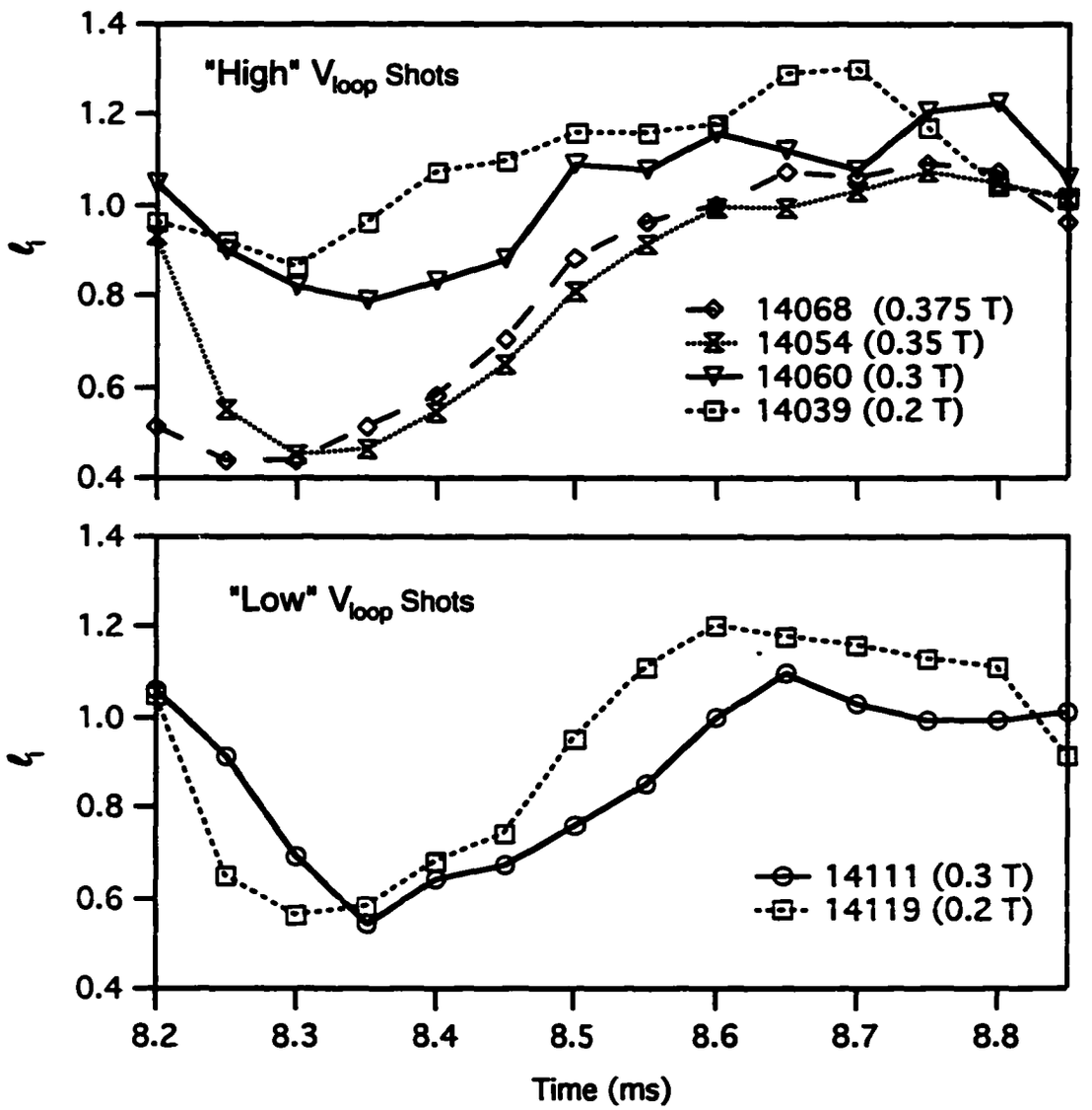

Figure 5-10. Evolution of normalized internal inductance for six shots.

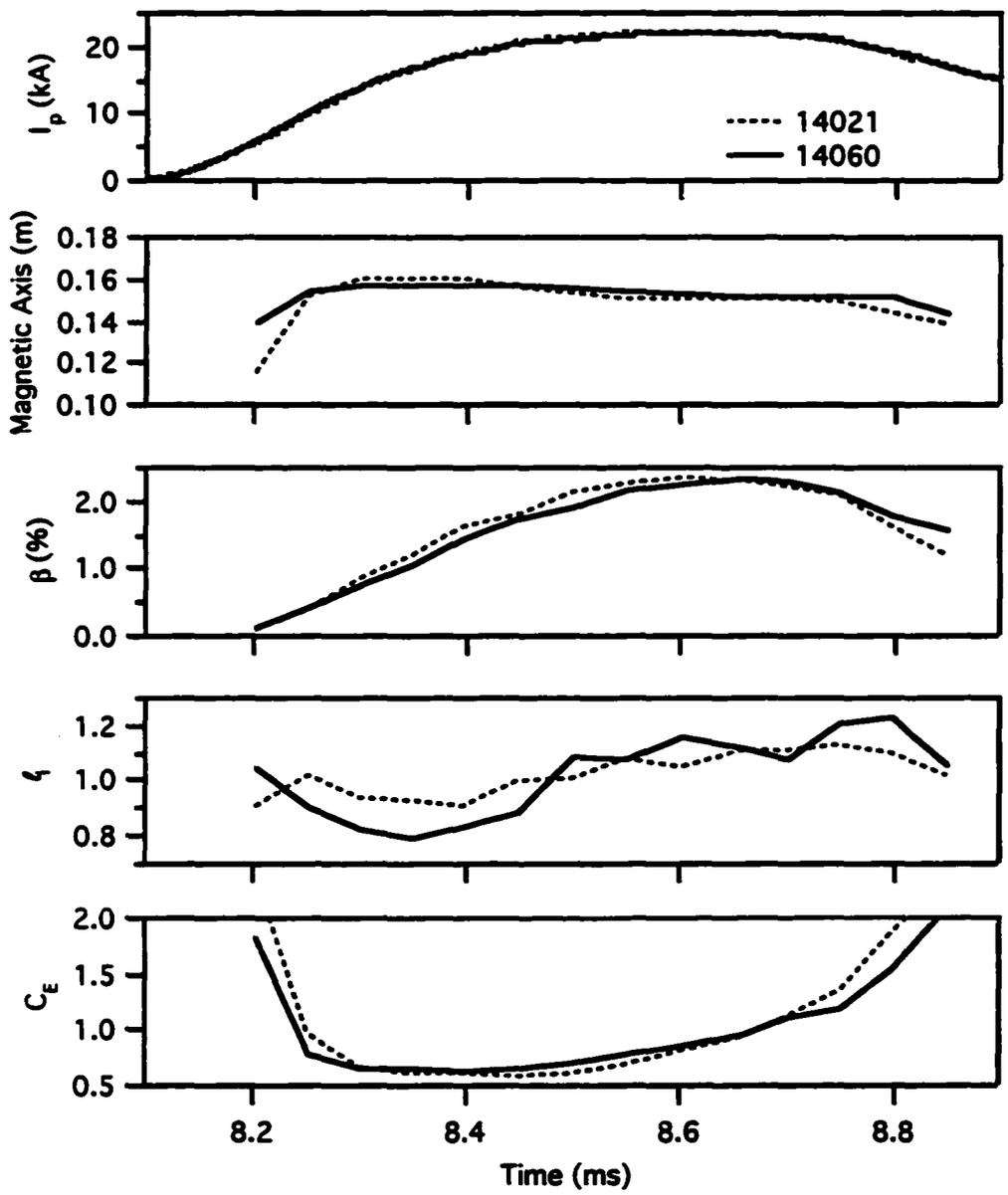

Figure 5-11. Some relevant quantities for comparing shots 14021 and 14060.

ramp. (The data also show a slightly increased β for shot 14021 over this period, as one would expect from a more peaked discharge, but this information is less certain than the current profile data.) It is this difference in the internal inductance that leads to the improved flux consumption. This can be seen in Figure 5-12, which is a comparison of the plasma fluxes for these two discharges. This figure clearly shows that shot 14021 has more inductive flux, and less dissipative flux, than does shot 14060 during the period when the Ejima coefficients are evaluated. It can also be observed that this situation reverses itself after 8.7 ms, which is mirrored in the lower Ejima coefficient for shot 14060 during this later interval in the discharge. It is asserted now, and demonstrated in the next chapter, that these differences are due to the relative levels of activity of double tearing modes in these two discharges.

This chapter discussed overall properties of MEDUSA equilibria, such as pressure, current density, ℓ_i, and β. These quantities were used to determine the flux consumption of a variety of plasma discharges. It was found that flux consumption improves (i.e., C_E decreases) in the cases studied with increasing toroidal field and driving loop voltage. It was determined that the normalized internal inductance, ℓ_i, plays a significant role in determining startup efficiency. An analysis of the mechanisms underlying the current penetration, and hence the evolution of ℓ_i, will be undertaken in Chapter 6.

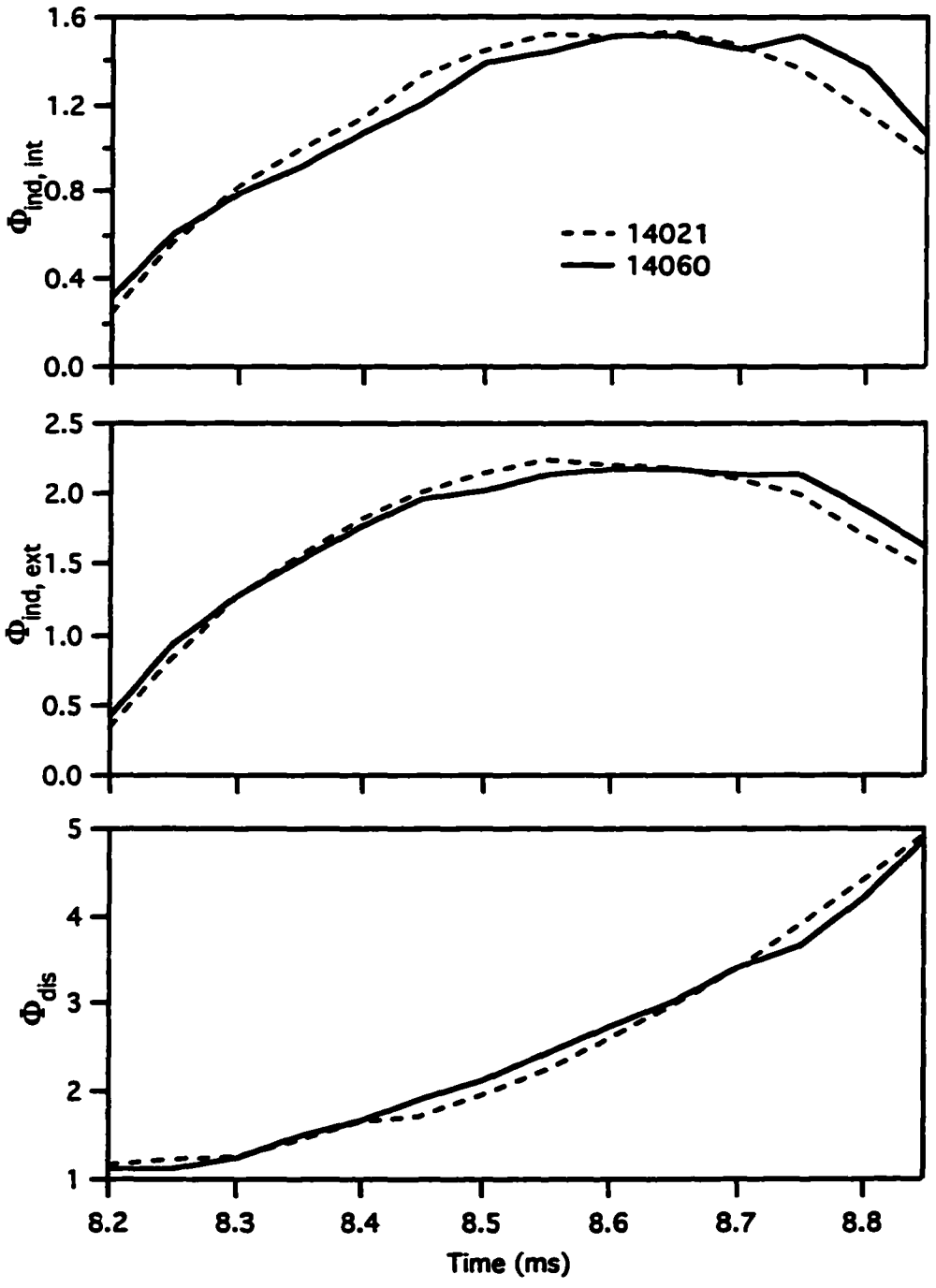

Figure 5-12. Poynting method fluxes for shots 14021 and 14060. From top to bottom: Internal, inductive flux; external, inductive flux; and dissipated flux. All flux units are mV-s.

6. Resistive Instabilities on MEDUSA

This chapter is concerned with resistive MHD instabilities in the MEDUSA tokamak. Two types of resistive tearing modes will be discussed. The first type is the double tearing mode. The presence of double tearing modes in MEDUSA will be established, and the role of these instabilities in current penetration during startup will be discussed. The second resistive instability to be addressed is the internal reconnection event, or IRE. A description of IREs will be presented, which is greatly aided by data from the MEDUSA internal magnetic probe array. These results will be compared to current theories which purport to describe these events.

6.1 Presence and Characterization of Double Tearing Modes

A double tearing mode (here abbreviated DTM) is the result of the reconnection of two magnetic islands of the same helicity [1]. For this pair of islands to exist, the q-profile must be double-valued. This situation exists in tokamaks primarily during the current ramp, when current density is built up on the plasma edge. DTMs relax this current distribution by changing the magnetic topology of the flux surfaces, allowing rapid penetration of the edge current.

The presence of double tearing modes in a tokamak plasma is usually indicated by positive spikes on the loop voltage trace and Mirnov oscillations that correspond to the reconnecting mode number [2,3]. The plasma current ramp also is observed to slow or even reverse momentarily. The positive loop voltage spikes and negative current spikes are the result of the rapid current penetration that occurs during a DTM. This penetration increases the internal inductance ℓ_i, which increases the total plasma inductance. The external voltage

and plasma current then change according to

$$V = L\frac{dI}{dt} + \frac{1}{2}I\frac{dL}{dt}. \qquad (6\text{-}1)$$

The increase in ℓ_i also typically leads to an outward displacement of the magnetic axis, as required by the radial equilibrium force balance.

There is ample evidence of the existence of DTMs on MEDUSA. Virtually every discharge has spikes on the loop voltage waveform that die off as the current ramp ends; these spikes clearly correspond to dips in the plasma current waveform. The MEDUSA Mirnov coil array has not been sufficient to produce mode numbers of the observed DTMs. This is due to the nature of these modes in spherical tokamaks. Double tearing modes usually occur at a relatively small value of *r/a* due to the large magnetic shear at the edge. This necessarily means that Mirnov coils cannot be "close-fitting" as they are in conventional tokamaks and therefore cannot detect the small perturbative signals associated with double tearing modes. In MEDUSA, then, the Mirnov coils can only provide information on bulk plasma motion associated with DTMs. Figure 6-1 shows the signals for five Mirnov coils, plasma current, and loop voltage for one DTM; phase information is not apparent.

In contrast to the Mirnov coils, however, the internal probe array provides a great deal of information on these instabilities. Figure 6-2 is an example of some raw magnetics data around two DTMs in shot 14060. Two of the larger events in this trace are highlighted by the dashed lines, but these are clearly not the only DTMs in this figure. The plasma current dips, and the loop voltage spikes upward, as expected. The internal probe data shows an almost stepwise increase in the radial magnetic field concurrent with the voltage spikes.

The observed DTMs can be analyzed within the framework of the Grad-Shafranov

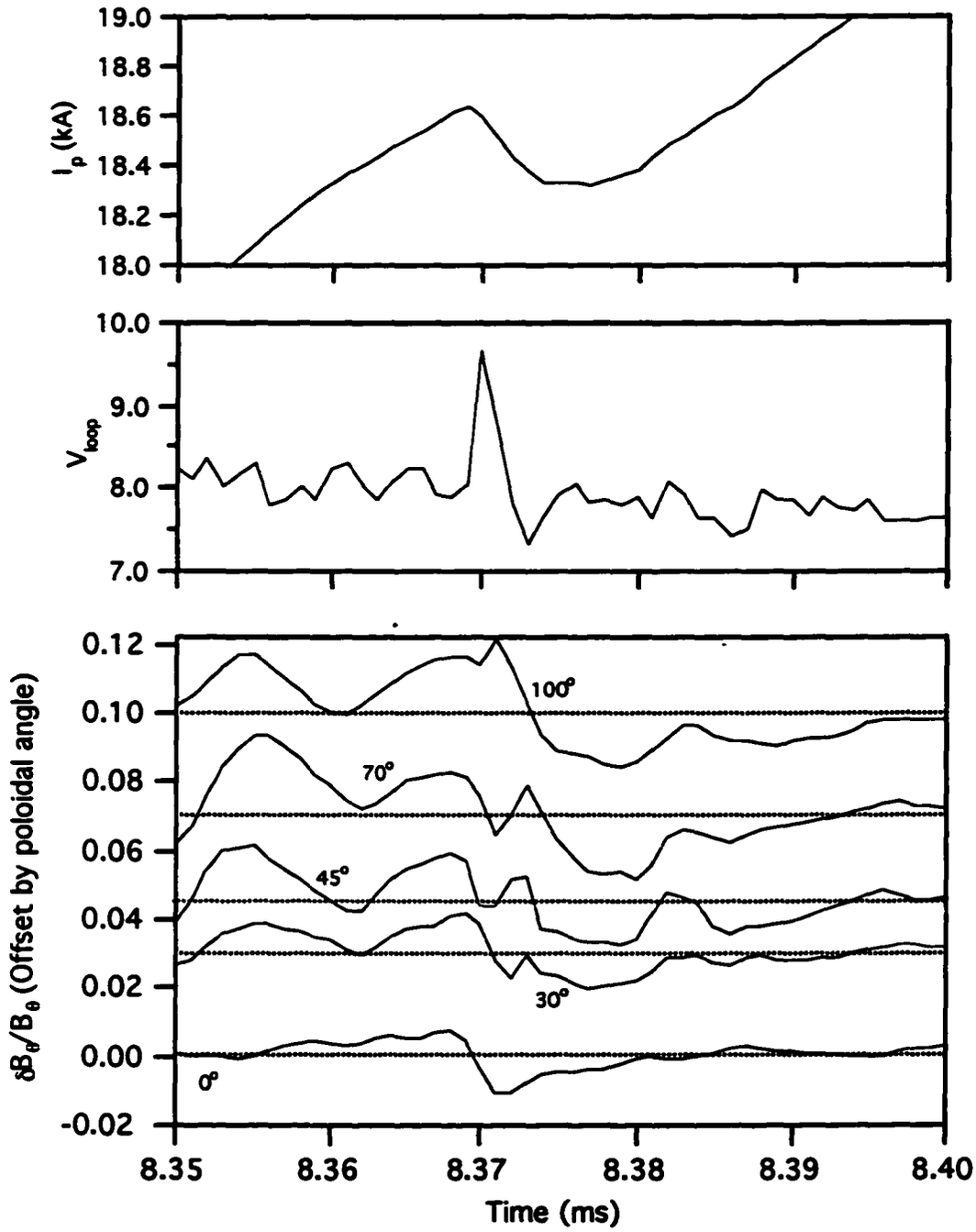

Figure 6-1. Plasma current, loop voltage, and Mirnov coil signals for a double tearing mode (shot 13521). Mirnov coil signals are expressed as the "AC" signal divided by the "DC" (< 10 kHz) signal.

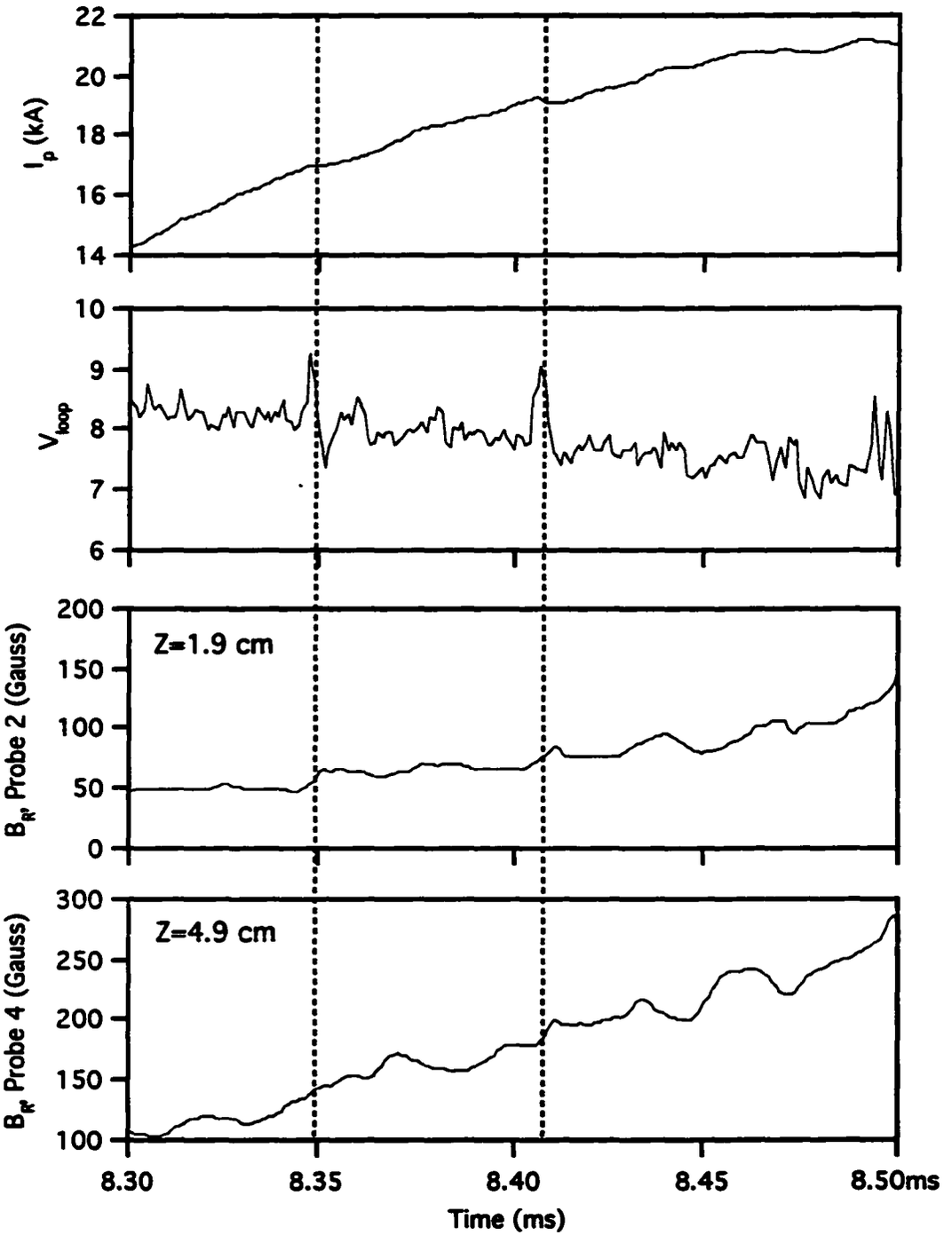

Figure 6-2. Raw magnetics data around two double tearing modes; shot 14060. From top to bottom: Plasma current, loop voltage, internal magnetic probes 2 and 4.

equation. The ideal equilibrium equation naturally cannot be used to describe a resistive double tearing mode itself. However, the equilibrium state of the plasma can be described before and after a DTM. The plasma can be considered to be in ideal MHD equilibrium on the Alfvén, or hydrodynamic, time scale, which for MEDUSA is roughly 1 μs.

An example of equilibrium results about a double tearing mode is given in Table 6-1. Some of the data from these equilibria are displayed graphically in Figure 6-3. Figure 6-3 gives flux surface plots and profiles (vs ψ_N) for a DTM in shot 13521. This figure and table illustrate many of the aspects of double tearing modes that have been discussed. The current profile is seen to fill in quite rapidly, the pressure in the core increases, and the value of q_0

Quantity	8.370 ms Pre-DTM	8.385 ms Post-DTM
I_p (kA)	18.4	17.9
Magnetic Axis (m)	0.117	0.134
ℓ_i	0.39	0.50
κ	1.36	1.26
q_0	7.4	2.4
q_{98}	12.3	12.6

Table 6-1. Equilibrium results about a double tearing mode - shot 13521.

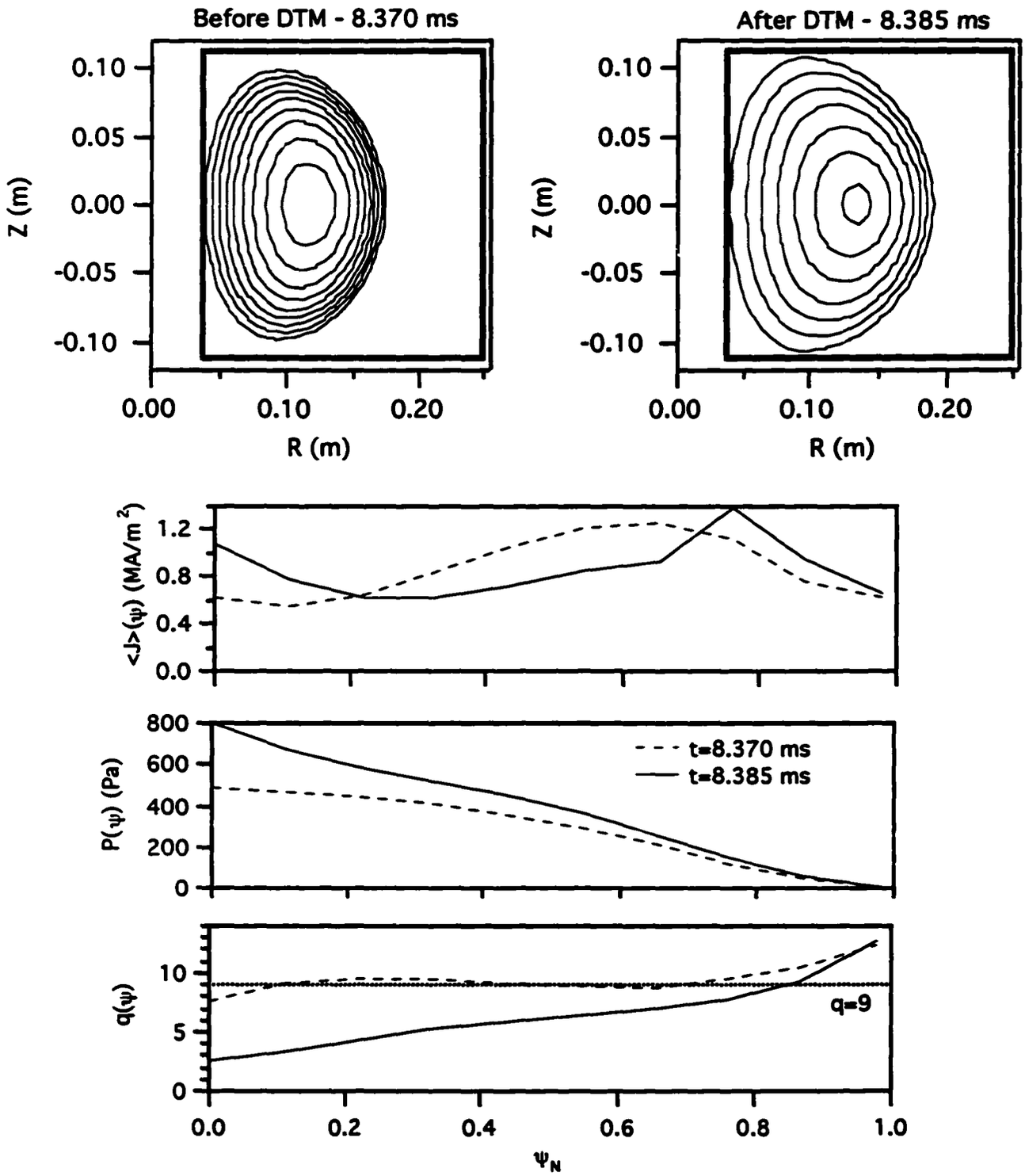

Figure 6-3. Equilibrium data for a DTM in shot 13521. Profiles are plotted against normalized ψ. From top to bottom: flux surface plots, profiles of average current density, pressure, and q.

drops substantially as more current is driven on axis. The plasma moves outward and becomes less elongated. The DTM in Figure 6-3 appears to reconnect across the q=9 flux surfaces.

Figure 6-4 illustrates one of the double tearing modes shown in Figure 6-2. In this case, the equilibrium does not explicitly show a double-valued q-profile before the reconnection. This profile is quite flat around the magnetic axis, which is characteristic of spherical tokamak equilibria. The equilibrium code does not have enough information or degrees of freedom to find a double-valued q profile in this case, but it is plain that small changes in these equilibria could produce such a profile. Figure 6-4 illustrates the first DTM of the two highlighted in Figure 6-2. Figure 6-4 again shows a filling-in of the current profile and a drop in q_0. This first event appears to reconnect about q=4.

6.2 Effect of Double Tearing Modes on Startup

Double tearing modes have a substantial impact on the startup of MEDUSA plasmas. One would expect the effects of DTMs to be detrimental to the plasma. The reconnection of magnetic island pairs consumes more energy than unreconnected islands [4], and the reconnection enhances particle and energy transport, which are dissipative processes. The effects of double tearing modes on MEDUSA are not necessarily detrimental, however.

In Chapter 5 it was shown that two discharges, 14021 and 14060, though identical from the operations standpoint, performed quite differently from each other in terms of the flux consumption figures of merit. It was shown that part of the reason for the superior performance of the higher-performing shot (14021) was a larger value of ℓ_i throughout the startup period. The details of these differences are given in Table 5-2 and Figures 5-11 and 5-12.

The larger value of ℓ_i in the higher-performing shot is due to the early presence of

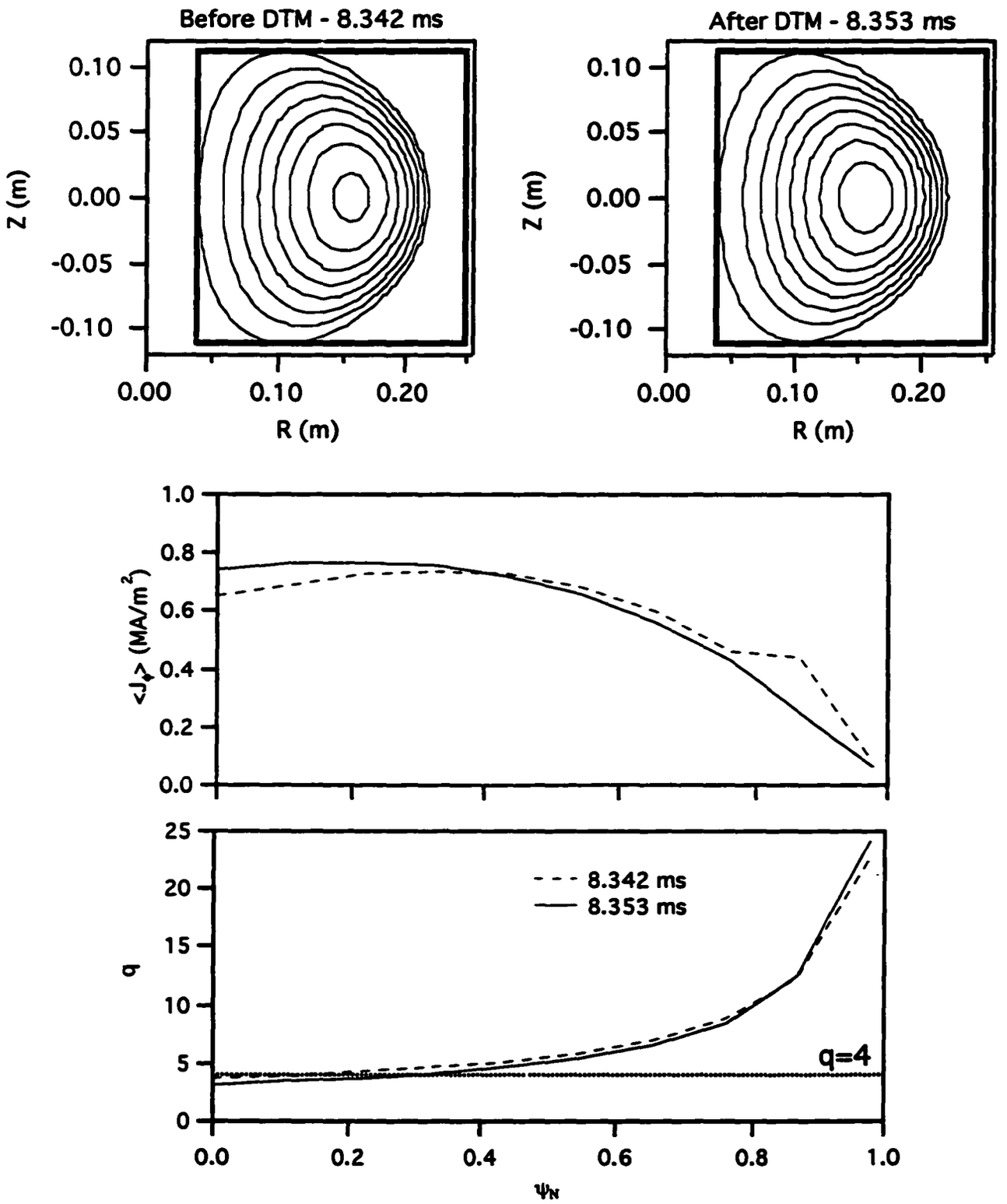

Figure 6-4. Equilibria of a double tearing mode at t=8.35 ms in shot 14060.

double tearing modes in that discharge relative to the poorer-performing shot (14060). This is illustrated in Figure 6-5. This figure gives the time derivative of the plasma current, the "AC" component of the loop voltage, and the signals from probes 2 and 3 for these two discharges. (The "AC," or "fast" component of the loop voltage was created by smoothing the original signal with a 100 μs window and subtracting the smoothed signal from the original signal.) Both discharges experience double tearing modes as evinced by sharp spikes on the loop voltage traces and decreases in the plasma current ramp rate. In the interval between 8.15 and 8.25 ms, however, the higher-performing shot experiences a greater amount of tearing mode activity than the poorer-performing shot. This activity clearly leads to increases in the internal magnetic field measurements, and hence to larger ℓ_i. The poorer-performing shot features more virulent tearing mode activity later in the discharge—the pair of events discussed earlier are clearly visible in Figure 6-5. These latter events cause the internal probe measurements to approach those of the higher-performing shot.

Figure 6-6 gives pressure and current profiles (vs ψ_N) for these two discharges for three time slices during the startup period. The current density on the graphs is the average on each flux surface. The current density of the poorer-performing shot (14060) can be seen to broaden over the first interval, and then peak after the two large reconnections discussed earlier. Meanwhile, the current density for the higher-performing shot (14021) is consistently more peaked than that of the poorer-performing shot. The pressure for shot 14021 is initially lower than that of 14060, but by the last time slice it is somewhat higher. This higher pressure is most likely due to an increased temperature brought about by plasma heating caused by greater on-axis current. The increased temperature implies a decreased plasma resistivity, and hence a smaller dissipative loss during startup.

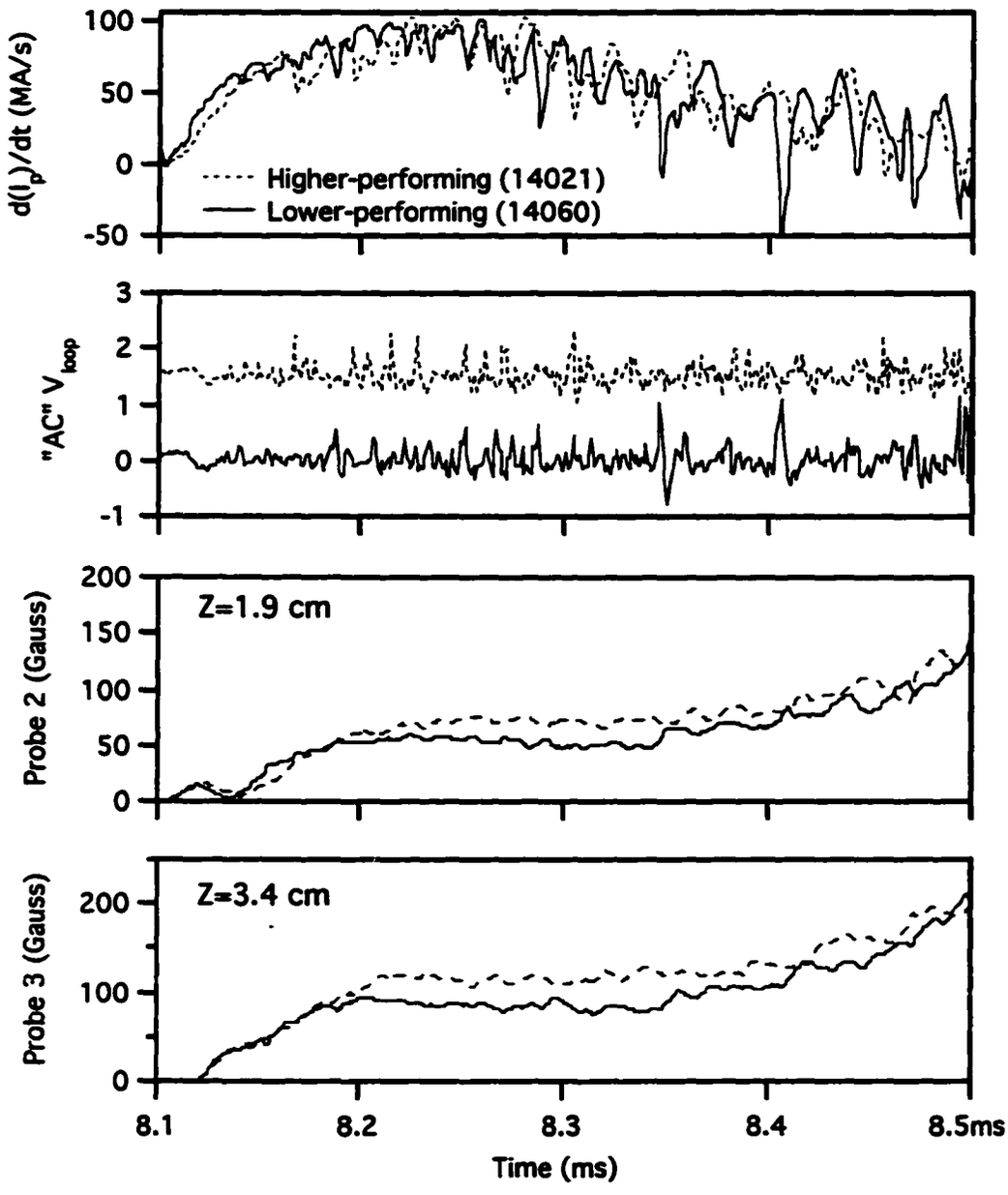

Figure 6-5. Raw magnetics for shots 14021 and 14060. From top to bottom: Time derivative of the plasma current, the "fast" or "AC" (above 10 kHz) component of the loop voltage, magnetic probes 2 and 3. The AC V_{loop} signal for 14021 is offset by 1.5 V for illustration.

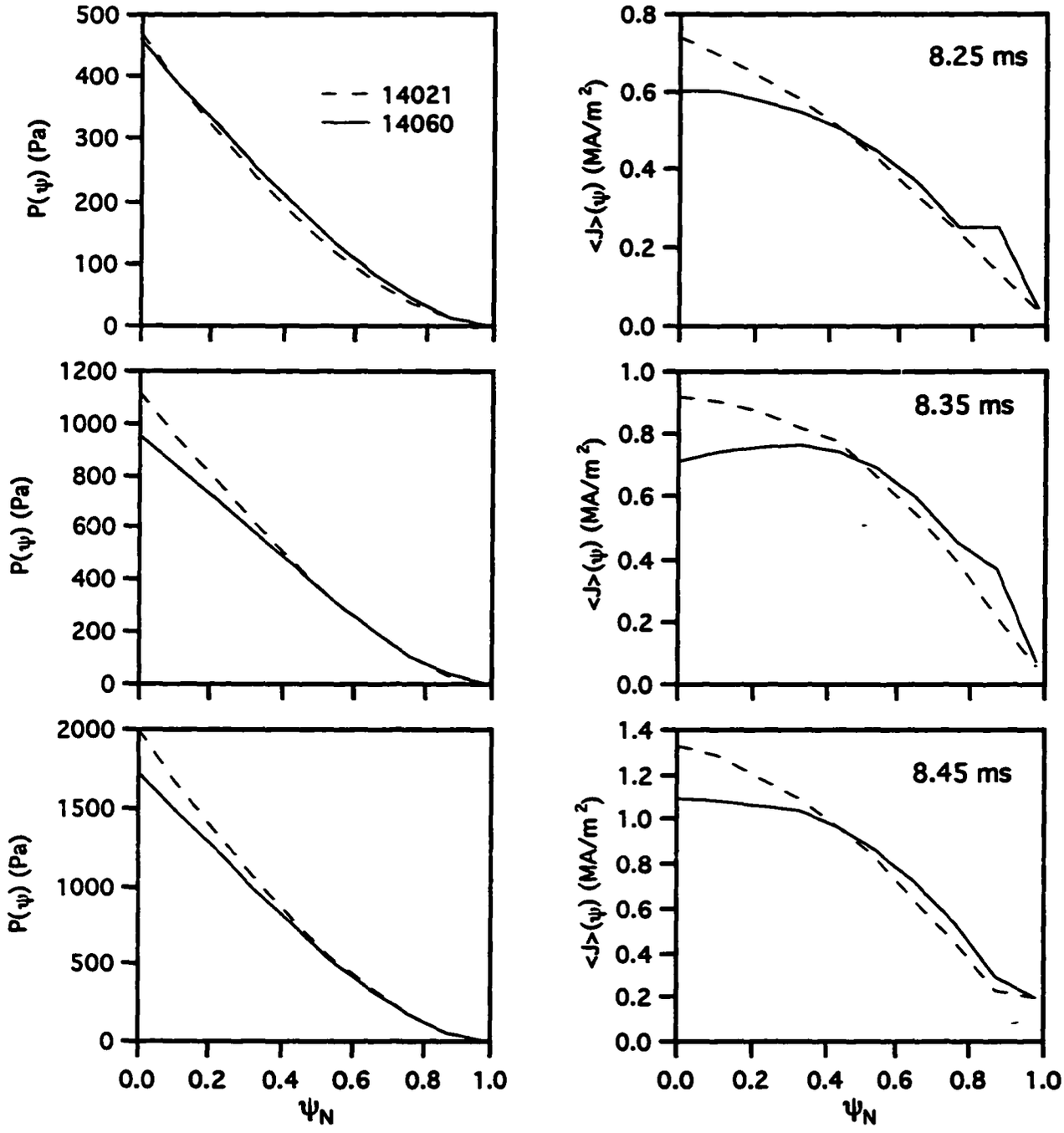

Figure 6-6. Pressure and current profiles for shots 14021 and 14060. Times at right indicate equilibrium time slice. Graphs at left are pressure. Graphs at right are flux-surface averaged toroidal current density. Profiles plotted vs normalized flux.

The effects of double tearing modes are also apparent when comparing the two different loop voltage scenarios introduced in Chapter 5. There are two pairs of discharges for comparison in this case: the high and low voltage shots at 0.3 T and 0.2 T. The high-voltage 0.3 T shot was number 14060, and the low-voltage 0.3 T shot was number 14111. The high-voltage 0.2 T shot was number 14039, while the low-voltage 0.2 T shot was number 14119. In Chapter 5 it was shown that the flux consumption improved (i.e., C_E decreased) as the loop voltage increased. This difference was again found to be due to differences in ℓ_i. The lower-voltage shots achieved significantly lower values of ℓ_i than the higher-voltage shots, which implied lower values of internal plasma flux and hence poorer flux consumption.

Magnetic diffusion alone fails to explain the observed startup behavior. The magnetic diffusion time in MEDUSA is roughly 300 μs, as discussed in Chapter 5. In Figure 5-10 it can be seen that the current distribution, as represented by ℓ_i, "fills in" on the two low-voltage shots (14111, 14119) on roughly this time scale. The high-voltage shots (14060, 14039), on the other hand, peak significantly faster than the low-voltage shots (order of 100 μs faster), and maintain higher values of ℓ_i throughout the current ramp. This is directly contrary to the expectations of current diffusion theory, which predicts that the higher-voltage case would peak more slowly and maintain broader current profiles than the lower-voltage cases. This is a result of increased conductivity at the edge caused by the greater current, and hence more heating, driven by the larger voltage. It can be argued that in a small tokamak like MEDUSA, edge power losses are significant, and that broader current profiles would not be produced by a higher loop voltage. Even if this argument is accepted, however, it does not explain why the higher-voltage shots reached peaked current profiles faster than the lower-voltage shots.

Double tearing modes are again found to be responsible for the faster current penetration of the higher-voltage shots. DTM activity is clearly visible in the loop voltage and magnetic probe traces of the pair of 0.3 T shots shown in Figure 6-7. The loop voltage trace of the higher-voltage 0.3 T shot (14060) certainly shows greater DTM activity than the lower-voltage 0.3 T shot (14111). This is clearly reflected in the internal probe signals, which feature much stronger DTM-induced fluctuations and reflect a significantly more peaked current profile. Rapid increases in the both sets of probe signals can be usually be associated with identifiable DTM events on the loop voltage trace. For example, upturns in probe signals 2, 3, and 4 in the higher-voltage 0.3 T shot can clearly be connected with the voltage spikes at 8.35 and 8.4 ms.

Figure 6-8 gives the plasma current, loop voltage, and internal probe traces for the pair of 0.2 T shots. Little DTM activity can be observed on the loop voltage trace of the lower-voltage 0.2 T shot (14119) for roughly the first 300 μs of the discharge. This lack of activity is mirrored in the internal probe signals, where the three innermost probes report small measurements during this period. The lower-voltage 0.2 T shot is a good illustration of a current diffusion-dominated discharge for this first 300 μs period. The signals of probes 4 and 5 show some plateauing early in the discharge, and subsequently show increases in the radial magnetic field between 8.2 and 8.35 ms that are not associated with specific instances of tearing modes. After this interval, though, DTM activity begins to appear on the loop voltage trace; these events can be directly associated with rapid increases in probe measurements, particularly the events around 8.43, 8.49, and 8.53 ms. The higher-voltage 0.2 T shot experiences much greater tearing mode activity than the lower voltage shot, just as in the 0.3 T case. This increased DTM activity leads to substantially increased core probe measurements, also as in the 0.3 T case. Figure 6-9 contains plots of the pressure and current density profiles of the 0.2 T shots. In this figure distinct differences

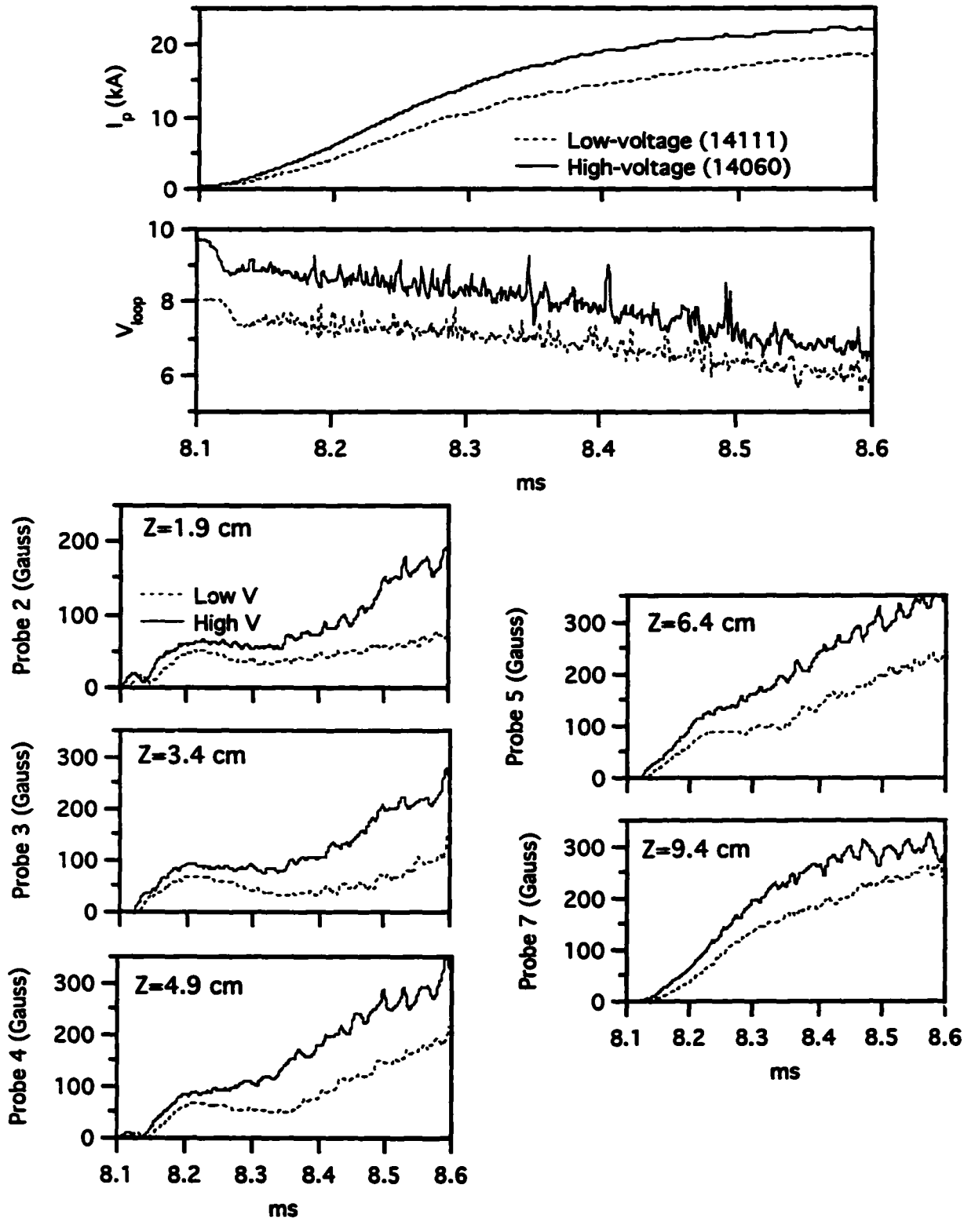

Figure 6-7. Raw magnetics measurements for 0.3 T shots 14060 (HV) and 14111 (LV).

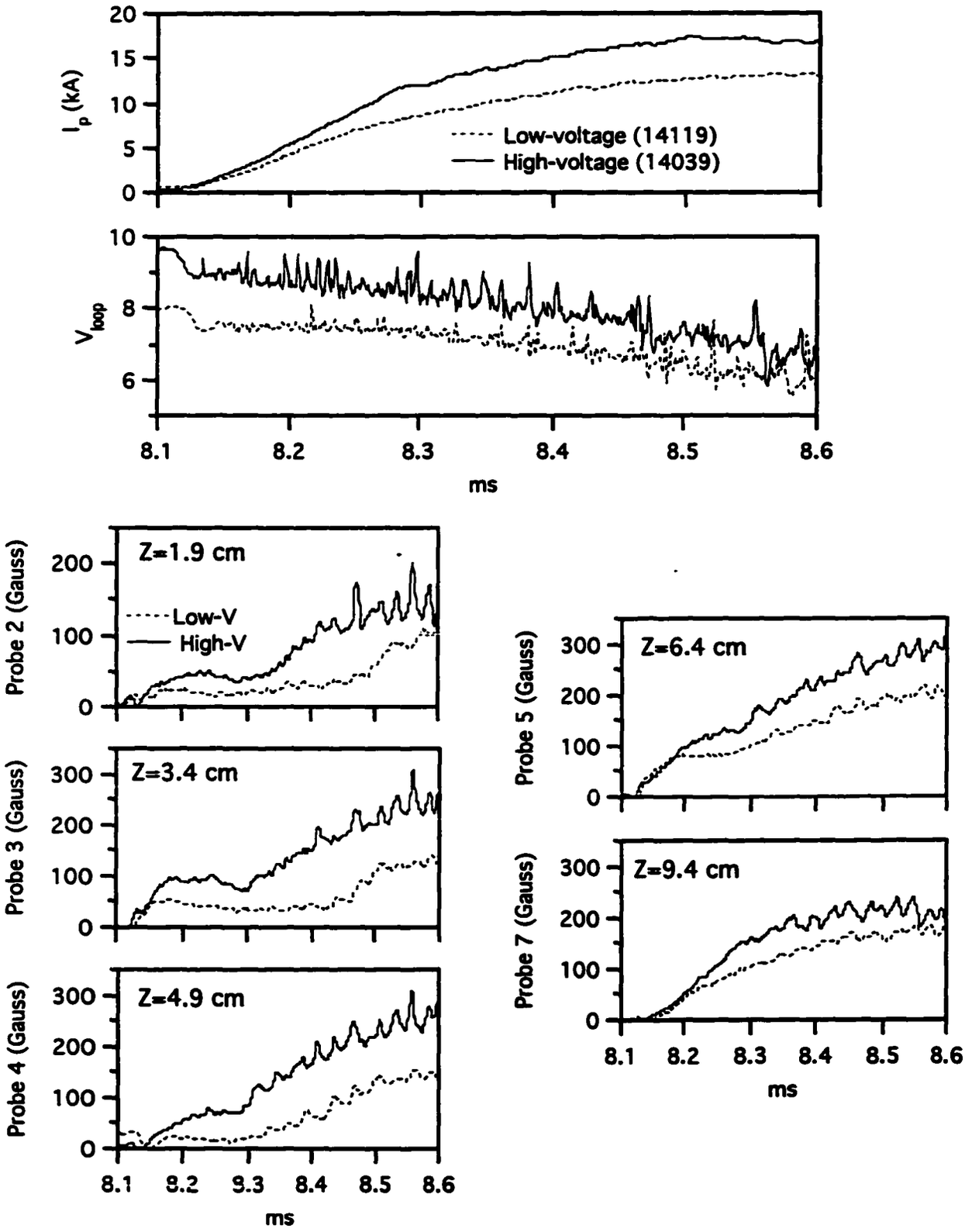

Figure 6-8. Raw magnetics measurements for 0.2 T shots 14039 (HV) and 14119 (LV).

between these two discharges can be observed. The current profile for the lower-voltage shot is hollow until about 8.5 ms, while for the higher-voltage shot it is much more peaked. These differences are mirrored in the pressure profiles. As was the case in the comparison of discharges 14021 and 14060, the differences in the pressure profiles of these two 0.2 T discharges are likely due to differing temperatures in the two discharges.

The effects of toroidal field strength on DTM activity and startup efficiency are more complex than the effects of varying the loop voltage. The results in Chapter 5 indicate that increasing toroidal field results in increased flux consumption and decreased Ejima coefficients for both the high- and low-loop voltage scenarios. It is also found that higher values of toroidal field suppress double tearing mode activity. Figure 6-10 is a comparison of some of the raw magnetics data for three high voltage shots—those at 0.375 T (14068), 0.3 T (14060), and 0.2 T (14039). Included in this figure are the plasma current and loop voltage for all three of these discharges, and the five internal magnetic probe signals for the 0.375 T and 0.2 T shots. All three discharges experience DTM activity during startup. As the toroidal field increases, the amount of DTM activity in the current ramp decreases, and the onset of virulent DTM activity occurs later in the discharge. The result of this decrease in activity is a corresponding decrease in the value of ℓ_i during the startup as shown in Figure 5-10.

Figure 6-11 gives the time evolution of q-profiles for the high voltage shots at 0.375 T, 0.35 T (14054), 0.3 T, and 0.2 T. The q-profiles of the 0.375 and 0.35 T discharges relax from double-valued at 8.25 ms to monotonically increasing with ψ_N at 8.55 ms. The q-profiles of the lower field discharges (0.3 and 0.2 T) are monotonically increasing throughout the startup period. Except near the edge, $q(\psi)$ increases with toroidal field; the increasing value of q with toroidal field is the reason that double tearing modes occur later in

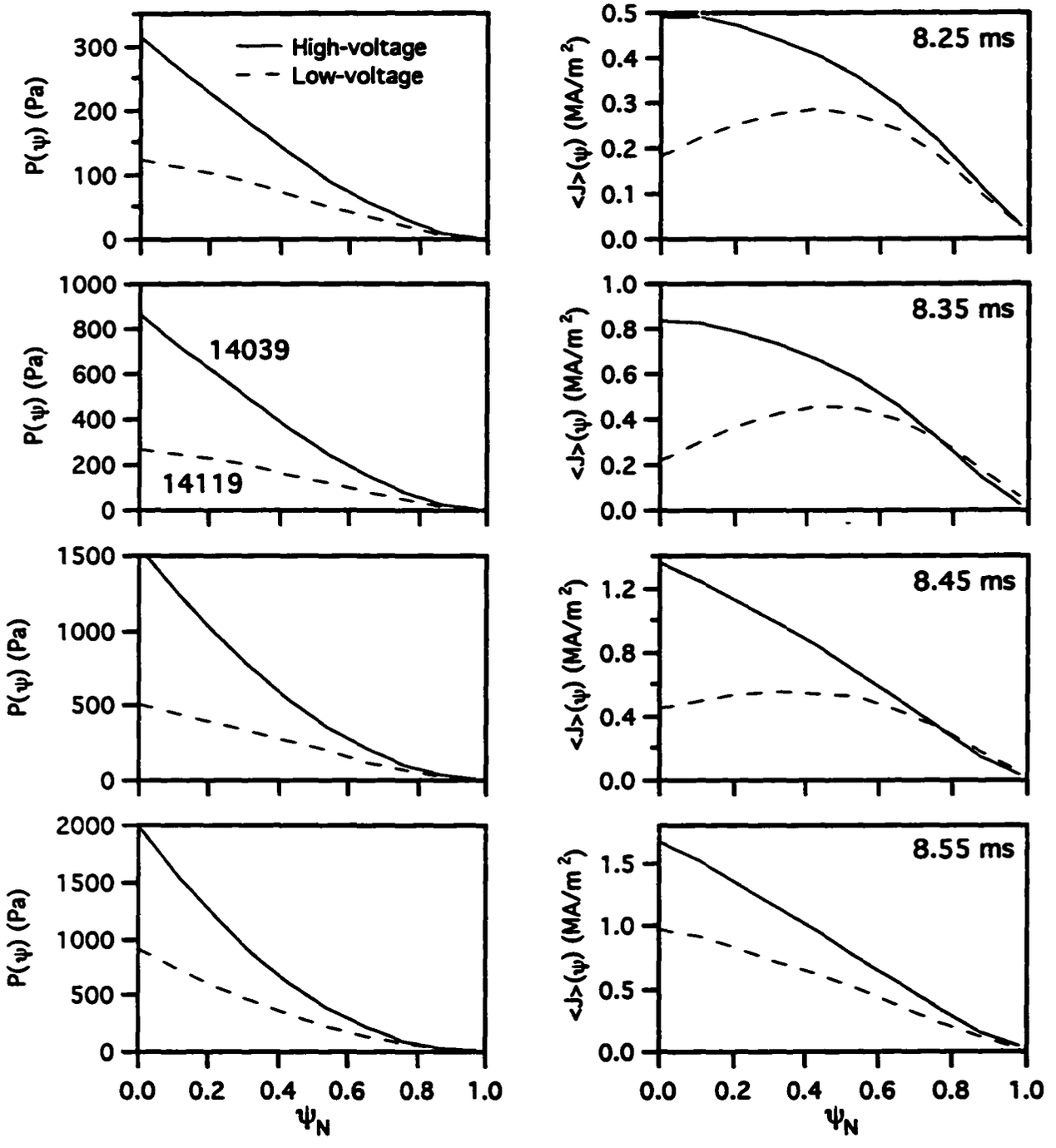

Figure 6-9. Evolution of pressure and current profiles for 0.2 T shots. Times at right indicate equilibrium time slice. Graphs at left are pressure. Graphs at right are flux-surface averaged toroidal current density. Profiles plotted vs normalized flux.

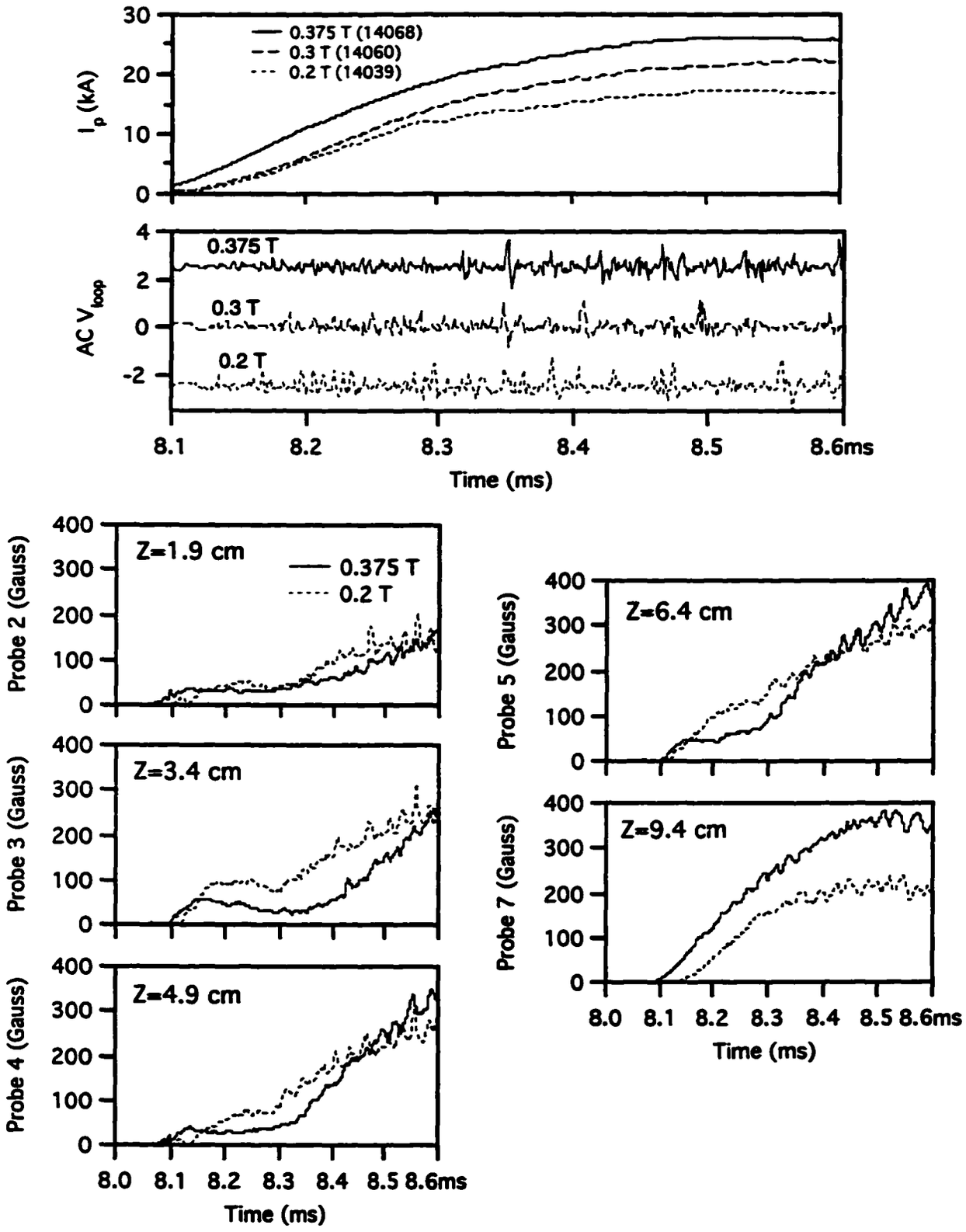

Figure 6-10. Raw magnetics measurements for high voltage shots. Loop voltage signal is the "fast" component. Some V_{loop} signals offset for clarity. Probe signals are shown for 0.2 T and 0.375 T shots only.

time as the field increases. Several terms in the magnetic island growth equation (3-13) are stabilized with increasing q. Thus the higher-field discharges can successfully maintain lower values of ℓ_i during the current ramp due to the absence of double tearing modes.

Further complicating this picture is the observation that the current ramp begins roughly 30 μs sooner for the 0.375 and 0.35 T discharges than for the 0.3 and 0.2 T shots. (This discrepancy is also evident in the differences in the q-profiles shown in Figure 6-11.) This behavior is most likely due to improved coupling with the ECR preionization at higher field and reduced error field losses during plasma initiation. The earlier initiation of the higher-field discharges result in reduced breakdown losses and hence a reduced Ejima coefficient. Figure 6-12 shows the plasma current and the current ramp rate for these four shots in the 160 μs interval following plasma initiation. The plasma current ramp rate increases with increasing toroidal field, which correlates with the decrease in inductance with increasing toroidal field discussed previously.

The internal inductive component of the plasma flux is roughly proportional to $I_p \ell_i$ (see equations 3-22 and 3-23.) As this quantity increases, the Ejima coefficient decreases. This quantity may be increased by increasing I_p, ℓ_i, or both. In the case of the two high-voltage 0.3 T shots (14021 and 14060), the higher-performing shot had an increased ℓ_i due to double tearing modes early in the current ramp. The comparison of high- and low-voltage shots at equal toroidal fields showed that the high-voltage shots had smaller values of C_E due to increased ℓ_i during the current ramp, while the ultimate plasma currents were roughly proportional to the applied voltage. The data for the toroidal field scan, on the other hand, show that the higher-field shots achieve lower values of C_E because of increased plasma current despite having lower values of ℓ_i during the current ramp. In fact, the lower values

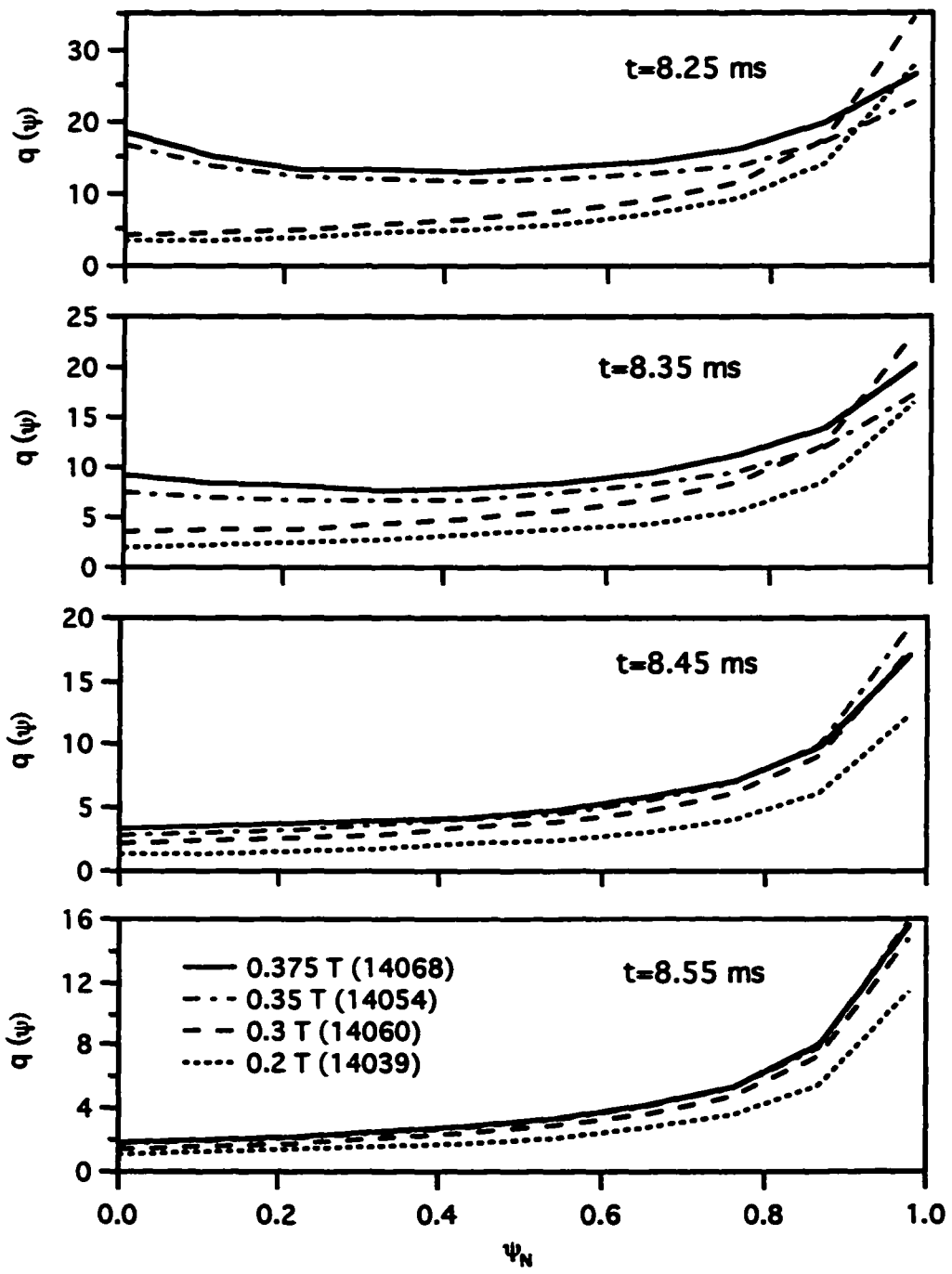

Figure 6-11. Evolution of q-profiles for four high-voltage shots.

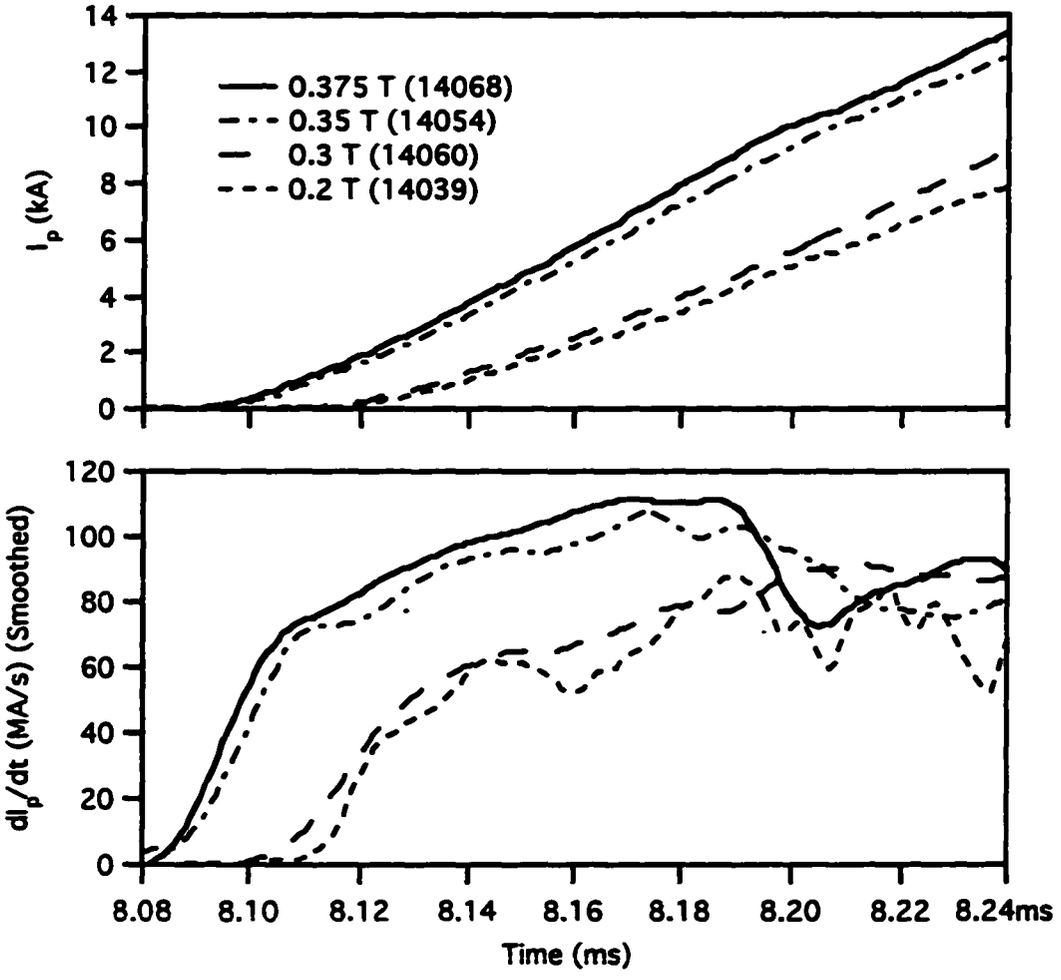

Figure 6-12. Plasma current and current ramp rate for high-voltage shots in a 160 μs interval after plasma initiation.

of ℓ_i in the higher-field discharges are partially responsible for these increased currents, although improved plasma initiation and improved confinement undoubtedly also contribute.

The effects of double tearing modes on startup flux consumption are therefore mixed, and must be considered as they interact with other quantities of interest. Increased DTM activity was beneficial to startup in the first two cases considered in that it led to an overall increase in the internal plasma flux and a corresponding decrease in C_E. Increases in the toroidal field at constant loop voltage led to decreased DTM activity, which in that case led to decreased values of ℓ_i and increased plasma current ramp rates. The increased plasma current then led to an increased internal (and external) plasma flux and a decreased C_E. However, the increase in plasma current is only partially due to the absence of double tearing modes. Improvements in plasma initiation at higher field certainly help to increase the plasma current, as has been demonstrated. Additionally, improved plasma confinement at higher field may also play a role in improving the flux consumption. Of the scaling relations discussed in Chapter 2, only neo-Alcator (equation 2-25) does not show a positive correlation between τ_E and B_T. The ITER-89P and Rebut-Lallia-Watkins give confinement times proportional to $B^{0.2}$ and $B^{0.5}$, respectively, while the Lackner-Gottardi and neo-Alcator-START expressions give confinement times proportional to $q^{0.4}$ and q, respectively. These expressions are all derived for steady-state plasmas, and as such are not directly applicable to the problem of startup. One can speculate, though, that the principle of improved confinement and reduced transport with increasing toroidal field is still valid.

6.3 Internal Reconnection Events

IREs have been observed on MEDUSA since the first weeks of operations. They are discrete occurrences, which may be seen once, twice, or not at all during a given shot. Most discharges on MEDUSA do not experience IREs; they appear in perhaps 5-10% of shots depending on the recent operating history.

An internal reconnection event is characterized by a rapid upward spike in the plasma current (over 10-20 μs) and a corresponding spike down in the loop voltage. The internal radial field, as observed with the probe array, drops over an IRE and recovers slowly, if at all. The deeper probes are the most strongly affected, and may lose 30-50% of their signal. A precursor usually appears on the probe signals about 100 μs before the IRE occurs. Figure 6-13 is an illustration of these magnetics measurements over an IRE. Triple probe measurements show strong transient behavior of the electron density about IREs. Figure 6-14 contains a plot of electron density during an IRE at a major radius of 12 cm and a height of 3 cm above the midplane (corresponding to ψ_N=0.2-0.3). The density is observed to spike up rapidly immediately before (50 μs) the IRE, and then crash precipitously. This is interpreted as an expulsion of core plasma during the event.

IREs almost always occur after the plasma has peaked in current and has a relatively high value of ℓ_i. Often they occur during the "rampdown" period, when the plasma is being compressed into the center column by the mismatched vertical field. IREs tend to occur more frequently when the vacuum is less clean, as after a vent. They can be made to appear by overdriving the vertical field system and forcing the plasma into the center column.

The raw magnetic probe data show the same behaviors over many different IREs. These behaviors are illustrated in Figure 6-15, which is a plot of plasma current and internal

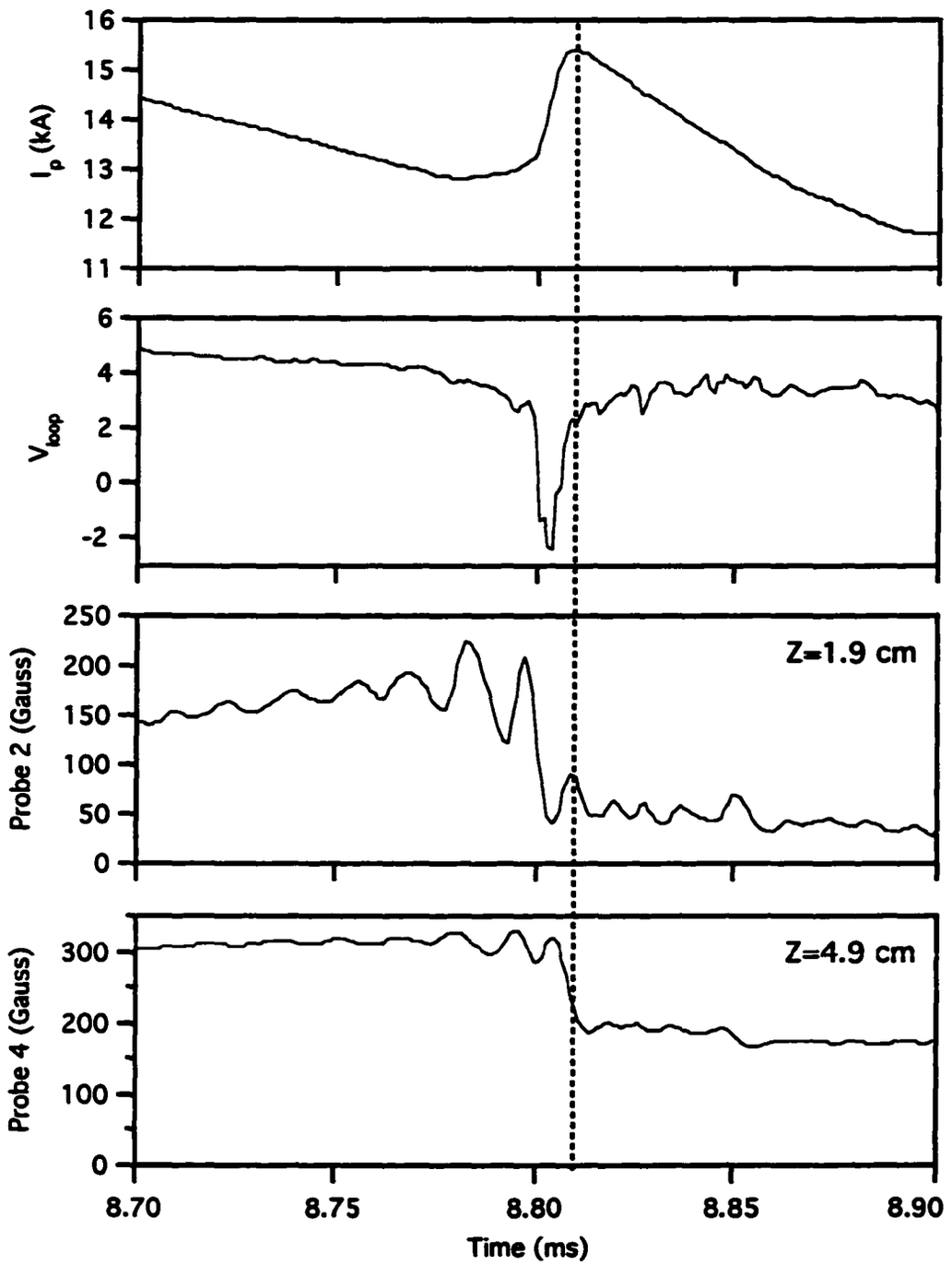

Figure 6-13. Some raw magnetics data for an IRE in shot 13462.

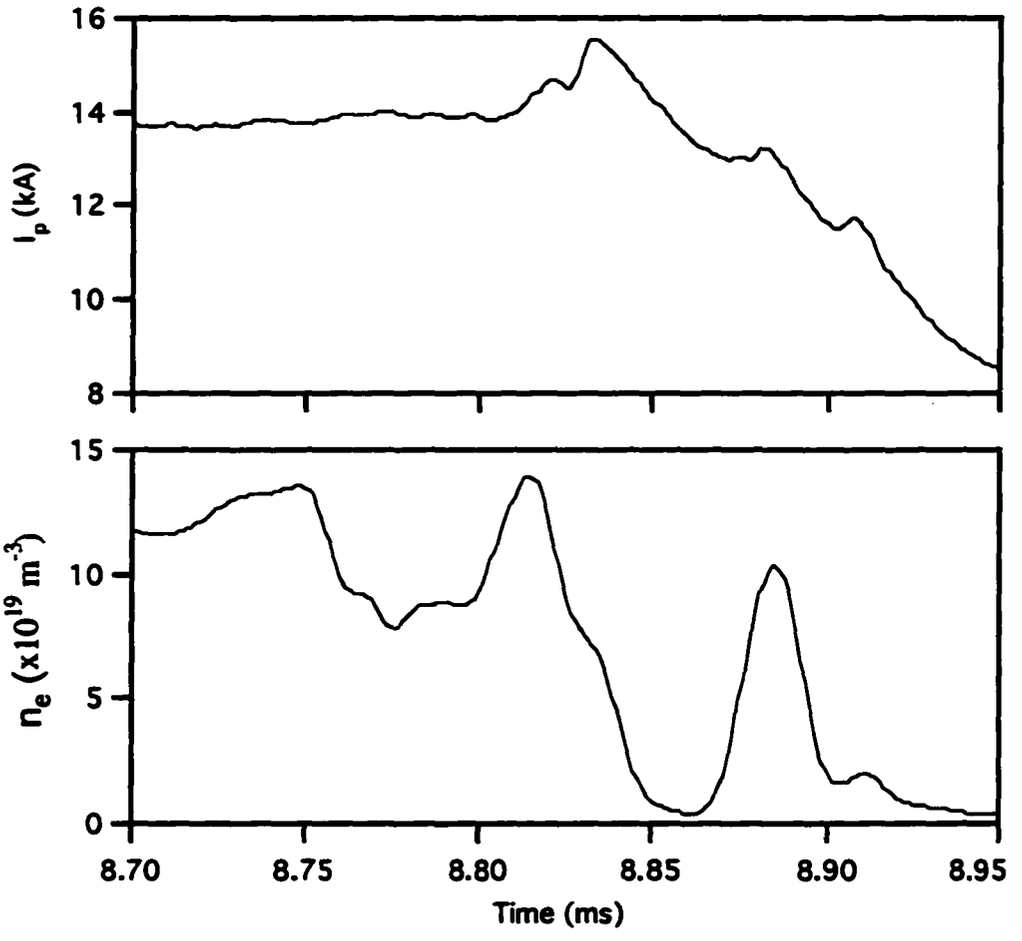

Figure 6-14. Triple probe measurement of the density change across an IRE.

probe measurements for an IRE in one shot. Generally the outermost probe (7) is outside the plasma by the time the IRE occurs and sees little effect due to the event besides a mild perturbation. About 100 μs before the IRE occurs, the probes that are in the plasma begin to show coherent oscillations in the neighborhood of 65-75 kHz. Prior to this, the oscillations are not necessarily coherent from one probe to another. The three "middle" probes (3,4, and 5) exhibit measurements that are nearly identical at about 100 μs before the IRE. As the event approaches, the signals begin to differentiate, with the innermost signal becoming the strongest. Immediately prior to the upward current spike, the probe signals collapse. The inner probe shows the greatest drop (30-50%), and the outermost the least (10%). This rapid change in field structure denotes a gross change in the plasma internal inductance. (As an aside, some of the drop in the probe signals is brought about by inward plasma motion. This motion will result in a decreased major-radial field at the probe even with no change in the internal inductance.) The signals usually do not return to their pre-IRE levels, although they sometimes do for "minor" IREs, which frequently precede the larger variety. These observations, especially those dealing with the coherent oscillations, lead to the conclusion that IREs in MEDUSA are the result of some magnetic island interaction/reconnection. The Mirnov coils could not determine any mode numbers for the precursors or IREs for essentially the same reason as the double tearing mode case—they are far from the perturbation, and the resultant signal is too small to be meaningful.

Internal reconnection events may be analyzed with the equilibrium code in the same fashion as double tearing modes. One selects time slices before and after the event, where the plasma is presumably in a quasi-equilibrium state, and reconstructs the equilibria at these instances. The events were analyzed at two instances: immediately before the magnetic field crash, called the pre-IRE time slice, and near the peak of the current spike, called the post-IRE time slice. An example of IRE equilibrium results is given in Table 6-2. Figure 6-16

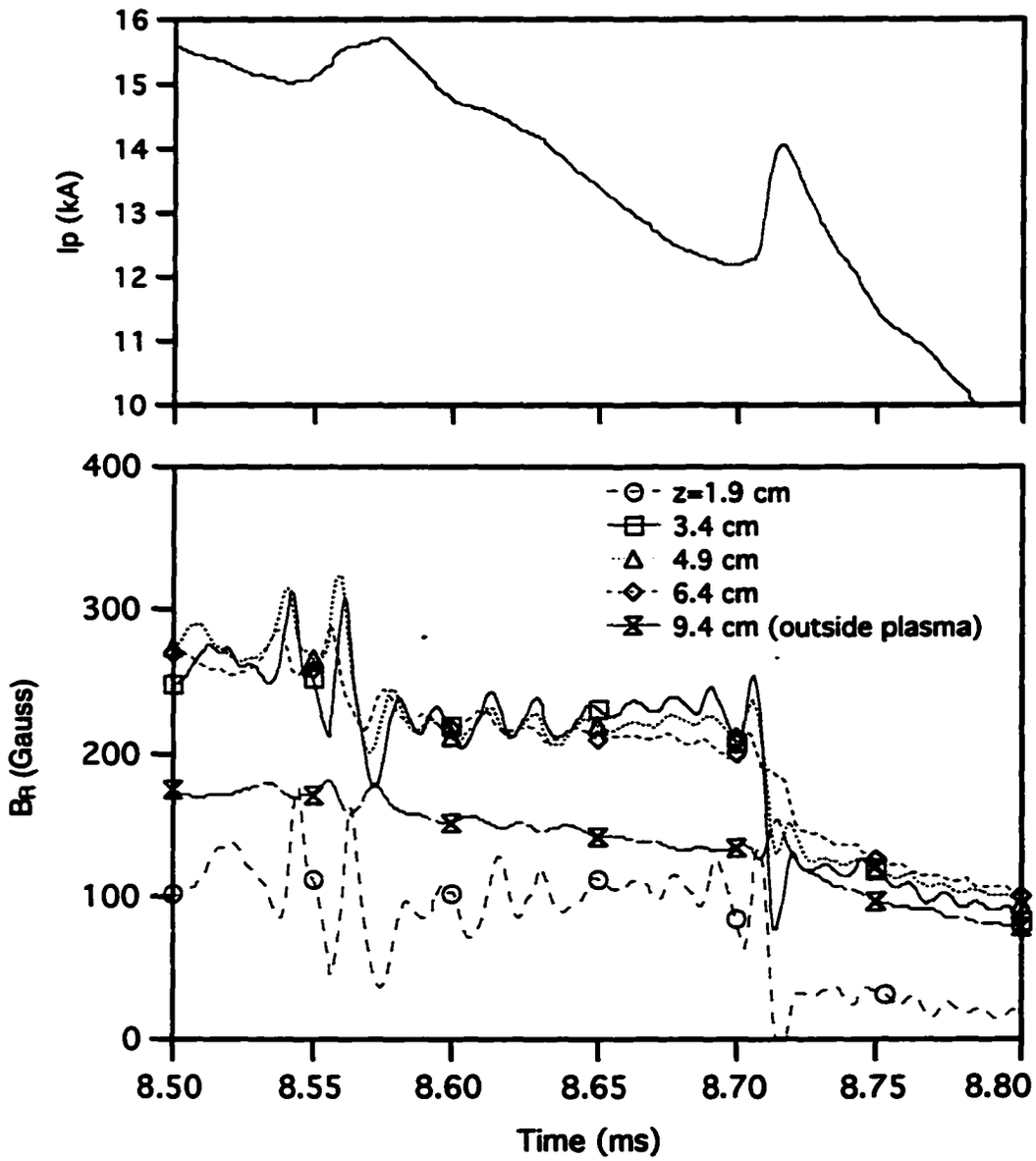

Figure 6-15. Internal field dynamics associated with IREs in shot 13404.

contains graphical data from the event summarized in the table. The results reveal several features of these events. The plasma moves radially inward during the IRE, by as much as 1 cm or more. The internal inductance drops precipitously as the current profile changes from a peaked profile to a broad or hollow one. The plasma beta drops sharply as well, to between 30 to 70 percent of the pre-IRE value. The pressure profile broadens considerably.

Quantity	8.629 ms Pre-IRE	8.662 ms Post-IRE
I_p (kA)	14.9	15.8
R (m)	0.0968	0.0862
Mag. Axis (m)	0.109	0.0921
ℓ_i	0.82	0.46
β (%)	0.44	0.18
κ	1.14	1.30
q_0	1.35	4.69
q_{98}	8.45	7.09

Table 6-2. Results from equilibrium analyses of IRE in shot 13032.

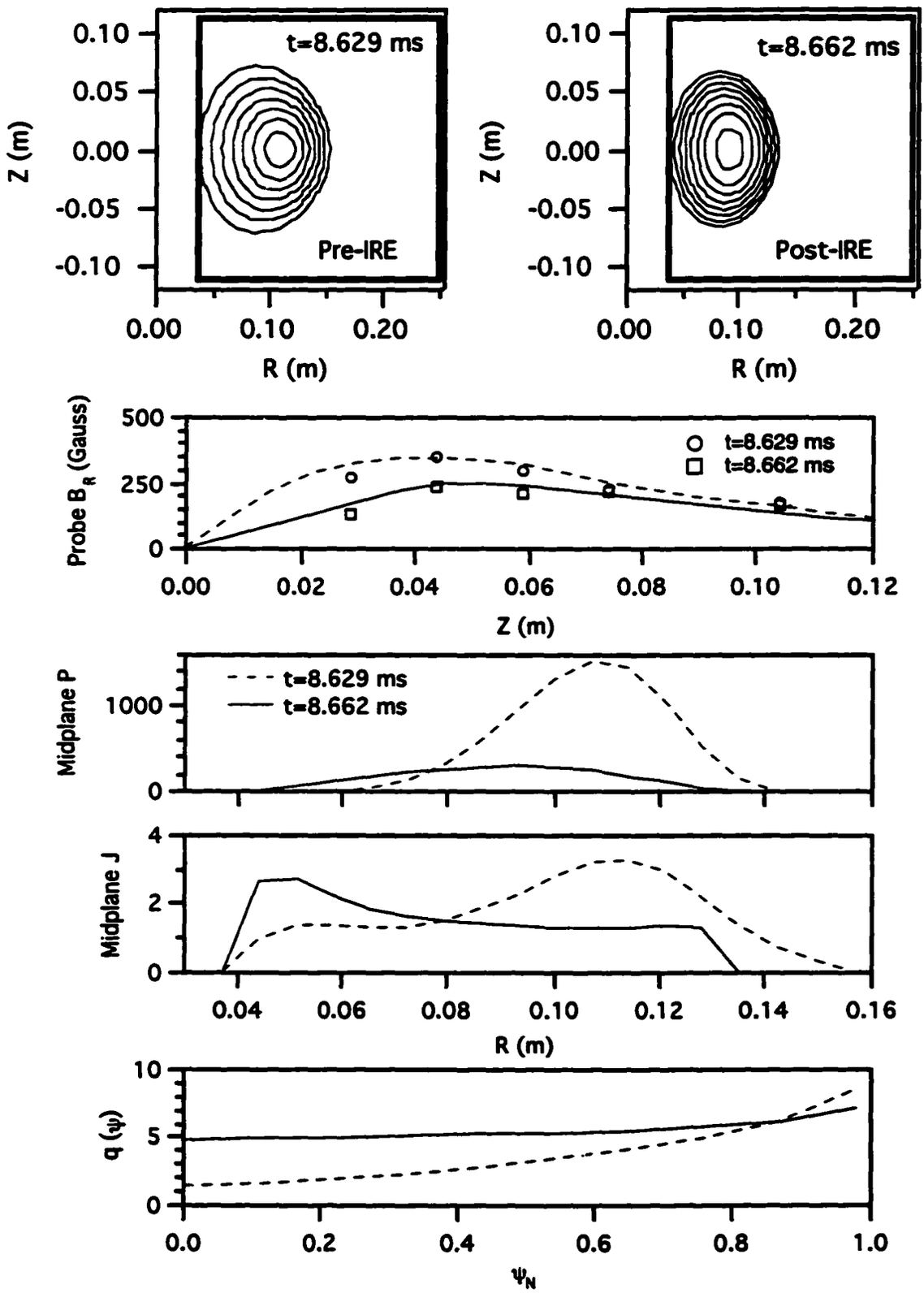

Figure 6-16. Equilibrium data about an IRE in shot 13032. Top to bottom: flux plots, B_R at the probe (Gauss), midplane P (Pa) and J (MA/m^2) vs R, q vs ψ_N.

The elongation increases, as is normally the case in STs when ℓ_i drops. The central q increases sharply, and the entire q-profile becomes flat or even hollow. The value of q_{98} changes much less, decreasing by 5 to 15 percent.

These data indicate that an internal reconnection event is indeed quite disruption-like, as discussed in Chapter 3. It features the same broadening of the current channel, drop in pressure, and spikes in current and voltage waveforms. The IRE, though, does not lead to a hard disruption. One hypothesis that has been proposed to explain the absence of hard disruptions following IREs is colloquially referred to as the "START picture." This hypothesis argues as follows [5,6]. When a major internal reconnection occurs in a conventional tokamak, ℓ_i and β_p fall, while the plasma retains approximately the same geometry. The increase in plasma current leads to a decrease in q_a, which helps destabilize the plasma. In a spherical tokamak, ℓ_i and β_p again both fall, but the plasma moves slightly inward (into the higher field region) and elongates. These changes in geometry and current result in little change in q_a, which stays approximately constant, and stabilizes the plasma.

This hypothesis is difficult to defend on the basis of the results presented here. In all of the IREs analyzed, q_{98} fell during the IRE, despite decreases in R and increases in κ. (This apparent paradox can be resolved if the effect of the current distribution on q is acknowledged.) It can be argued that these data do not provide an adequate test of the hypothesis, in that the edge safety factors in these shots (7 - 11) are significantly above the minimum required for external kink stability (3 - 5). This argument does not address the crux of this hypothesis, though, which is that q_{98} remains essentially constant over the IRE. Operating with a lower edge safety factor, for example by lowering the toroidal field, presumably would not alter the results given here.

The large edge q may hold the key to the resilience of ST plasmas to disruptions after IREs. Since IREs only occur when ℓ_i is large (roughly > 0.8), they presumably are reconnections of low mode-number island structures (such as 2/1 and 5/2 or 3/2 and 2/1), since these flux surfaces are only present in high-ℓ_i MEDUSA plasmas. In a conventional tokamak with q_a=3, these islands could well occupy a majority of the plasma volume, including the edge. However, in a spherical tokamak, where the edge q is naturally large, these island chains would not reconnect near the edge, leaving the magnetic topology there unchanged and giving the plasma time to recover from the internal reconnection. Toroidicity-induced coupling of magnetic islands in STs complicates this view.

This line of reasoning leads into a second model for IREs. Another hypothesis that has been considered recently posits that magnetic helicity is conserved in an ST plasma over an IRE [7]. Magnetic helicity, K, is defined as

$$K \equiv \int \mathbf{A} \cdot \mathbf{B}\, dV \tag{6-2}$$

where **A** is the vector potential and the integral is over a volume bounded by a flux surface. The helicity is conserved on the resistive time scale [8]. This relation is usually not significant for tokamaks without some constraint on the flux surface of interest. In tokamaks such as HIT-II [9] helicity is conserved within a metal shell known as a flux conserver. The nature of the internal reconnection event in a tokamak might be such that the outer plasma acts as a flux conserver for the inner plasma. In this case helicity would be conserved by the plasma over an IRE.

This hypothesis was tested by calculating the helicity for six time slices encompassing 3 IREs. The expression for helicity can be approximately recast for tokamaks, including STs, as [10]

$$K \propto 2\Phi_T \Psi_p \tag{6-3}$$

where Φ_T is the plasma toroidal flux and Ψ_p is the poloidal flux. Applying the original definition of q as the derivative of the toroidal flux with respect to the poloidal flux (given in Chapter 2) and manipulating gives

$$K \propto 2\Psi \int q d\Psi \tag{6-4}$$

where the integral is taken from the center of the plasma to the edge, and $\Psi = \psi_a - \psi_0$. This form of the helicity was used with the output of an equilibrium code to produce the values of helicity for three different IREs in discharges 13032 (in Table 6-2), 13462, and 14000.

The results of the analysis are mixed. Shot 13032 gives the smallest change in helicity (-5%), from -3.9×10^{-6} to -4.1×10^{-6} Wb^2. Shot 13462 had the largest change, -28%, from -2.3×10^{-6} to -3.2×10^{-6} Wb^2. Shot 14000 had a positive change of 15%, from -1.7×10^{-6} to -1.4×10^{-6} Wb^2. For the shots analyzed, then, the helicity changed over IREs by values between +15% to -28%. The underlying hypothesis is not well-defined at this point, so it is impossible to declare if these results are sufficient to vindicate or refute helicity conservation over internal reconnection events. These results are also tempered by the fact that the internal magnetic energy dropped by roughly 50% over the IRE in each case analyzed.

6.4 References

1. STIX, T.H., Phys. Rev. Lett. **36** (1976) 521.

2. CALLEN, J.D., "Models of Plasma Confinement and Heating in Tokamaks", U. of Wisconsin Center for Plasma Theory and Computation Report UWPR 89-2, 1989.

3. GRANETZ, R.S., HUTCHINSON, I.H., OVERSKEI, D.O., Nucl. Fusion **19** (1979) 1587.

4. CARRERAS, B., HICKS, H.R., WADDELL, B.V., Nucl. Fusion **22** (1982) 1191.

5. SYKES, A., Seminar at the U. of Wisconsin-Madison, November 18, 1996.

6. SYKES, A., Private Communication.

7. HENDER, T.C., Private Communication.

8. TAYLOR, J.B., Phys. Rev. Lett. **33** (1974) 1139.

9. NELSON, B.A., et al., Bull. Am. Phys. Soc. **41** (1996) 1577.

10. NELSON, B.A., JARBOE, T.R., et al., Phys. Plasmas **2** (1995) 2337.

7. Summary

7.1 Overview

The spherical tokamak (ST) is an evolutionary extension of the tokamak concept. This concept may represent a substantial improvement over the conventional tokamak paradigm. Theoretically the ST should be able to achieve stable values of β that are significantly larger than those currently attainable. The ST appears to be more resilient to disruptions than conventional tokamaks. The small size of the ST would also imply a significantly lower capital cost for a reactor or volumetric neutron source. But spherical tokamaks are only in the early stages of experimental development. Significant amounts of research will be required to determine if they will live up to their initial promise.

The Madison EDUcational Small-Aspect-ratio (MEDUSA) tokamak was designed and built to begin answering some of the many questions surrounding STs. As its name implies, MEDUSA is a small spherical tokamak; some of its parameters are R = 9-13 cm, a = 5-9 cm, I_p = 10-40 kA, B_T = 0.2-0.5 T, $A > 1.4$, and $\beta_T < 4\%$. MEDUSA had a threefold mission. The first mission was educational—MEDUSA was designed and built as a student project. The second mission was to serve as a technology and experience test bed for the Pegasus toroidal experiment currently under construction at the University of Wisconsin. The third mission—and the point of this thesis—was to study two aspects of the plasma performance.

The first of these two aspects was the plasma startup. This included a survey of the flux consumption performance of several types of MEDUSA discharges and a study of the mechanisms responsible for current penetration during startup. The second aspect was internal reconnection events (IREs), which are non-terminating disruption-like phenomena

observed in STs. This part of the study involved reconstructing equilibria before and after IREs to determine their effect on the plasma, and a search for any detectable MHD precursor to these events.

7.2 Startup Results

It was found that the Ejima coefficient for the MEDUSA discharges under consideration increased with increasing toroidal field (from 0.2 to 0.375 T) and increasing loop voltage (from 7.8 to 9.4 V). See Table 5-4 and Figure 5-9. The lowest Ejima coefficient found in this study was 0.61, for shot 14068, which was a high-voltage discharge at 0.375 T. Double tearing modes and classical current diffusion were both found to play a significant role in distributing the current density during startup. Double tearing modes were not necessarily detrimental to the startup, as might be expected. This result for C_E can be compared with results from other tokamak experiments. An Ejima coefficient of 0.47 was found in experiments [1] on Doublet III, while results from CDX-U have indicated values of C_E possibly as low as 0.3 [2]. TSC simulations of ITER startup give values of C_E between 0.39 and 0.57 [3].

Generally, the Ejima coefficient is decreased when the inductive plasma flux is increased relative to the total input flux. The internal inductive flux ($\Phi_{int}^{ind} = \ell_i I_p$) may be increased by increasing the plasma current, the internal inductance, or both. The external inductive flux may be increased by increasing the plasma current. Thus improving the flux consumption (reducing C_E) by increasing the inductive fluxes can result in trade-offs between increasing the current and increasing the internal inductance.

In the comparisons between shots of constant toroidal field, it was found that the discharges with larger values of ℓ_i during startup consistently produced smaller values of

C_E. This is clearly illustrated in the comparisons of discharges at equal toroidal fields but with differing loop voltage waveforms. The higher-voltage shots experience noticeably greater double tearing mode activity during the current ramp than do the lower voltage discharges (see Figures 6-7 and 6-8). These DTM events in the higher-voltage shots lead directly to current penetration on a significantly faster time scale than standard magnetic diffusion, while the lower-voltage shots see the current "fill in" on roughly the magnetic diffusion time of 300 μs, as can be seen on Figure 5-10. This faster current peaking in the higher-voltage shots results in higher and more peaked pressure profiles from increased on-axis current and reduced edge heat losses. This behavior can also be observed in the comparison of discharges 14021 and 14060, which had identical control parameters. The higher-performing shot (14021) experienced greater tearing mode activity in the first 100 μs of the discharge, which slowed the current ramp slightly but resulted in an increased ℓ_i during the startup and hence an improved flux consumption.

The interplay between double tearing modes and flux consumption is more subtle in the comparison of discharges at constant loop voltage waveform but variable toroidal field. The onset of double tearing modes occurred later as the toroidal field increased, as can be observed in Figure 6-10. This suppression of DTM activity at higher B_T results in a reduced rate of current penetration relative to the lower-field discharges as shown in Figure 5-10. In this case the lower-ℓ_i (higher-field) discharges achieved lower values of C_E than did the higher-ℓ_i (lower-field) shots. The higher-field discharges achieved larger values of the maximum plasma current than the lower-field shots. This increased current leads to improved flux consumption by dominating the $I_p \ell_i$ term. One must be careful not to draw too many conclusions from the toroidal field scan results. The toroidal field is a significant variable in tokamak operation, and affects these results in many ways besides the

suppression of double tearing modes; plasma initiation and confinement (at least in some models) both improve with toroidal field, and these effects undoubtedly play a role in the improved flux consumption of the higher-field shots.

7.3 IRE Results

Internal reconnection events were found to affect the plasma much like a disruption. Internal magnetic probe data taken for several IREs showed large drops in the plasma major radial field, which became more severe closer to the magnetic axis; reductions in the average field at probe 2 (Z=1.9 cm) often exceeded 50%. Coherent oscillations at around 65-75 kHz were found to emerge consistently on probes 2-5 around 100 μs before the IRE. This precursive behavior has never been detected before in any operating ST. These fluctuations disappear after the IRE. An example of this behavior is given in Figure 6-15. This precursor appears to be associated with a magnetic island or islands, which strengthens the association of IREs with "minor" disruptions. Equilibrium results from three separate IREs confirmed previous observations from START: ℓ_i drops dramatically (50%) as the current profile broadens, β falls drastically (30-80%), the plasma elongates and moves inward, q_0 increases from near 1 to a much greater value (4 - 20), while q_{98} was found to change significantly less, decreasing by about 15%. See Table 6-2 and Figure 6-16 for sample data.

The consistently observed decrease in the edge q does not provide support for the "START picture" of IREs. This hypothesis claims that IREs do not result in disruptions since the edge value of q does not decrease, unlike a disruption-produced reconnection in a conventional tokamak, keeping the plasma edge stable to edge kink modes. Another hypothesis tested by this data claims that the outer edge of the plasma acts as a flux conserver, keeping the magnetic helicity constant in the plasma over an IRE. Explicit

support for this hypothesis was not forthcoming: results for the three shots analyzed gave changes in K between -30% and +15%. However, the hypothesis of helicity conservation over IREs is not well-developed, and these results may in fact be reasonable in a more well-developed version of the hypothesis.

7.4 Conclusions

The objectives of this thesis were satisfied as:

1. The MEDUSA tokamak was designed, built, and operated. It has produced plasmas with significant values of β_N and large current densities. MEDUSA was the first spherical tokamak to reproduce the internal reconnection events first observed on the START experiment, and also the first to make internal current profile measurements. The equilibrium behavior of MEDUSA was modeled with a Grad-Shafranov computer code, and the resultant equilibria provided good fits to the experimental data.

2. The flux consumption was evaluated for different startup scenarios and the effects of some independent parameters were determined. It was found that the Ejima coefficient decreased with increasing loop voltage and toroidal field. Double tearing modes were discovered to be a significant factor governing the startup efficiency. These events were found to be beneficial for flux consumption, since they led to more rapid current penetration and hence a hotter, less resistive core. This effect was not always dominant, though, as illustrated in the toroidal field scan where improved breakdown behavior at higher field led to improved flux consumption.

3. The behavior of internal reconnection events on MEDUSA was characterized. It was found that these events were disruption-like in character, resulting in rapid broadening of the current profile and significant loss of plasma pressure. An internal precursor was found, which appeared to be the result of a magnetic island or islands. This precursor has a frequency around 65-75 kHz and typically appears 80-100 μs before the IRE. The MEDUSA IRE results do not support the START picture of IREs. The magnetic helicity changed by -30% to +15% in the analyzed cases, and the stored magnetic energy fell by roughly 50%, leaving the validity of helicity conservation over IREs as a question for further refinement.

7.5 References

1. EJIMA, S., et al., Nucl. Fusion **22** (1982) 1313.

2. JONES, T.G., Ph.D. Thesis, Princeton University, November 1995.

3. JARDIN, S.C., KESSEL, C.E., POMPHREY, N., Nucl. Fusion **34** (1994) 1145.